Contents

1 Introduction

An introduction to Alternating-current thin-film electroluminescent (ACTFEL) device technology begins with the discovery of the category of materials that luminesce, known as phosphors. Luminescence is a non-thermal conversion of energy from some excitation source into light. The phenomenon of luminescence is observable in many forms, such as bioluminescence, triboluminescence, photoluminescence, cathodo-luminescence and electroluminescence [1].

Electroluminescence (EL) is the conversion of electric energy into light by subjecting a phosphor to an electric field. High-field EL was first discovered by Destriau [2], which observed light emission after applying a high AC voltage to a thin layer of fine Cu doped ZnS powder particles suspended in castor oil. Practical high-field ACFEL devices in the form of powder lamps were later developed by Sylvania after the emergence of the transparent conductor ITO in the early 1950's. The development of powder AC-EL gave way to thin-film EL technology after Vlasenko and Popkov showed brighter luminance from thin-film ZnS doped with Mn. [3] Thin-film electroluminescence suffered stability problems until 1974 when Inoguchi et al.reported a TFEL ZnS:Mn device sandwiched between two insulators which showed high luminance and a long operating life under an applied AC voltage [4]. ACTFEL technology has since matured with the commercialization of monochrome at panel displays in the early 1980's and the development of multi-color displays in the 90's.

The primary application of ACTFEL technology is as a thin display in the flat-panel display (FPD) industry, which is driven by the demand for portable displays [5]. The leading FPD technology is the liquid-crystal display (LCD), found in a number of applications, such as watches, calculators, laptop computer monitors, and hand-held electronic devices. The LCD display is expanding into the desktop monitor market, replacing cathode-ray tube (CRT) technology. Other FPD technologies are the plasma display panel and the field-emission display (FED). The advantages of ACTFEL displays over LCDs are full-viewing angle, performance over a wider temperature range, sufficient ruggedness, and the ability to pattern smaller pixels.

An ACTFEL device has the structure of a metal-insulator-semiconductor-insulator-metal (MISIM) thin-film stack. The standard ACTFEL device structure, shown in Fig.1, employs a transparent substrate, typically glass, coated with a transparent conducting layer, which serves as the bottom electrode. The bottom insulator, phosphor, and top insulator layers reside between the bottom transparent conductor and a top conducting layer, which is opaque. The top conducting layer serves both as an electrical contact and as a reflector to direct light generated in the phosphor layer out through the glass substrate. The standard structure is the most prominently used structure by ACTFEL researchers. It is also used in manufacturing.

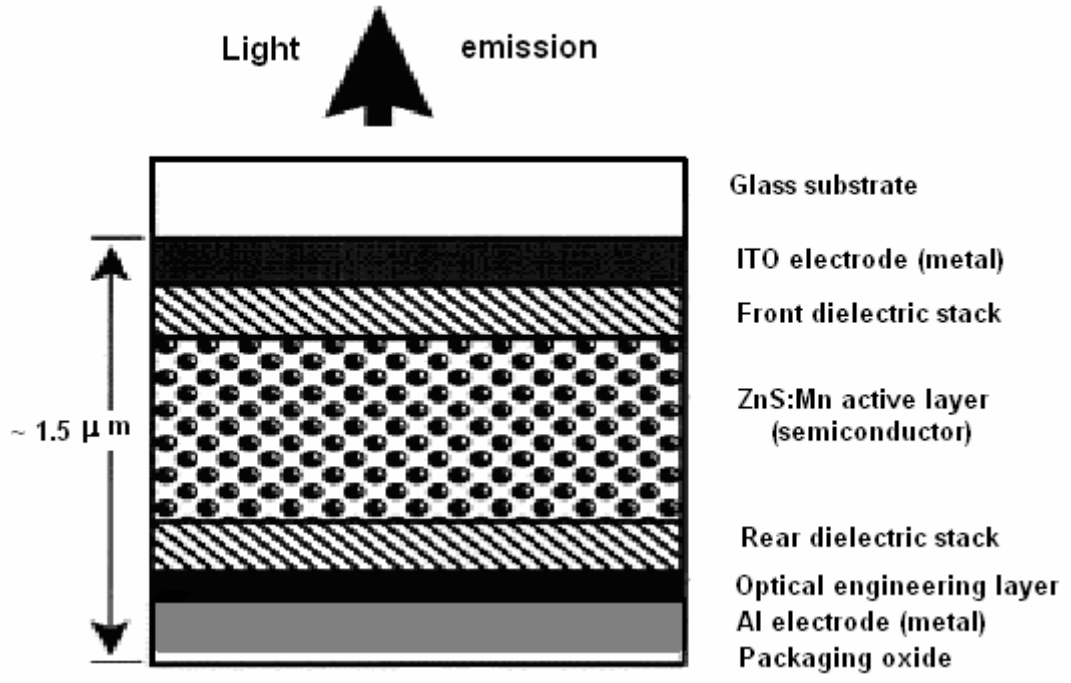

Fig.1.1 ACTFEL thin-film stack

ACTFEL displays are inferior to LCDs in that they suffer greater power consumption, lack adequate chromaticity, and require much larger driving voltages. The strong interaction of "hot" electrons with lattice phonons and crystal imperfections renders high-field EL an inefficient process, making it naturally more difficult to find sufficiently efficient phosphor materials for ACTFEL devices that emit in the primary colors. The best known ACTFEL phosphor to date is the yellow emitting ZnS:Mn, which can be filtered to give bright red and green emission.

1.1. Objective of the thesis

The **objective** of this thesis is to **study the electrical and optical characterization** of ACTFEL display, and specifically the **aging process** of materials that comprise the ACTFEL display in an effort to improve the overall performance of the primary phosphor colors in terms of brightness, efficiency and stability. Since the dominant flat-panel display technology is the LCD, an alternative flat-panel display technology must gauge itself in terms of the LCD. The advantages of ACTFEL displays in comparison with LCDs are the ability to pattern much smaller pixel, performance over a wider temperature range, full-viewing angle, and readability with much greater intensity background light. The disadvantages of ACTFEL displays in comparison with LCDs are larger power consumption, lack of adequate chromaticity of the three primary colors, and much larger driving voltages.

Although the use and importance of green phosphors appeared to be overcome, the target for the near future is the investigation of a green phosphor with enough brightness to maintain the correct ratio of brightness between the red, green and blue phosphors. For this reason, the **development of green ZnS:Mn ACTFEL phosphors**

and **their characterization** is the main emphasis of this thesis although phosphors of other colors have not been entirely ignored.

Because of limited funds for this investigation, which was marginal in the mainstream of the research in the Department of Physics, the realistic goals of the thesis was to provide an improved understanding of luminescent materials, and to exploit their properties to achieve bright, efficient green phosphors for use in full-color at-panel displays. Fortunately, a high-luminance, high-efficiency ACTFEL phosphor system, capable of being processed at temperatures below the glass substrate melting temperature, has been study on the different ACTFEL samples prepared by French colleagues from University of Technology of Troyes. The development of ACTFEL phosphors has also been advanced through the exploration of other phosphor materials, such as Zn_2GeO_4:Mn and ZnS:Mn doped with KCl.

One of the important objectives of this thesis is its pedagogical aspect. Therefore, the presented text can also be considered as a textbook suitable for our students in Libya.

1.2 Organization of the thesis

The structure of this thesis is as follows:

Chapter two presents a review of currently available knowledge pertaining to ACTFEL materials, device, and testing. The chapter begins by examining the structure and operational physics of an ACTFEL device. Then, materials and material issues in ACTFEL fabrication are considered. Finally, characterization and testing of ACTFEL materials and devices is examined.

To understand the result of the current study, the experimental set-ups used in this thesis for optical, electrical and aging characteristics of ACTFEL devices are shortly described in Chapter three. The following chapters deal with these characterization methods more in details.

Chapter four presents the results obtained from different optical and opto-electrical measurements of ACTFEL devices of ZnS:Mn phosphor hosts. Moreover, the effects of KCl co-doping on the microstructure and the EL properties (mainly brightness and luminous efficiency) of ZnS:Mn phosphors have also been investigated.

Chapter five investigates the non-common electrical characterization of ACTFEL devices. We also calculated charged center scattering rates, and simulated the electron transport process in an ACTFEL device.

Chapter six presents the aging study of ACTFEL devices as an important part of their characterization. The practical case of a Zn_2GeO_4:Mn (2% Mn) ACTFEL device operated at 50 Hz was studied and a luminance stability by a measurement of luminance-voltage (L-V) and luminous efficiency-voltage (η-V) characteristics has been evaluated.

Finally, chapter seven brings the overall conclusions of this work and some recommendation for the future tasks in this area.

2 State-of-the-art

This chapter presents a review of currently available literature pertaining to ACTFEL materials, device, and testing. The chapter begins by examining the structure and operational physics of an ACTFEL device. Then, materials and material issues in ACTFEL fabrication are considered. Finally, characterization and testing of ACTFEL materials and devices is examined.

For many years the cathode-ray tube (CRT) has dominated the information display marketplace. The reason for this dominance is that the CRT is a relatively mature technology compared to other display technologies. The advantages that CRT displays offer are excellent chromaticity, contrast and resolution at an affordable price. The main drawbacks of CRT displays are their fragile nature, large size, and high power consumption. These drawbacks have little relevance when a display is intended for use as a home television set or a home computer monitor. However, during the past decades there has been an intense drive towards portability for many display utilizing products, necessitating displays that are physically smaller, more rugged and less power consumption than the CRT.

The drive for portability has fueled a large amount of research into alternative display technologies during the past fifteen to twenty years. Most of the research involving non-CRT display technologies is focused upon developing a thin display, known as a flat-panel display (FPD) that has the quality of a CRT display, but is rugged and much less power hungry than a CRT display of comparable viewing area. The clear front-runner in this effort is the liquid-crystal display (LCD) which is found in virtually every laptop computer manufactured today. Other less well-known display technologies showing promise are the plasma display panel (PDP), the field-emission display (FED), and the thin-film electroluminescent (TFEL) display. All of the flat-panel display technologies require significant amounts of research and development to match the quality and affordability of the CRT, but LCDs are years, if not decades ahead of competing FPD technologies in terms of technological maturity. It is naive to think that the LCD could be rivaled by any other FPD technology in the very near future however, the plasma display, the FED, and the TFEL display are all currently commercially produced and are competitive in certain niche markets. The PDP seems ideally suited for use as a large area display (> 20'' diagonal), a display size far too large to be rivaled by LCDs with the current state of LCD technology. The FED is the least mature of all of the technologies mentioned, but is presently attracting great interest due to the potential for very high brightness FPDs [6]. The TFEL display seems well suited for production of small display (< 4" diagonal) and displays requiring operation in harsh environments. If all of the FPD technologies continue the maturation process, the day may arrive when each display technology owns a portion of the display market in which it excels.

2.1. ACTFEL device structures

An ACTFEL device consists of several constituent thin-film layers that are all important in terms of device operation. All ACTFEL devices consist of a phosphor layer, at least one insulating layer, an opaque conductor, a transparent conductor, and a substrate. However, there are three different general structures comprising the aforementioned layers commonly employed when fabricating ACTFEL devices for testing purposes.

The first structure, the "*standard structure*", consists of a phosphor layer encapsulated by two insulating layers, with contact to the top insulator made by an opaque conductor and to the bottom insulator by a transparent conductor. The standard structure for ACTFEL device fabrication is deposited onto a transparent substrate and light reaches the viewer through the substrates, as shown in Fig.2.1a.

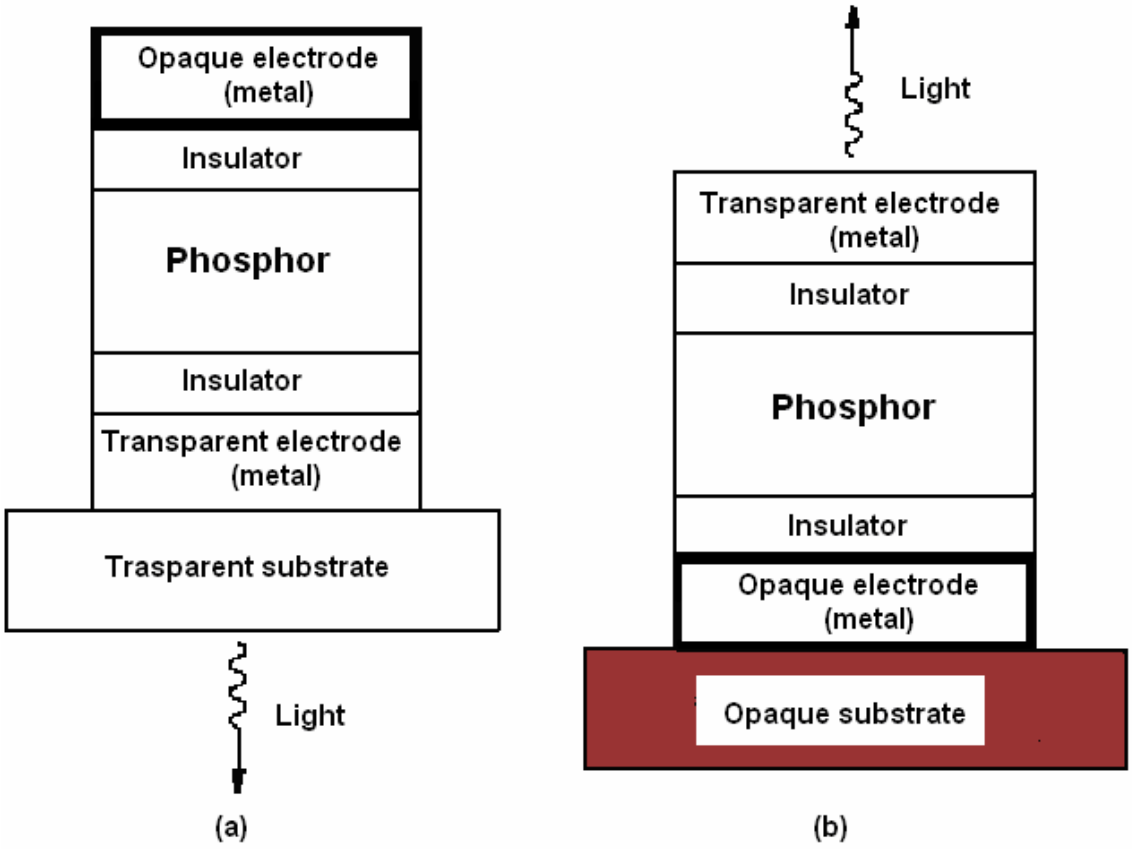

Fig.2.1: (a) The standard ACTFEL device structure. (b) The inverted ACTFEL device structure.

The second structure, the "*inverted structure*" also consists of a phosphor layer encapsulated by two insulating layers, but contact is made to the top insulator by a transparent electrode and to the bottom insulator by an opaque electrode. The inverted structure for ACTFEL device fabrication can be deposited onto either a transparent substrate or an opaque substrate, because the light reaches the viewer through the transparent top electrode, as shown in Fig.2.1b.

The standard and inverted ACTFEL device structures are both used in commercial processes, and the choice of which structure to use is often dictated by process requirements, process limitations or intended device applications.

The standard structure is the preferred structure for test devices and monochrome passive-matrix displays because it requires a less complex process than the inverted structure. The most important advantage of the standard structure is that it exhibits so-called self-healing breakdown when a suitable top electrode is deposited [6].

The self-healing breakdown property prevents small pinholes and defects from causing catastrophic device failure by effectively open-circuiting microscopic defective areas of the ACTFEL device. Another advantage of the standard structure is inherent durability because the active device layers are shielded from the viewer by the glass substrate. However, the inverted structure possesses several distinct advantages over the standard structure, and is therefore preferred for certain applications. When high temperature process steps are necessary, the standard structure is unusable because the glass substrates necessary for this structure begin melting around 600 °C.

Unlike the standard structure, there is the option of depositing on opaque substrates when the inverted structure is employed, allowing the use of high-temperature tolerant ceramic or silicon substrates. Another case where the inverted structure is preferred over the standard structure is when color filtering is required. When adding filter layers to a device, it is advantageous to deposit these layers on top of a finished device because simple organic color filters that are sensitive to further process steps can be used [7]. However, when the standard structure is employed, it is necessary to deposit the color filter layers first because light is viewed through the substrate. The main disadvantage of the inverted structure is that self-healing breakdown characteristics are not achievable with transparent top-electrodes. This necessitates extremely low defect density ACTFEL devices for stable and reliable inverted structure ACTFEL device operation. This requirement greatly increases the processing complexity, and hence cost, because special processing techniques are required.

The third ACTFEL device structure that is sometimes used for testing purposes is the "*one-insulator*" structure. The one-insulator structure is essentially either the standard structure or the inverted structure minus either of the insulator layers. The phosphor layer ($BaTiO_3$) encapsulated by two insulating layers, with contact to the top insulator made by an opaque conductor (ZnO:Al) and to the bottom insulator by a transparent conductor (Al).This structure is used in ACTFEL testing because the elimination of an insulator deposition process step allows devices to reach the testing phase more rapidly. For certain applications, a one-insulator structure is used with the phosphor layer deposited directly on a thick insulating ceramic sheet that serves the dual purpose of the substrate and an insulator layer. A cross-section of a device of this type is shown in Fig.2.2 [8]. Although the one-insulator structure has advantages in terms of ease of device fabrication, it is not used in commercial products because it exhibits lower luminance, affords less protection for the phosphor layer, and is not compatible with long-term device reliability.

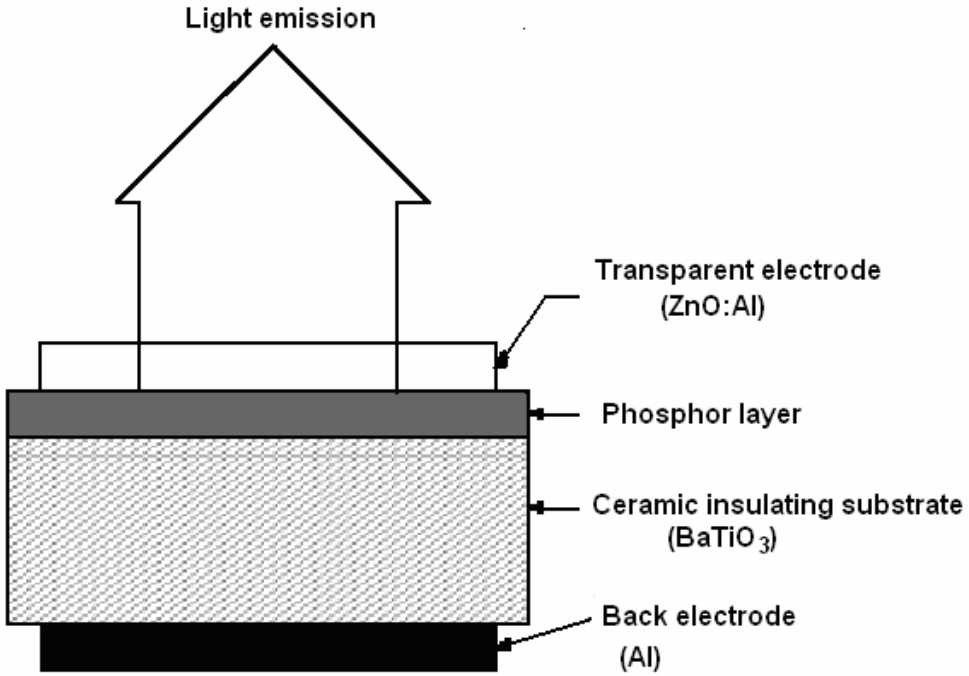

Fig.2.2: Cross-section structure of an ACTFEL device deposited on an insulating $BaTiO_3$ sheet [8].

2.2 ACTFEL device physics

In this section we are mainly concerned with the basic physical processes and their interrelations which lead to high-field electroluminescence in zinc sulfide devices. A basic requirement for electroluminescence to occur is that an electric field be applied to a luminescent material with sufficient strength to generate charge carriers which can impact-excite or impact-ionize a luminescent center. Impact excitation and impact ionization are differentiated by the valence state of the impurity after impact [9]. Impact excitation does not change the valence of the impurity but rather rearranges the electrons to a higher energy configuration. Impact ionization of defects results from delocalization of a valence electron into a continuum state, such as the conduction band, and leaves an ionized center. This center is then free to recombine with a free electron. For example, in ZnS a Mn^{2+} ion is typically excited by direct impact, while in CaS a Eu^{2+} ion is thought to be ionized and then later brought back to its ground state after a radiative recombination with a free electron [9]. Impact ionization of the lattice can also occur resulting in the generation of an electron-hole pair. Figure 2.3 below shows a simple illustration of the six primary physical processes involved in the operation of an ACTFEL device. To observe electroluminescence:

1) Electrons are injected from interface states by tunneling into the phosphor conduction band.
2) Electrons are accelerated to ballistic energies during high electric field transport across the phosphor; impact scattering can result in electron-hole production and electron multiplication in the host lattice.

3) Luminescent centers are impact excited.
4) Relaxation of electrons.
5) Electrons are trapped at the anode interface, resulting in a counter field that stops current flow
6) Radiative de-excitation of the impact-excited luminescent center results in emission of light. [10]

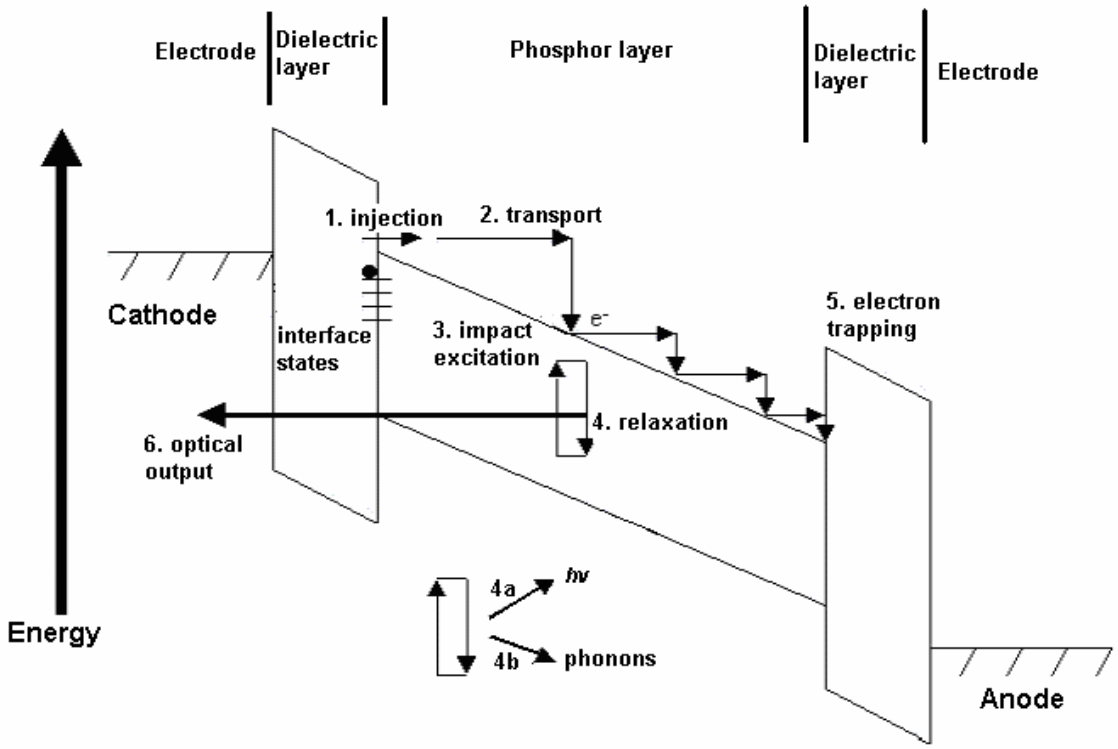

Fig.2.3: Energy band diagram of ACTFEL device and schematic illustrations of the EL emission mechanism [11].

The six steps shown in the Fig.2.3 will now be explained in more detail in subsequent sections.

2.2.1 Tunnel injection

In general there are three mechanisms which are responsible for carrier injection, namely

1) thermionic emission,
2) field emission,
3) tunneling [11].

Several experiments support the fact the electrons trapped at the phosphor-insulator interface are the carrier source and that thermally assisted electron tunneling is the main mechanism. Typically, commercial ACTFEL displays are driven at 50 Hz with 30 ms pulses and an 8 ms rise and fall time. When the voltage applied to the device reaches a critical value (called the threshold voltage), the electric field at the phosphor

becomes sufficiently large (~1-2 MVcm^{-1}) and the energy bands are bent enough so that electrons trapped at interface states (or deep states distributed throughout the thin film) may tunnel into the phosphor conduction band. The tunneling emission current J for Schottky barriers is given by [12]

$$J \approx E^2 \exp\left[\frac{-8\pi\sqrt{2m^*}(q\Phi B)^{3/2}}{3qhE}\right], \tag{2.1}$$

where E is the electric field, m^* is the effective electron mass, q is the charge of an electron, Φ_B is the barrier height, and h is Planck's constant. For this equation to apply to electron trap state emission, the barrier height term is replaced by a term that represents the interface trap depth. The ideal electron trap is shallow enough to avoid excessively high fields for electron injection, but sufficiently deep so that injection fields will result in acceptable acceleration of the electrons. From this description it becomes apparent that, unlike in other semiconductor devices, a high density of interface states and deep bulk states is desirable in order to inject enough current to excite EL emission.

Several groups have attempted to increase the density of occupied states through modification of the phosphor/insulator interface. Kobayashi *et al*. [13], Ohwaki *et al*. [14], and Rack *et al*. [15] have added thin interfacial layers (SiO_2, Ge, In) between the phosphor and insulator. In all cases, the interfacial layers were found to enhance the electron injection current, presumably through an increased density of trapped electrons. The other additional mechanism suggested for charge injection is thermionic emission. The expression relating the thermionic current, J_e, to temperature is the Richardson-Dushman equation [16]:

$$J_e = \left(\frac{(kT)^2 mq}{2\pi^2\hbar^3}\right)\exp(-\frac{\Phi}{kT}), \tag{2.2}$$

where, J_e is the electronic charge flux, m is mass of electron, k is Boltzmann's constant, $\hbar$ is Planck's constant h divided by 2π, Φ is the work function, and T is temperature. This equation must be modified to take into account the phosphor's electron affinity, as it is valid for the metal-vacuum interface.

2.2.2 High field charge transport

The mechanism of high field electron transport in ACTFEL devices has always been a matter of intense debate. Simulations of high-field electron transport in ACTFEL devices have been investigated by several groups using Monte Carlo techniques. Initially, Brennan [17] used a full-band ZnS structure to calculate the electron energy distribution for electric fields up to 1 MV/cm. For this electric field region, he concluded that very few electrons obtained sufficient energy to excite Mn luminescent centers. Later, a simple parabolic-band model [18] was used to simulate the high field transport properties in ZnS in which the conduction band was described by a single parabolic band. In addition, this parabolic band model assumed that the electron scattering was dominated by polar optical phonon scattering. These calculations suggested that the electrons in ZnS experience nearly loss free transport, which is referred to as electron runaway, and resulted in a very energetic electron energy

distribution. Later, a nonparabolic conduction band was implemented by Bhattacharyya *et al*. [19], where they included scattering due to polar optical phonons, acoustic phonons, intervalley scattering, and ionized and neutral impurities. In this case, electron runaway was no longer observed and the electron energy distribution became stable. It was determined that nonpolar interactions and conduction-band nonparabolicity stabilized the electron distribution by increasing the electron-phonon scattering rates.

Figure 2.4 shows the electron energy distribution $n(E)$ as a function of electron energy for different phosphor fields, and the impact excitation rate for Mn^{2+} as a function of energy obtained from the nonparabolic band model [19].

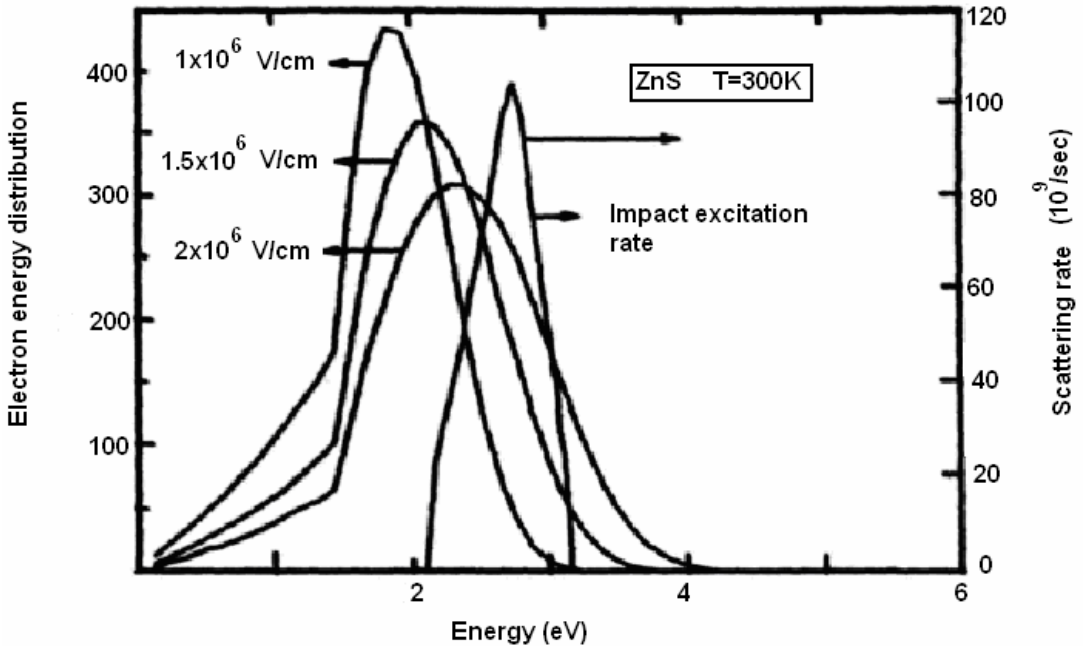

Fig.2.4: Electron energy distribution as a function of energy for different phosphor fields using the nonparabolic band structure model [19]. The impact excitation rate as a function of energy is also included.

This electron energy distribution n(E) as a function of electron energy using the full-band model is shown in Fig.2.5. The Mn^{2+} impact excitation cross-section as a function of electron energy is also shown here. The data indicate that a majority of electrons are able to attain energies of around 2.12 eV, the minimum energy required to excite Mn^{2+}.

A simpler approach was taken by Bringuier [20], who employed a so-called "lucky-drift" approach. He made the argument that the full-band Monte Carlo approach may be more accurate, but given the lack of certainty in some physical parameters of II-VI compounds and the poor crystallinity in ACTFEL devices, the lucky-drift approach should be adequate to highlight the important factors in device operation. The lucky-drift approach is an extension of the original theory given by Baraff [21]. In this theory two transport modes are considered. One is ballistic transport, which is collision-free. The other is the drift mode, which occurs after the electron has had one collision, which increases the probability of subsequent collisions.

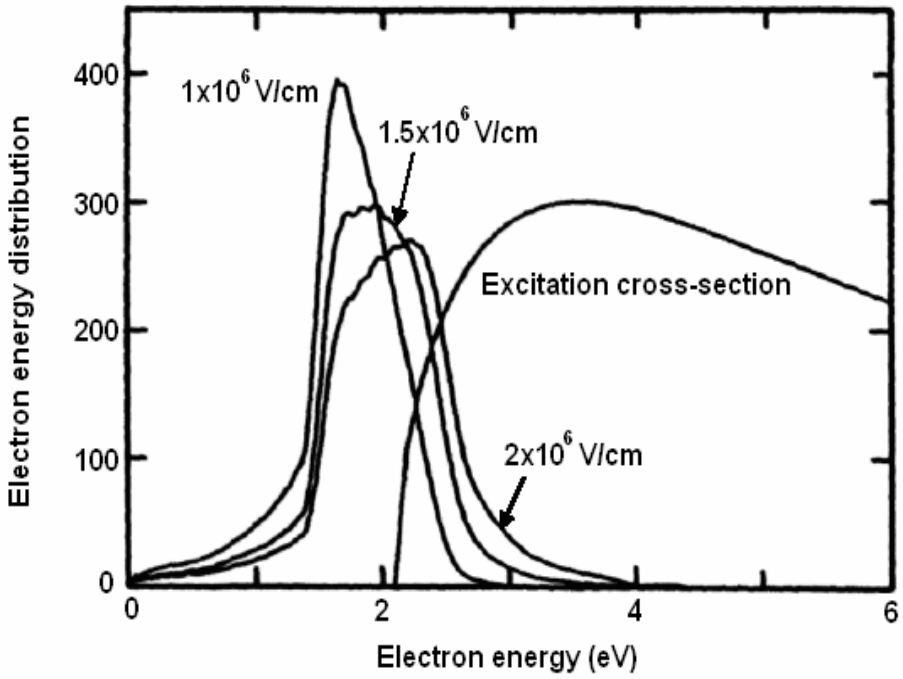

Fig.2.5: Electron energy distribution as a function of energy for different phosphor fields using the full-band structure model [19]. The impact excitation cross-section as a function of energy is also included.

2.2.3 Impact excitation/ionization

As the hot electrons (e.g. the electrons that are in excess of the thermal equilibrium number and, for metals, have an energy greater than the Fermi level; for semiconductors, the energy must be a definite amount above that of the edge of the conduction band) travel through the phosphor matrix, a fraction may interact with the luminescent centers (activators), resulting in either impact excitation or impact ionization. The electron-luminescent interaction probability is related to the luminescent center radiative cross-section. Impact excitation is the case when an electron in the ground state of the luminescent center is excited to a higher electronic state localized on the activator ion core. De-excitation from the excited state may occur either radiatively or non-radiatively. Radiative relaxation paths result in the emission of a photon whose wavelength corresponds to the difference in energy between the excited and lower energy states. Non-radiative relaxation results in phonon emission, which will dissipate the potential energy of the excited luminescent center in the form of heat without resulting in luminescence. The delay time between excitation and relaxation can be long (ms) or short (a fraction of a μs), depending on the spin and parity selection rules applied to the excited and ground states [10]. If the ballistic electron (e.g. an electron passing through a semiconductor whose length is less than the mean free path of electron in the semiconductor, so that most of the electrons pass through the semiconductor without scattering) ionizes the ground state electron of the luminescent center by impact scattering an electron into the phosphor conduction band, this process is called impact ionization. Once ionized, the activator ion core may trap either an electron or a hole and subsequently capture a carrier of the opposite charge to result in electron-hole recombination, with subsequent light emission. In high fields, the

electrons are accelerated to such high energies that the cross section of capture and radiative relaxation is significantly reduced. In addition, at high fields the residence time of a trapped carrier may be so short that recombination is unlikely (i.e. the carrier may be field stripped from the center) [22]. At high fields, electron multiplication also occurs where one electron elastically scatters off of valence electrons creating two electrons and another hole. These two electrons may accelerate and scatter creating more electrons and holes, with the result known as avalanche breakdown. Because of these complications upon ionization, impact excitation is typically considered to be the dominant mechanism for generating light in ACTFELs [23]. Eventually, the ballistic electrons on reaching the anodic phosphor/insulator interface become trapped in interface states, causing a field of opposite polarity that influences current injection and transport during a large part of the voltage pulse in ACTFELs.

2.2.4 Radiative decay

When an impurity center is in an excited state, that energy will eventually have to be dissipated. The relaxation process can occur by either a) emission of a photon, b) non-radiative decay (relaxation) or c) transfer of energy from one ion to another. For display applications, it is desirable to maximize the first process and to minimize the others.

For a two-level system, the rate of population state decrease to the ground state is given by

$$\frac{dN_e}{dt} = -N_e P_{eg}, \tag{2.3}$$

where N_e is the number of luminescent ions in the excited state, t is the time, and P_{eg} is the probability for spontaneous emission from the excited to the ground state. Upon integration

$$N_e(t) = N_e(0)\exp\left(\frac{-t}{\tau_R}\right), \tag{2.4}$$

where τ_R ($= P_{eg}^{-1}$) is the radiative decay time [22].

The lifetime of the excited state depends on whether the emission is allowed or forbidden. For strongly forbidden emissions the lifetime can be in the range of microseconds to milliseconds, whereas for allowed transitions it may be microseconds or less [22].

2.2.5 Optical outcoupling

An important parameter to be considered is the direction in which the light must escape through the device; hence internal reflection becomes an important issue. In conventional EL devices light generated within the phosphor layer sees several interfaces as shown in Fig.2.6. The phosphor layer typically has the highest index of refraction in the stack, and all layers have a higher index of refraction than air. Hence

when light travels from the phosphor layer through the insulators, we define critical angle for internal reflection θ_c as

$$\theta_c = \sin^{-1}(\frac{n_2}{n_1}), \tag{2.5}$$

where n_1 and n_2 are refractive indices for each media. The extent of internal reflection can be estimated [6, 24] by assuming just the phosphor layer (for ZnS n = 2.3), and that light is reflected from the metal electrode with optical efficiency η_{opt}

$$\eta_{opt} = \int_0^{\arcsin\left(\frac{1}{2.4}\right)} \sin\theta \mathrm{d}\theta = 1 - \left[1 - \left(\frac{1}{2.4}\right)^2\right]^{0.5} \approx 0.1\,. \tag{2.6}$$

The optical outcoupling efficiency can be improved by more than an order of magnitude by increasing the surface roughness and thereby reducing internal reflection [15]. However, too rough a surface can reduce contrast because of increased diffuse scattering [6].

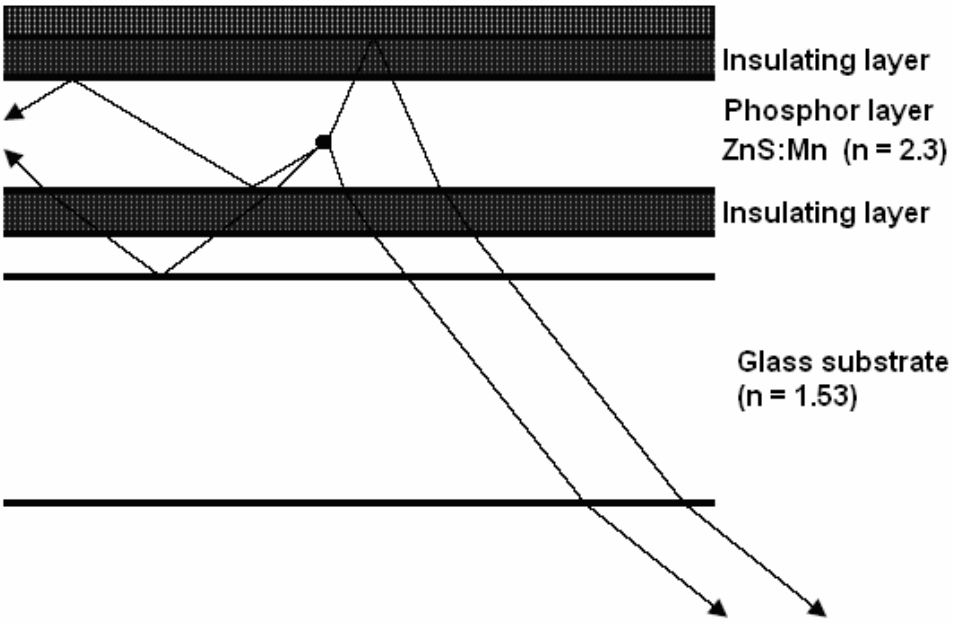

Fig.2.6: Schematic representation of internal reflection in a ZnS:Mn ACTFEL device [6].

2.3 ACTFEL materials

The requirements and critical characteristics for the materials used in ACTFEL devices are discussed below.

2.3.1 Substrate materials

The primary requirements for the substrates for the standard device structure are low cost and easy availability, high transmission coefficient, a thermal coefficient of expansion that is close to that of the deposited films and low alkali metal content (diffusion of metal ions from the glass into the phosphor layer results in deteriorated performance). The most common substrate material is Corning 7059 soda-lime-silicate glass. This is an alkali-free, barium borosilicate glass often used for LCD substrates [25]. It has a softening temperature of ~598°C and large panels can undergo rapid thermal anneals (RTA's) of up to 650 °C without significant damage or warping [26]. Soda lime glass has been used which poses a diffusion barrier to alkali metals [6]. Fig 2.7 is the transmission spectrum of this glass.

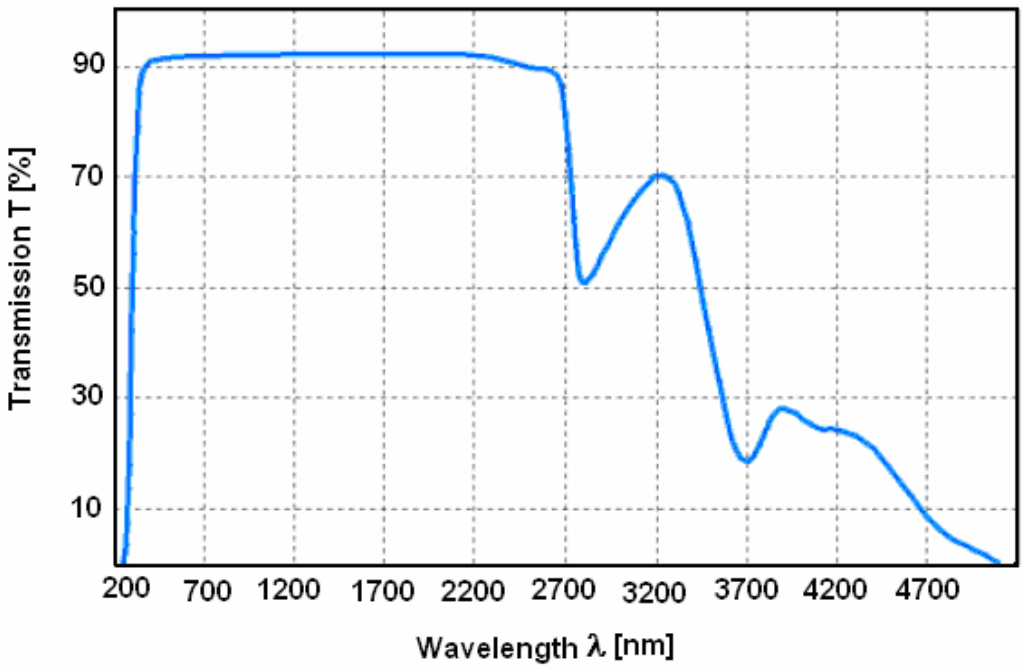

Fig.2.7: Transmission spectrum of Corning 7059 glass [27].

For higher temperatures, glass-ceramics substrates may be used which meet the substrate requirements, but these materials are expensive and not economically viable substrate materials for commercial applications. A cheaper alternative to these expensive substrates is silicon, which is readily available and can be used extensively for visible ACTEFEL devices in the inverted structure format or infrared light emitting ACTFEL devices in the standard structure format. These substrates can withstand high temperature heat treatments of post-deposition annealing.

For the inverted structure devices, the requirements are a smooth surface and the ability to meet the thermal considerations for processing of subsequent layers. For the inverted structure in Fig.2.1b, the substrate acts as part of the device, comprising the bottom insulator, and electrical properties must be considered. These are discussed in the following section.

2.3.2 Transparent electrodes

For the standard device structure the first layer deposited onto the glass substrate is the transparent conductor. The critical materials requirements of this layer are: it must be sufficiently conductive to not affect the RC time constant of the device, it must be as transparent as possible in the topical spectral emission region to minimize absorption and/or color perturbation and finally it must withstand the thermal processing of subsequent layers. The material predominantly used is indium-tin-oxide (ITO) [6]. This is normally an alloy of 90 weight % In_2O_3 and 5-10 weight % SnO_2. ITO can be deposited by a number of deposition techniques, namely pulsed-laser deposition, e-beam evaporation, DC magnetron sputtering, RF magnetron sputtering, plasma ion-assisted deposition, chemical vapor deposition and atomic layer deposition [6, 28, 29]. ITO thicknesses of 200 nm are typical, and good transparency (> 90 %) can be obtained in the visible region of the spectrum with a resistivity of ~1 x 10^{-7} Ω.m, providing a sheet resistance of ~ 50 kΩ/m^2. In addition, ITO is easily patterned with standard photolithography and wet or dry etching.

Though optically transparent, ITO is a degenerately doped n-type semiconductor. The n-type conductivity of ITO is due to the thermal ionization of shallow donors which arise from the substitution of Sn^{+4} onto In^{+3} lattice sites, and oxygen vacancies [30]. Zinc-oxide (ZnO) and zinc-oxide doped Al, In or Ga thin films are also used as transparent conducting electrodes. In the undoped material, n-type conductivity is due to shallow donor levels due to oxygen vacancies while in the doped system, the +3 valence state of Al, In or Ga substituting on Zn^{+2} lattice sites creates shallow donor levels [30]. It is also of importance to choose neighboring layers (substrate and bottom insulator) that do not interact significantly with the ITO layer during subsequent thermal processing. One thing to keep in mind is that, since ITO lacks transparency for wavelengths larger than plasma wavelength (1.6-2 μm), it is only useful for the near infrared light emitting devices. But for mid IR and far IR, ITO would be ineffective and in those circumstances it is wise to choose the inverted configuration ACTFEL device and use Si as a substrate.

2.3.3 Opaque electrodes

For the standard structure, the requirements for the opaque electrode are not stringent because it is the last layer deposited. The top metal electrode is typically 100-300 nm thick and is the last layer to be deposited during device fabrication. It must have a low resistivity, be resistant to electromigration (metal-ion migration) at high fields, have good adhesiveness to the insulating layers and must possess some ability to prevent breakdown propagation (spread) when dielectric breakdown of the insulator (full stack structure) or phosphor (half-stack) layers occurs. Aluminum is the best metal that satisfies these requirements. Aluminum also exhibits desirable wetting characteristics to many common insulator materials, and this provides the possibility for self-healing breakdown by fusing of the metal surrounding a short. The main drawback of Al is its high reflectivity, which leads to higher brightness but lower contrast. Mirror-type reflections occur when external light penetrates the devices and this negatively affects the display contrast. Filters are often used to suppress this back reflection so that only light generated by the device is observed by the viewer. The problem has also been

effectively dealt with by adding either a dark layer above the phosphor or by adding a circular polarizer, which eliminates specular reflection [6].

For inverted structures, in which the electrode is deposited on the bottom of the substrate, aluminum is again commonly used since conductivity, cost, and ease of processing are the major concerns. However for the other type of inverted structure in which the opaque electrode is deposited below the rest of the EL device, the additional requirement for thermal stability is added. The gold (Au), molybdenum (Mo), tantalum (Ta) and wolfram (W) are candidates for this type of structure.

2.3.4 Insulator materials

In the full stack structure, the dc path is blocked. The insulator thickness is usually in the 250 nm range, which is too thick for electrons to tunnel through from the metal under cathodic bias. The device is therefore only capacitively coupled to the externally applied field. The main function of the insulator layers is to protect the ZnS phosphor from electrical breakdown (runaway avalanche breakdown eventually leading to destructive breakdown) at high fields (greater than 200 MV/m). The properties of the insulator layers are therefore critical to device performance. The most important requirements [6, 31, 32] of these layers are:

1) High dielectric constant.
2) High dielectric breakdown electric field strength.
3) Must provide interface states at the insulator-phosphor interface, from which electrons can tunnel into the phosphor conduction-band under the influence of an applied field above a certain threshold value.
4) A small number of pinholes and defects. Pinholes and defects offer sites for local field enhancement and consequent premature dielectric breakdown.
5) Good mechanical adhesion and stress accommodation over process temperatures which range up to 600°C (the coefficients of thermal expansion varies widely for the (different layers).
6) Must act as a barrier to metal-ion diffusion into the phosphor layer.

As we will discuss in detail shortly, above a certain applied threshold voltage carrier injection into the phosphor layer conduction-band occurs due to field emission from interface states. Below the threshold field, the double insulator device structure is a perfect capacitor. Maxwell's equations then apply, and impose the following boundary conditions at the insulator-phosphor interfaces:

$$\varepsilon_{\mathrm{i}}^{\mathrm{t,b}} E_{\mathrm{i}}^{\mathrm{t,b}} = \varepsilon_{\mathrm{P}} E_{\mathrm{P}}\,, \tag{2.7}$$

where ε is the dielectric constant at the frequency of operation, E is the electric field, the subscripts i and p refer to the insulator and phosphor respectively, and the superscripts t and b refer to the top and bottom insulator. The total applied voltage is divided between each layer according to the following:

$$V_{\mathrm{aPP}}^{\mathrm{tot}} = E_{\mathrm{i}}^{\mathrm{t,b}} d_{\mathrm{i}}^{\mathrm{t,b}} + E_{\mathrm{P}} d_{\mathrm{P}}\,, \tag{2.8}$$

where d_i and d_p are the thicknesses of the insulator and phosphor layers respectively. From Eqs.2.7 and 2.8, the fraction of the total applied voltage that appears across the phosphor layer can be calculated as [6]

$$V_P = E_P d_P = \frac{\varepsilon_i d_P}{\varepsilon_i d_P + \varepsilon_p d_i} \times V_{app}^{tot} . \tag{2.9}$$

As (2.9) shows, the dielectric constant of the insulating layer ε_i must be as large as possible and its thickness d_i as small as device reliability will permit, in order to maximize the voltage drop across the EL phosphor layer. Another advantage of insulators with a high dielectric constant is better device reliability due to lower operating voltages, because a proportionally smaller voltage will appear across the insulator layers.

The threshold field for tunnel emission from interface traps in ZnS is ~1.8×10^8 V/m [6]. According to (2.9), the minimum field that the insulator layer must sustain without breakdown in order to perform its function properly is

$$E_i^{t,b} = \frac{\varepsilon_P E_P}{\varepsilon_i^{t,b}} = \frac{8.3\times1.5\times1.6^8\,\mathrm{V/m}}{\varepsilon_i^{t,b}}, \tag{2.10}$$

where ε_p (ZnS) is taken as $\varepsilon_p = 8.3$. This equation shows that high breakdown field and high dielectric constant are inversely proportional, and this has been verified experimentally for several insulators.

Tab.2.1: Typical insulator materials with relative dielectric constant, dielectric breakdown field, figure of merit (maximum trapped charge density at insulator- phosphor interface), breakdown mode and deposition technique.

Material	**Dielectric Constant (ε_i)**	**Breakdown Field E_{DB} (MV/cm)**	**Figure of merit $\varepsilon_i * E_{DB}$ ($\mu C/cm^2$)**	**Breakdown mode**	**Deposition method**
SiO_2	4	6	2	SHB	Sputtering
SiON	6	7	4	SHB	Sputtering/PECVD
Al_2O_3	8	5	3.5	SHB	Sputtering
Al_2O_3	8	8	6	SHB	ALE
Si_3N_4	8	6-8	4-6	SHB	Sputtering
Y_2O_3	12	3-5	3-5	SHB	Sputtering/EBE
Ta_2O_5	23-25	1.5-3	3-7	SHB	Sputtering
$BaTiO_3$	14	3.3	4	SHB	Sputtering
$BaTa_2O_6$	22	3.5	7	SHB	Sputtering
$PbTiO_3$	150	0.5	7	PB	Sputtering
TiO_2	60	0.2	1	PB	ALE
$SrTiO_3$	140	1.5-2	19-25	PB	Sputtering
$Sr(Zr,Ti)O_3$	100	3	26	PB	Sputtering

SHB - self healing breakdown; PB - propagating breakdown; PECVD - plasma enhanced chemical vapor deposition; ALE - atomic layer epitaxy; EBE - electron beam evaporation [6].

As high dielectric constant and high breakdown field are difficult to be satisfy simultaneously, a figure of merit introduced by Howard [33] is used to rate insulators for ACTFEL devices. It is simply the product of the dielectric constant and the electrical breakdown field (E_{DB}), and is a measure of the maximum trapped charge ($\mu C/cm^2$) density at the insulator-phosphor interface. Table 2.1 presents a comparison of the important properties of several insulators. Unfortunately, the insulators with the highest figures of merit exhibit propagating breakdown, which when initiated, spreads catastrophically and eventually destroys the device.

2.3.5 Phosphor layer

The phosphor layer materials consists of a host material and a luminescent center, each discussed below.

2.3.5.1 Host material (matrix)

All phosphors consist of a host material, and a luminescent center or light-emitting dopant. Before proceeding with a detailed look at the ZnS host system, it is worth reviewing the properties that are desirable of all high-field electroluminescence hosts. Namely:

1) The band-gap must be sufficiently large, so that light emitted from the luminescent center not be absorbed (the host should be transparent in the range of the electromagnetic spectrum that is of interest). Complete visible transmission requires a band-gap of at least ~3.1 eV (400 nm). The equation for converting between energy E, wavelength λ, and wavenumber $\acute{\omega}$ is

$$\lambda=1240/E,\ \lambda=1/\acute{\omega} \text{ where } \lambda=[\text{nm}],\ E=[\text{eV}]. \qquad (2.11)$$

2) The host must be non-conducting below the EL threshold. This is required for a voltage drop and subsequent high electrical field across the phosphor, and leads to a capacitive sub-threshold behavior
3) The host must have high breakdown strength to allow for efficient acceleration of electrons. The breakdown field of the host must be at least 1MV/cm
4) The host must have excellent crystallinity and a low phonon-coupling constant in order to minimize electron scattering. To maintain good crystallinity at the dopant levels (~1 atomic %) typically used in EL phosphors, it is desirable to match the geometric size as well as the valence of the host cation with that of the luminescent center [34]
5) The host must provide a substitutional lattice site of appropriate symmetry for the luminescent center.

These requirements have historically been met best by sulfur-based compounds, [1, 5, 15] and thiogallates. Examples of the former group are ZnS, CaS, and SrS, while examples of the latter group are $CaGa_2S_4$, $SrGa_2S_4$ and $BaGa_2S_4$. Table 2.2 summarizes the important physical properties of the sulfide based II-VI semiconductor hosts.

Tab.2.2: Properties of some common ACTFEL host compounds [6].

Property	**IIb-VIb compound**	**IIa-VIb compound**	
Compound	ZnS	CaS	SrS
Melting point (°C)	180-1900	2400	> 2000
Band gap (eV)	3.6	4.4	4.3
Transition type	Direct	Indirect	Indirect
Crystal structure*	ZB, W,O	Rock salt	Rock salt
Lattice constant (Å)	5.409	5.697	6.019
Dielectric constant ε	8.3	9.3	9.4
Ionicity	0.623	> 0.785	> 0.785

*ZB = zinc blende; W = wurtzite; O = orthorhombic.

2.3.5.2 Luminescent centers

The activator impurity (dopant) in the phosphor influences the spectral properties, and to a large extent the temporal properties of optical emission. In many lamp and CRT phosphors, luminescence results from recombination of electrons and holes trapped in deep donor and deep acceptor levels, respectively. The most common examples of this type of phosphor are based on a ZnS host, with some combination of Ag, Cu, Au, Al, and Cl added as the acceptor and donor impurities to tailor the spectral properties and efficiency. This class of luminescent center is not used in ACTFEL devices because the electron-hole pairs are unstable under high fields and the luminescence is effectively quenched [6, 35].

The second type of center is a localized transition between electronic states of an isolated dopant ion. This dopant ion is typically either a transition metal such as Mn^{2+}, Cr^{2+}, Ti^{4+}, Cu^{+}, Ag^{+}, a rare earth ion such as Eu^{3+}, Er^{3+}, Nd^{3+}, Eu^{2+}, Ce^{3+}, Tb^{3+}, or Tm^{3+}, or an s^2 configuration ion such as Pb^{2+}, or Bi^{3+} [6, 22].

Without going into a detailed discussion of the underlying physics, the general emission characteristics of these ions can be separated into several categories based on the electronic configuration of the ground and excited states. One characteristic of importance in terms of both understanding the luminescent process and for application to displays is the radiative decay time. The decay time is determined primarily by two selection rules related to the electronic configuration of the ground and excited states, as well as the surroundings of the ion. The first selection rule is referred to as the parity selection rule, which forbids transitions between levels of the same parity, i.e. transitions within the *d*-shell, within the *f*-shell, or between the *d*-shell and *s*-shell are forbidden. The other selection rule is the spin selection rule, which forbids transitions between configurations with different spin states. Forbidden transitions are not completely forbidden, but they have longer decay times [22].

The transition metal ions mentioned above all have a d^n valence configuration, and emission spectra are all characteristic of intra-shell *d-d* transitions. They are therefore all forbidden by the parity selection rule [22], and their emission is usually broad band (although Cr^{3+} can exhibit line emission in some instances). Therefore decay times for the transition metals can be in the range of 100 μs to several ms, depending on

the spin selection rule and symmetry. Another general characteristic of the transition metal activators is that because the transitions originate in the valence d-shell, they are strongly influenced by the crystal field and ligand fields of the host.

Rare-earth (RE) or lanthanide ions are the second type of luminescent centers that are employed in zinc sulfide phosphors. These are typically used as RE^{3+} ions, which in general, except for Ce^{3+}, exhibit parity forbidden, long-lived 4f-4f transitions. Rare-earth ions have an electron configuration of $1s^2 2s^2 2p^6 3s^3 3p^6 4s^2 3d^{10} 4p^6 5s^2 4d^{10} 5p^6 6s^2 4f^X$, and the energy levels of the atomic orbitals fill up in order of increasing energy as is shown in Fig.2.8 [36]. Thus, the 5s, 5p and 6s orbitals fill up before the 4f orbital, even though the radial probability distribution of the 4f orbital has its maxima closer to the nucleus. As a result, the emission spectra of transitions which arise from the $40f^n$ configuration appear as narrow lines because the 4f electrons are well shielded from their environment by the 5s and 5p electrons. Fig.2.9 is a schematic representation of this shielding effect in RE^{3+} ions.

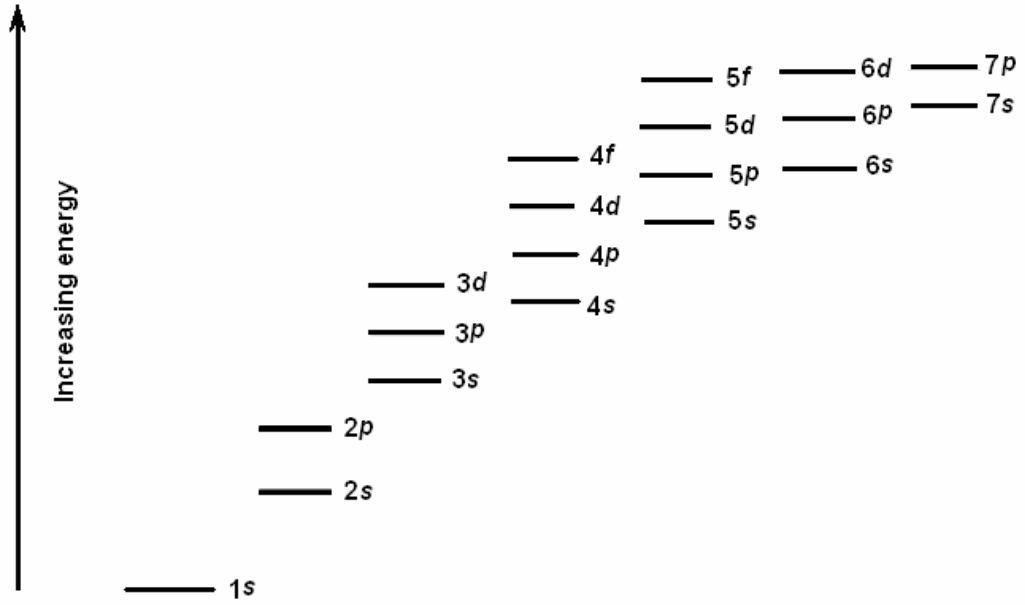

Fig.2.8: The relative energy levels of the atomic orbitals in multi-electron atoms [36]. Orbitals fill up in order of increasing energy as shown above.

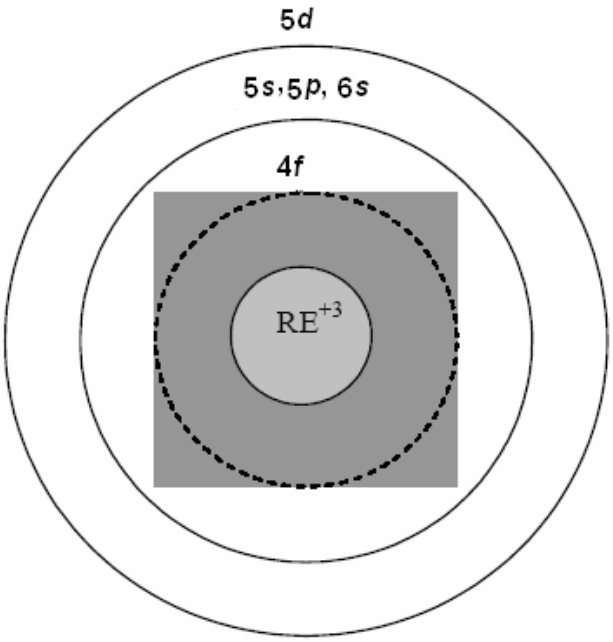

Fig.2.9: Schematic diagram of a RE^{3+} ion showing the radial position of the outer orbitals. Note that 4*f* electrons are shielded, but 5*d* electrons are exposed to the environment.

In cases where emission is a result of 5*d*-4*f* transitions (e.g. Ce^{3+}, Eu^{2+} and Nd^{3+}) the emission spectra are broader because the 5*d* electrons are unshielded and are therefore influenced by their surroundings i.e. the excited state is influenced by the crystal field, the nephelauxetic effect and other luminescent center-host lattice interactions. Since 5*d*-4*f* transitions are parity allowed, they are faster than the parity forbidden 4*f*-4*f* transitions. The book by Blasse and Grabmaier [22] provides excellent details of these effects on luminescent ions. Figure 2.10 shows the partial energy level diagram for several rare-earth ions. Among these are blue emitting Tm^{+3}, green emitting Er^{3+} and the orange emitting Nd^{3+} in ZnS. All these ions also have significant emission lines in the infrared region. We shall elaborate on these and other ZnS phosphors in the device section of this article. The infra-red properties of rare-earth ions are being actively researched for several applications including optical telecommunications, optoelectronic electronic integrated circuitry, lasers and sensors to name a few [37].

The second type of rare earth transition is an intra-shell 4*f*-4*f* transition [22,38]. This type of transition is seen in Er^{3+}, Tm^{3+}, and most other trivalent rare earths. The transitions are all parity forbidden and may have decay times typically of several ms. The spectra are characterized by line transitions, and are insensitive to the surroundings and symmetry of the ion since the 4*f* electrons are shielded by the 6*s* orbital.

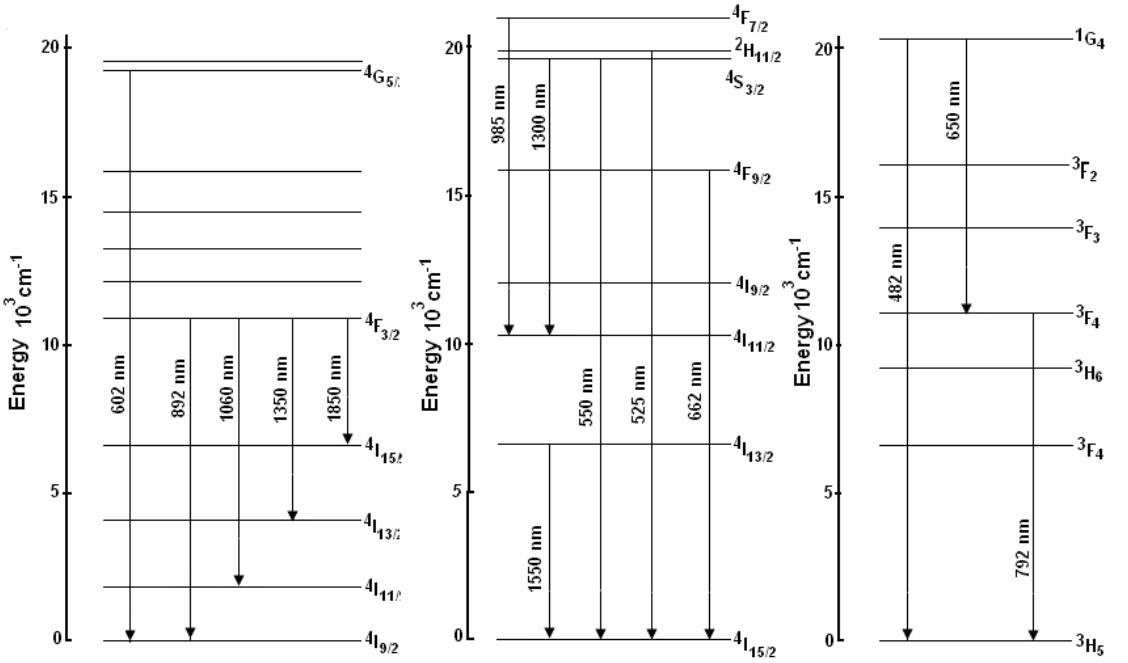

(Neodymium) (Erbium) (Thulium)

Fig.2.10: Energy level scheme for different rare earths [39, 40].

The excitation cross-section of the luminescent center – σ is discussed frequently in the literature [6, 15, 20, 24, 41]. This value relates the concentration of the centers to the mean free path for excitation through the simple relation,

$$l_i^{-1} = \sigma N , \qquad (2.12)$$

where N is the concentration of centers and l_i is the impact length. Some groups have directly measured the value for σ of Mn^{2+} in ZnS by measuring the efficiency and calculating the value from other known parameters [24]. The resulting value was similar to the physical ionic cross section. However, other efforts to predict impact cross sections for Mn^{2+} and other ions have shown that this is an extremely difficult task and accurate values are elusive [42], thereby impeding the ability to predict device efficiency. It is reported in the literature [20, 41] that it is desirable to have a large luminescent center impact cross section for good device efficiency, however there is not much practical value to this statement as the cross section has only been determined by measuring efficiency, and it is an intrinsic property of the atom.

2.3.5.3 Luminescent-center host-lattice systems

In addition to considering the electrical properties and processing conditions of the host and the luminescent properties of the center, one must consider the compatibility and interrelationships between the two. The size mismatch of the activator on the cation site is important, as is the valence match (or mismatch). Listed in Tab.2.3 are the valence and ionic radius of common ACTFEL host cations and dopants [43]. Minimizing the size and valence mismatch allows the incorporation of the dopant with the least concentration of induced defects.

Tab.2.3: List of valence and ionic radius for cations commonly used in ACTFEL hosts, as well as common dopant ions [43].

Ion	Radius [Å]	Ion	Radius [Å]	Ion	Radius [Å]
Zn^{2+}	0.74	Mn^{2+}	0.80	Tm^{3+}	0.88
Ca^{2+}	0.99	Ce^{3+}	1.03	Er^{3+}	0.95
Sr^{2+}	1.13	Tb^{3+}	0.92	Ho^{3+}	1.17
Dy^{3+}	0.62	Nd^{3+}	1.123		

Tab.2.4: Comparison of the visible characteristics of ZnS electroluminescent phosphors [43].

Phosphor material	Emission color	Color CIE coordinates	Subpixel luminance at 50 Hz (cd/m^2)	Luminous efficiency (lm/W)
ZnS:Mn	Yellow	x=0.50, y=0.50	600	5
ZnS:Mn/filter	Red	x=0.65, y=0.35	75	0.8
ZnS:Mn/filter	Yellow-green	x=0.45, y=0.55	80	
ZnS:Tb, F	Green	x=0.30, y=0.60	125	1.3
ZnS:Sm, Cl	Green	x=0.30, y=0.60	90	0.5-1
ZnS:Sm, F	Red	x=0.64, y=0.35	12	0.08
ZnS:Tm, F	Orange-red	x=0.60, y=0.38	8	0.05
ZnS:Mn/filter	Blue	x=0.15, y=0.15	< 1	< 0.01
SrS:Ce	White	x=0.42, y=0.48	450	1.6
SrS:Ce, Eu	White	x=0.41, y=0.39	36	0.2
CaS:Eu	Red	x=0.68, y=0.31	12	0.05
CaS:Ce	Green	x=0.27, y=0.52	10	0.1
$CaGa_2S_4$:Ce	Blue	x=0.15, y=0.19	13	0.04

The most commonly used and best performing visible EL phosphor system is Mn-doped ZnS. This phosphor can be filtered to obtain both green and red emission. To complete a full color display, there has been a tremendous amount of effort devoted to the development of a sufficiently bright and stable, saturated blue phosphor. Promising results were obtained for SrS:Ce. However the blue-green chromaticity and low luminance when filters are used were the primary limitations for this phosphor [15]. Nevertheless full color displays were developed based on this material. Promising results were also obtained for (Sr,Ca)Ga_2S_4:Ce, which had superior chromaticity, but lower brightness and greater difficulty in deposition and processing. Recently excellent performance has been demonstrated for blue-emitting SrS:Cu,Ag [44]. A list of results obtained for sulfide-based phosphors is given in Tab.2.4 [43, 44]. More details regarding these phosphor systems are available in the literature [15].

3 Experimental methods

To understand the result of the current study, previous studies of some optical and electrical characteristics of ACTFEL devices are shortly reviewed from the experiment point of view. The interested reader is also referred to the critical review article on this subject by Wager et al. [10] The methods used in this thesis will be displayed more in detail in following chapters. The structures of typical samples are also studied.

3.1 Standard measurements

The Figure 3.1 shows a block diagram of different set-ups used in this thesis for the measurement of optical and electric characterizations.

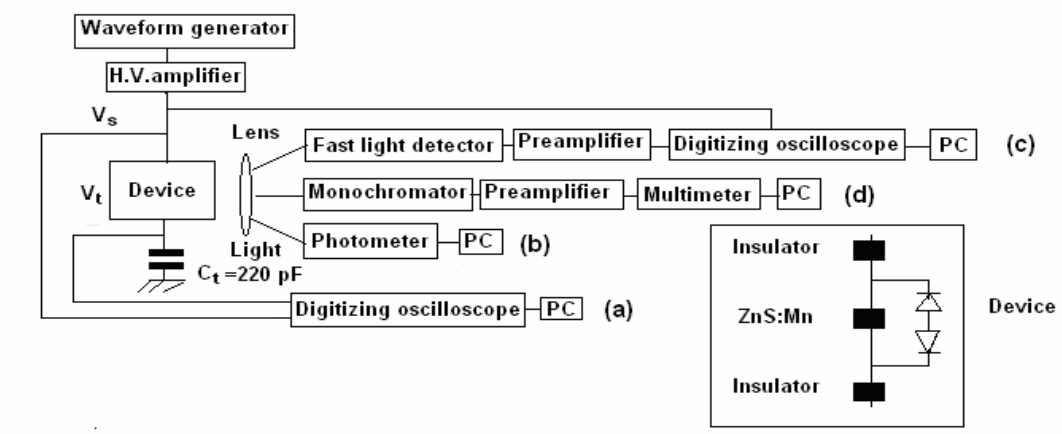

Fig.3.1: Block diagram of the different set-ups used in this work:
(a) *Q–V* loop evaluation, the typical equivalent circuit of the EL device is depicted in the detail;
(b) *L–V* characteristic and efficiency;
(c) Time relationship between V_s waveform and the EL light pulse;
(d) Emission spectra measurement.

Since the ACTFEL device is an optoelectronic device, it is necessary to measure certain properties in terms of optical parameters like

- luminance,
- luminous efficiency,
- emission spectrum,
- latent image,
- color of the light

as well as electric parameters such as

- charge-voltage (*Q*-*V*),
- capacitance-voltage (*C*-*V*),

- internal charge-phosphor field (Q_{int}-F_P) and
- maximum charge-maximum voltage (Q_{max}-V_{max}).

An important property of each ACTFEL device is its aging process.

3.2 Optical characterization

For practical applications, the optical output of EL devices is a critical parameter. Two systems units for quantifying optical output are used. Radiometric units are optical power units and can be used to quantify all electromagnetic radiation. These units quantify the photon flux density (radiant flux density) at a given wavelength. Optical power or irradiance is measured in W/cm^2.nm.

Photometric units can be used to quantify light only in the visible part of the spectrum. The photometric system takes into account the spectral response of the human eye. This response curve is called the luminosity curve for the standard observer (also known as the CIE curve). A brightness scale is the basic measuring element of the standard observer curve. That is, human observers were asked to rank by brightness various wavelengths of light of known flux density. The response curve can be interpreted as follows: A wavelength of 555 nm will appear brighter than any other wavelength of the same radiometric power. A source that can emit the same radiometric energy at 555 nm and 610 nm will appear only half as bright when operated at 610 nm as it does when operated at 555 nm. This relative brightness is known as the relative luminosity. Brightness is formally referred to as luminance.

The most important properties of an ACTFEL device are

- the intensity of the light output, [45]
- the power required to generate that light, and
- the color of the light.

As a result of this, the most commonly performed characterization experiments measure the luminance, the luminous efficiency, and the color spectrum of an ACTFEL device.

3.2.1 Optical experimental setup

The basic idea of electro-optical measurement is illustrated in Fig.3.2.derived from Fig.3.1. First, an applied DC voltage pulse is applied to the ACTFEL device to establish the band-bending shown. Next, electron-hole pairs are generated within ~ 40-60 nm [45] of the incident phosphor surface by a ultraviolet N_2 laser pulse (λ = 337 nm). The polarity of the applied voltage pulse determines whether electron or hole transport is expected to dominate.

The luminance of an ACTFEL display is a function of the peak voltage and frequency of the drive waveform, the intrinsic efficiency of the insulator-phosphor-insulator stack, and the operating history (aging). The efficiency is a function of the drive waveform shape and frequency as well as various device parameters. The emission spectrum is primarily determined by the phosphor host material and activators, although it is also affected by deposition and anneal conditions and in some cases by the drive voltage and frequency.

Latent image is the burning in of a permanent image of a fixed pattern which is displayed for long periods. It can appear as a faint dark image superimposed on a bright background or as a faint bright image superimposed on a dark background. Formation of latent image is affected primarily by drive waveform symmetry and device processing parameters. Display defects include pixel, line, and mural defects.

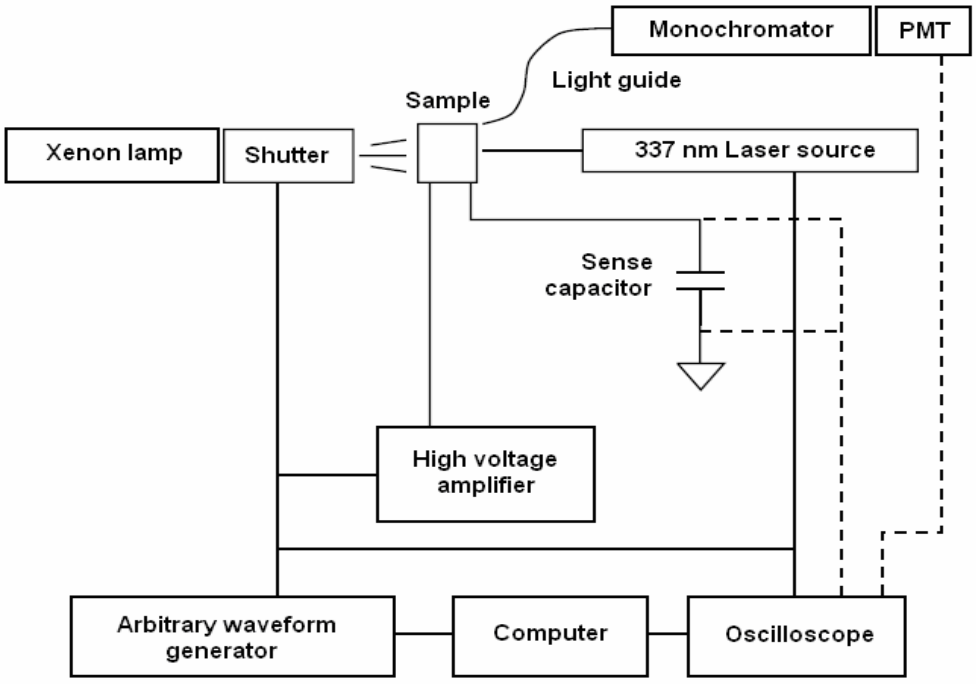

Fig.3.2: Typical optical measurement setup. Dashed lines denote measurement of the voltage across the sense capacitor and the voltage from the photomultiplier [45].

3.2.1.1 Electroluminescence (EL) measurement

Optical properties such as brightness, chromaticity and emission spectrum are routinely measured for all the deposited films. EL emission was excited by applying 2.5 kHz positive and negative trapezoidal voltage pulses, 30μs and 5μs in length with 5μs rise and fall times. The emitted light is analyzed with an Oriel MS257 0.25m monochromator using reflective optics. A chopper and lock-in detection scheme is used to improve the signal to noise ratio. A Si-based photomultiplier tube (PMT) (Oriel instruments, model 77345) attached to one of the exit ports on the monochromator was used to detect light up to 0.8μm, and a thermo-electric cooled Ge photodiode (Oriel instruments, model 71614) on a second exit port was used to detect light with wavelengths up to 2μm. An Oriel Merlin radiometry system controlled the chopper and was used to interface the monochromator and detectors with the acquisition software. The setup for the optical bench is shown in Fig.3.2.

3.2.1.2 Photoluminescence (PL) measurement

A Xenon lamp was used for the excitation source for PL. The excitation wavelength is selected with a source monochromator (Oriel Instruments, Cornerstone 260) between the lamp and the sample. The monochromator is capable of selecting wavelengths ranging from 200 nm to 1200 nm. PL measurements are carried out at room temperature in a dark room. The emission spectrum is collected from 300 nm to 1800 nm utilizing suitable detectors and monochromators (Oriel Instruments, MS257).

3.2.2 Luminance-voltage characterization

One measurement required to evaluate the performance of an ACTFEL device is the luminance-voltage (*L-V*) measurement, also known as the brightness-voltage (*B-V*) measurement. The *L-V* measurement is performed by measuring the light output of an ACTFEL device at applied voltages of increasing amplitudes until a predetermined stopping point is reached [11].

The first point is measured by applying a voltage waveform with amplitude below the threshold voltage, allowing the device to reach steady-state, and measuring the luminance with a photometer, photomultiplier tube, or photodiode, in a direction perpendicular to the substrate. The SI unit for luminance is candela per square meter (cd/m^2).

Electrons, which are the majority carriers in ACTFEL devices, tunnel out of the interface states on the left and into the conduction band. Once in the conduction band the electrons are accelerated by the large electric field, which is approximately 1 MV/cm = 100 kV/mm. The conduction electrons drift across the ZnS:Mn layer until they impact excite an Mn^{2+} center, transferring some energy to one of its electrons and causing it to undergo a transition to an excited state. The conduction electron may undergo additional collisions, eventually reaching the right interface and getting trapped in interface states there until the next voltage pulse, which is of the opposite polarity. This pulse causes the electrons to tunnel out and drift back across the ZnS:Mn layer, transferring energy to Mn^{2+} centers along the way, until eventually they are trapped again at the left interface. This transfer of charge back and forth between the interface states continues as long as the alternating polarity drive signal with peak amplitude above the threshold voltage of the device continues to be applied. Light emission occurs when the Mn^{2+} centers, which have been impact excited by the hot electrons, relax [6-8]. The light emission thus results from transitions of the electrons within the Mn^{2+} centers, rather than electron–hole pair recombination near a *pn* junction as occurs in a light-emitting diode (LED).

3.2.3 Photo-induced transferred charge (PIQ) and photo-induced luminescence (PIL)

Photo-induced transferred charge (PIQ) and photo-induced luminescence (PIL) measurements involve the creation of electron-hole pairs in the phosphor near one of the phosphor/insulator interfaces, transport of this photo-induced charge across the phosphor, and measurement of the charge transferred across the phosphor layer or the luminescence emitted from the phosphor layer, respectively, as a function of the

magnitude of the applied DC voltage. In PIQ/PIL experiments the electron and hole transport may be studied independently by simply changing the polarity of the DC bias. In ZnS:Mn alternating-current thin-film electroluminescence (ACTFEL) devices the hole transport may give rise to impact excitation-induced electroluminescence (EL), holes are approximately half as efficient as electrons in contributing to the transferred charge, and that the efficiency of transport is significantly greater for holes than electrons [11].

3.2.4 Electroluminescence emission spectrum and color coordinates

The color of the light emitted from an ACTFEL device is readily apparent to the observer, but the exact nature of the light source is not. Information about the properties of the luminescent center can be extracted by measuring the emission spectrum of the electroluminescence. The emission spectrum and color coordinates are also important from an industrial point of view for assessing the effectiveness of a phosphor for full color ACTFEL displays.

The emission spectrum is created by plotting the intensity of the emission as a function of wavelength. The energy of the transition(s) is then apparent from the value of the wavelength where the emission peaks. Also evident in the emission spectrum is the nature of the energy levels involved in the radiative transition in the luminescent center.

3.2.5 Transient brightness analysis

A less common optical ACTFEL characterization experiment is the transient brightness, or $b(t)$, measurement. In a $b(t)$ measurement, the optical output of an ACTFEL device is measured as the output current of a photomultiplier tube over the duration of an applied voltage pulse. In a $b(t)$ measurement, photon emission is observed as a function of time, so that it can be correlated with the applied voltage waveform, which yields information about various aspects of the operation of an ACTFEL device.

3.3 Electrical characterization

Measuring the optical output of an ACTFEL device is useful for evaluating its potential as a display product, but does not provide adequate information regarding the physics of device operation. More insight into the physics of ACTFEL operation is gained with the use of various electrical characterization techniques. This section describes electrical characterization techniques commonly used to investigate the physics of ACTFEL devices.

3.3.1 Electrical experimental setup

The electrical characterization circuit and attached measurement components comprising the experimental setup are shown in Fig.3.3. An arbitrary waveform generator is used to produce the driving voltage waveform. The waveform is amplified by a high voltage amplifier consisting of two Apex model PA-85 operational amplifiers and a switching network. The output of the amplifier drives the series combination of a protection resistor, the ACTFEL device, and a sense capacitor. The circuit used in this

setup is known as a Sawyer-Tower circuit [46]. The value of the sense capacitor, *C*, sense, should be about 100 times greater than the capacitance of the device being tested, so that most of the applied voltage is dropped across the ACTFEL device. The voltages v_2 and v_3 are measured using a digitizing oscilloscope (Agilent 54621 A).

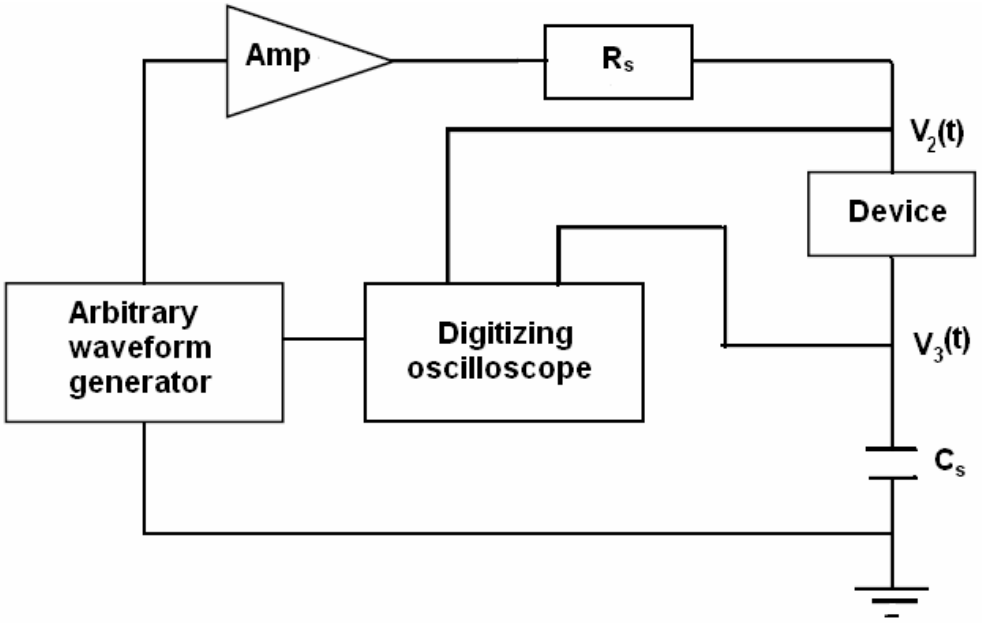

Fig.3.3: ACTFEL electrical characterization setup.

For electrical characterization of ACTFEL devices, the waveform used in this work is the bipolar trapezoidal waveform, shown in Fig.3.4. Typically, a waveform with rise and fall times of 5 μs and a 30 μs width is used. In order to match points in a data plot with points in the driving waveform, an A-L labeling scheme is used, as shown in Fig.3.4. The points C and I identify the voltage in the waveform where the device begins conducting charge, or the turn-on voltage.

Characterization measurements are usually taken after the ACTFEL device has established a steady state with the applied voltage waveform. Depending on the type of ACTFEL device being evaluated, the number of applied voltage pulses required to establish steady state varies from several to several hundred periods of the applied voltage waveform [10].

As the device structure shown in Fig.3.1 indicates, ACTFEL devices are capacitively coupled. Since only displacement current can flow across the insulator layers, the drive signal must be an alternating polarity waveform. A typical alternating polarity, trapezoidal waveform is shown in Fig.3.4.

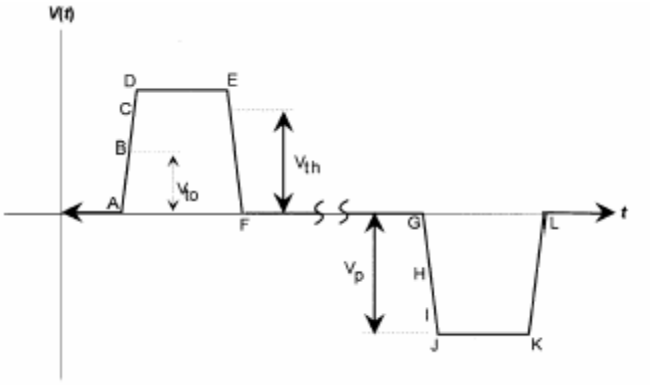

Fig 3.4: Typical alternating polarity, pulse drive bipolar trapezoidal waveform. Letters A–L mark points on the drive waveform, and are referenced later in Fig.3.5 and Fig.3.6. The pulse width would generally be about 30 μs and the frequency would be between 50 and 500 Hz for a passive matrix-addressed display.

3.3.2 Charge-voltage characterization

The basic technique for electrical characterization of ACTFEL devices is the charge-voltage (*Q-V*) measurement. If the external charge, *Q*, flowing into the ACTFEL device is plotted vs. the externally applied voltage, *V*, the resulting curve is called a *Q-V* loop [26, 47]. If the amplitude of the applied voltage pulses is less than the threshold voltage of the device, the *Q-V* loop is simply a straight line with slope equal to the total capacitance of the insulator-phosphor-insulator stack. If the amplitude of the applied voltage pulses is greater than the threshold voltage of the device, the *Q-V* loop opens up.

A *Q-V* plot is obtained by plotting the charge measured on the sense capacitor, $q_{ext}(t)$, normalized to the device area, versus the voltage measured across the device, $v_a(t)$. The external charge and applied voltage are given by

$$q_{ext}(t) = C_{sense} v_3(t) \tag{3.1}$$

and

$$v_a(t) = v_2(t) - v_3(t)\,, \tag{3.2}$$

where $v_2(t)$ and $v_3(t)$ are as shown in Fig.3.3. The charge *Q* plotted in a *Q-V* curve is the charge detected on the sense capacitor in the test circuit, not the actual charge inside the ACTFEL device at one of the phosphor/insulator interfaces. The voltage *V* in a *Q-V* curve is the voltage drop across the ACTFEL device, which is slightly different than the output of the high voltage output because some of the output voltage drops across the series resistor and the sense capacitor.

A *Q-V* curve assesses several physical parameters about ACTFEL devices. The amount of charge on the sense capacitor at various portions of a *Q-V* curve has physical meaning.

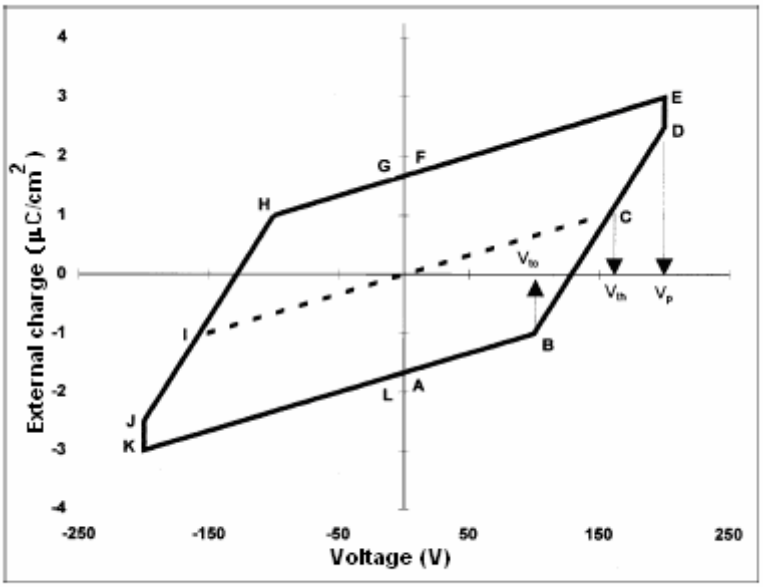

Fig.3.5: Idealized *Q-V* loop with no charge leakage from interface states between drive pulses. Letters A–L mark points on the *Q-V* loop which are coincident in time with the points labeled A–L on the drive waveform in Fig.3.4. The dashed line is the *Q-V* loop for the case just below threshold. The solid line is the open loop above threshold. The area of the *Q-V* loop represents the energy dissipated by the device per cycle of the drive waveform [47].

Q-V loop below and above threshold is shown in Fig.3.5 [47]. Above threshold, power is dissipated in the ACTFEL device. The area encompassed by the *Q-V* loop is equal to the energy delivered to the device per period of the drive waveform. The *Q-V* loop is measured directly. A theoretical extension of the *Q-V* loop that is sometimes used by researchers studying the physics of ACTFEL devices is a plot of the actual charge flow across a phosphor layer, Q_p, vs. electric field across the phosphor layer, F_p. The quantities required for a plot of Q_p-F_p can be calculated from the *Q-V* data if the thicknesses and dielectric constants of the insulator layers and phosphor layer are known. The actual charge flow across the phosphor is calculated by subtracting the reactive charge from the total charge. The field in the phosphor layer is calculated by adding the externally applied field to the internal polarization field due to the actual flow of charges across the phosphor layer. A Q_p-F_p loop corresponding to the above threshold *Q-V* loop of Fig.3.5 is shown in Fig.3.6 [47]. The Q_p-F_p loop is useful, because it expresses the internal electrical characteristics of the phosphor layer during device operation.

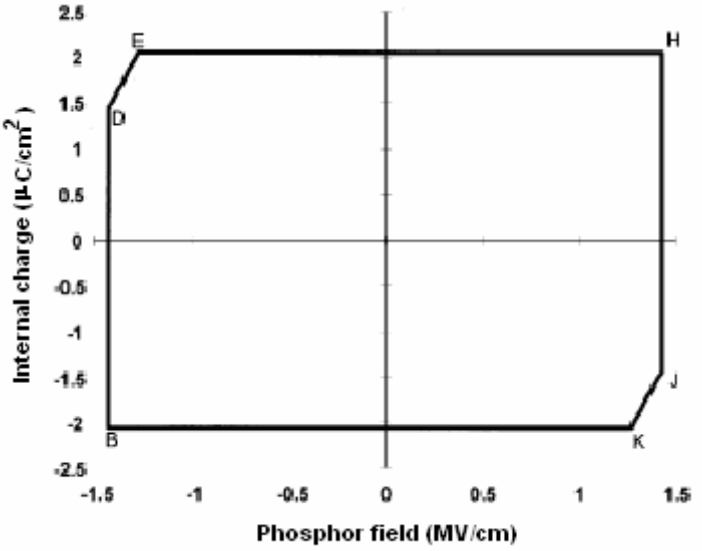

Fig. 3.6: Internal charge vs. electric field across phosphor layer Q_p-F_p loop corresponding to the above threshold Q-V loop in Fig.3.5. This loop represents the charge flow across the phosphor layer as a function of the electric field across the phosphor layer [47].

3.3.3 Luminance and efficiency

A schematic representation of a measurement system for collecting luminance and efficiency vs. voltage data on a test dot is shown in Fig.3.7 [11].

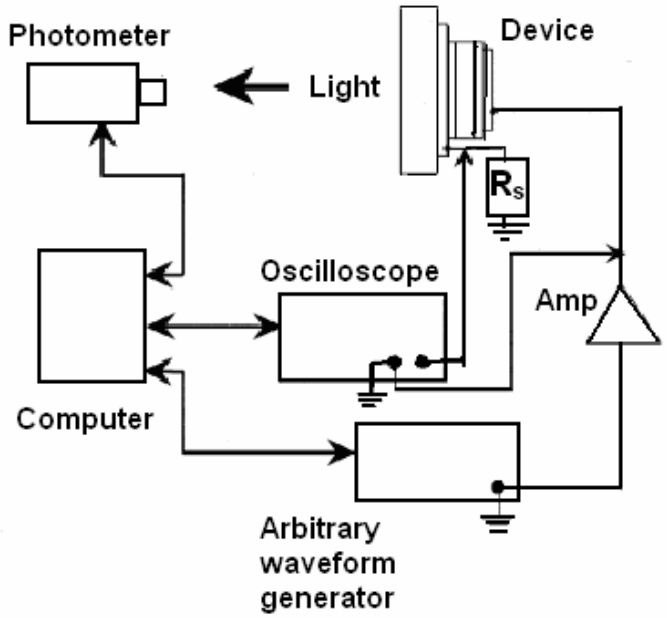

Fig.3.7: Schematic diagram of a system for measuring luminance and efficiency as functions of the peak drive voltage. The voltage waveform, $V(t)$, is measured by the oscilloscope at the Al electrode of the device under test. The current waveform, $I(t)$, is measured by the oscilloscope as the voltage across the sense resistor divided by its resistance. The luminance is measured by the photometer [11].

An arbitrary waveform generator provides a drive signal with the waveshape, frequency, and peak voltage determined by a control computer. The waveform generator output signal is amplified from a ± 5 V range to a ± 300 V range. A photometer, also under computer control, measures the luminance, L, of the test dot. An oscilloscope measures the voltage across the test dot and the voltage across the sense resistor. The current is calculated by dividing the voltage across the sense resistor by its resistance. The control computer can thus adjust the peak voltage up and down and collect the luminance data, as well as the waveforms representing the voltage across the test dot and the current through it. The energy dissipated, Ep, during each drive pulse is calculated as

$$E_p = \int_T I(t)V(t)dt, \tag{3.3}$$

where $I(t)$ and $V(t)$ are the current and voltage waveforms, respectively, and T is the duration of either the positive or negative drive pulse. This integration can be carried out by most oscilloscopes or the $I(t)$ and $V(t)$ data can be transferred to the control computer for the calculation, although this approach is generally slower. The average energy dissipated per period of the drive waveform, E, is the average of E_P for a positive pulse and a negative pulse. The average power dissipated, P, can be calculated by multiplying E by the frequency of the drive waveform.

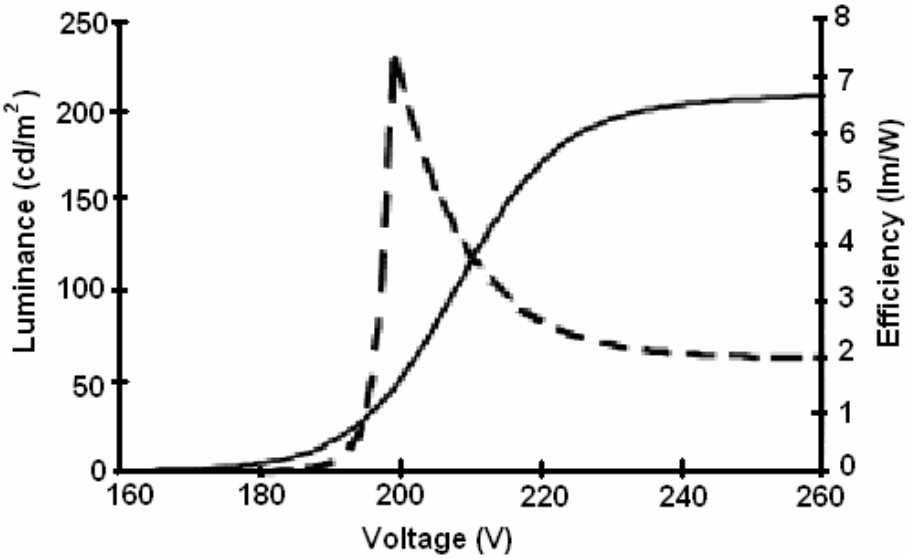

Fig.3.8: Plots of luminance and efficiency as functions of peak drive voltage. The solid line is the luminance and the dashed line is the efficiency.

3.3.4 Efficiency-voltage characterization

Another ACTFEL characterization procedure of interest is the efficiency-voltage (η-V) measurement. This measurement determines the luminous intensity of an ACTEL device per unit power consumed, or luminous efficiency, η, which has units of lumens per Watt (lm/W). The luminous efficiency is found from

$$\eta = \pi \frac{LS}{P}, \tag{3.4}$$

where L is the measured luminance in cd/m^2, S is the area of the test spot in m^2, and P is the average power in W. Values of L and η are collected for peak voltages ranging from 10 V below threshold to 40 or 50 V above threshold. Plots of L and η vs. peak voltage for a typical device are shown in Fig.3.8.

The luminous intensity is found by assuming the luminance is constant in all directions and integrating over all viewable angles. The power density is measured at the same time as the luminance and is found from

$$P = \frac{1}{S\tau}\int_{t}^{t+\tau} v(t')i(t')dt', \tag{3.5}$$

where S is the device area, τ is the period of the driving waveform, and $v(t')$ and $i(t')$ are the applied voltage and current waveforms, respectively.

3.3.5 Capacitance-voltage characterization

Capacitance-voltage (C-V) curves are created by plotting the dynamic capacitance of an ACTFEL device as a function of the voltage applied to the ACTFEL device during the rising edge of the applied voltage waveform [48]. The dynamic capacitance is the slope of the Q-V curve and is plotted for the rising edge of both the positive and negative portions of the applied voltage waveform. The dynamic capacitance is calculated from

$$C = \frac{i(t)}{\frac{dv_a(t)}{dt}}, \tag{3.6}$$

where

$$i(t) = \frac{dq_{ext}}{dt} = C_{sense}\frac{dv_3(t)}{dt}, \tag{3.7}$$

and $v_a(t)$ is as given in Eq.3.2. Substituting Eq.3.7 into Eq.3.6 gives the dynamic capacitance in terms of the differences of raw data values,

$$C = C_{sense}\frac{dv_3(t)}{dv_a(t)}. \tag{3.8}$$

3.3.6 Internal charge-phosphor field characterization

The internal charge-phosphor field (Q-F_p) technique was developed to obtain information about the device physics that is not obvious in a Q-V curve. A Q-F_p curve is obtained by plotting the instantaneous internal charge $q(t)$ versus the internal phosphor field $f_p(t)$ [49]. The internal charge and phosphor field are related to the external voltages and external charge by

$$q(t) = \frac{C_i + C_p}{C_i}q_{ext}(t) - C_p[v_2(t) - v_3(t)] \tag{3.9}$$

and

$$f_p(t) = \frac{1}{d_p}\left(\frac{C_{sense}v_3(t)}{C_i} - [v_2(t) - v_3(t)]\right), \tag{3.10}$$

where C_i is the insulator capacitance, C_p the phosphor capacitance, and d_p the phosphor thickness [11]. In contrast to a Q-V curve, a Q-F_p curve loops in a clockwise direction and the types of charge obtainable are all internal rather than both internal and external, and are therefore directly comparable. The Q-F_p curve also provides the average steady-state phosphor field, F_{ss}, while a Q-V curve does not. F_{ss} is the constant or nearly constant average phosphor field which exists in the device during the leading edge of the applied voltage waveform in which the applied voltage exceeds the turn-on voltage.

3.4 Aging characteristics

The importance of the aging characteristics of ACTFEL devices is underscored by the fact that device stability with aging tend to stabilize after a few tens of hours of burn-in, but can exhibit complex aging behavior during the burn-in process. The luminance vs. voltage curves for ZnS:Mn devices in which the phosphor layer is deposited by evaporation, for example, tend to shift to slightly higher voltage during burn-in [50]. Aging data is collected by measuring luminance vs. voltage at selected time intervals during aging. The measurement is carried out as described earlier for luminance vs. voltage measurements. The aging is done by continuously operating the device at a fixed voltage or at a fixed voltage above threshold. The aging process can be accelerated by operating the device at higher frequency or at higher temperature regime.

3.4.1 Time-resolved measurements

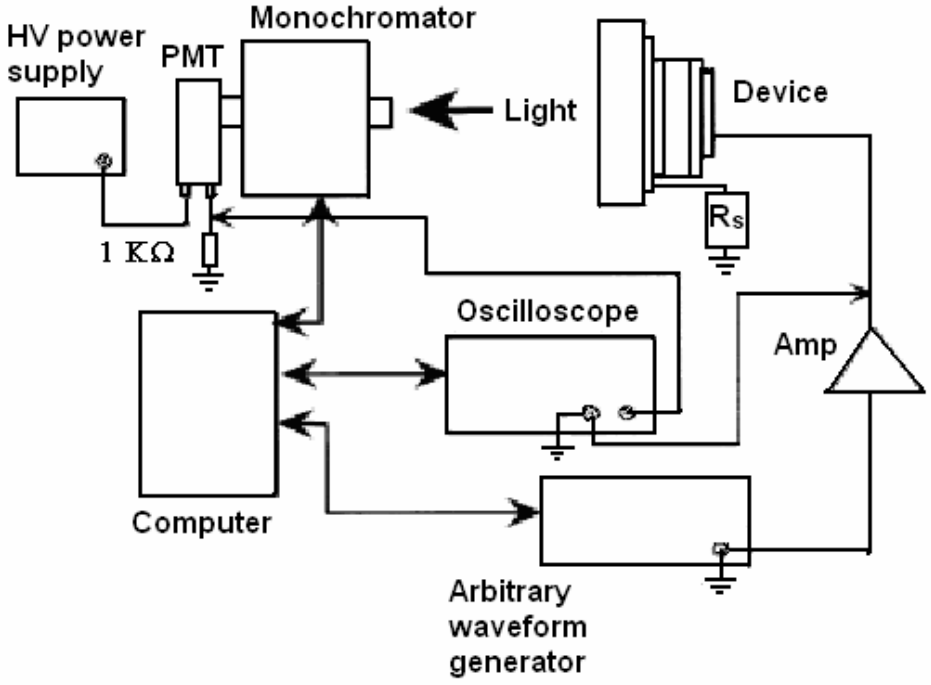

Fig.3.9: System for measuring the time-resolved emission spectrum of an ACTFEL device. The oscilloscope is set to integrate the light signal from the PMT during a selected time window. The monochromator wavelength is scanned over the entire spectral range and the emission intensity data is collected from the oscilloscope [50].

The set-up for measuring τ is shown in Fig.3.7. A photomultiplier tube (PMT) is used to detect the light emission as a function of time. The drive system is set to provide relatively narrow drive pulses, typically 10 μs pulse width, at relatively low frequency, typically 50 Hz. This approach works well for phosphors with relatively long decay times, on the order of 100 μs to a few milliseconds. This is the case for many common ACTFEL phosphors such as ZnS:Mn and ZnS:Tb. Phosphors such as SrS:Ce, however, have very fast decay times and cannot be measured in this manner. In such cases the photoluminescent decay time must be measured using a pulsed laser to excite the phosphor and appropriately low *RC* response time of the light detection system.

The general setup for measuring time-resolved emission spectra from ACTFEL devices is shown schematically in Fig. 3.9. The oscilloscope is triggered on the drive waveform and the signal integration period is set to the region of interest. A boxcar integrator can also be used to integrate the light signal during the desired time window. The monochromator wavelength is scanned and the emission spectrum is collected for the selected portion of the emission process.

4 Optical characterization - results and discussion

4.1 Measurement of emitted light

Several types of instruments are used for measuring light emission from ACTFEL displays. Photometers are used for luminance measurements. Spectrophotometers are used for measuring the emission spectrum and with suitable software can also provide luminance measurements. Time-resolved measurements are accomplished by using photomultiplier tubes or photodiode detectors. Table 4.1 lists some examples of photometers, spectroradiometers, photomultipliers, and photodiodes along with the names of the companies that manufacture them. A relatively new development for characterizing the light emission characteristics of flat panel displays, including ACTFEL displays, is the flat panel inspection system. This is a large measurement system comprising a CCD camera detector, light-tight enclosure, control computer, image processor, and specialized software. This type of system images an entire flat panel display on the CCD camera and measures luminance, chromaticity, and various defects by analyzing the image. These systems are intended for high throughput manufacturing environments and cost several hundred thousand dollars. An example of this type of system is also included in Tab.4.1.

Tab.4.1: Light measurement instruments.

Instrument type	Model	Manufacturer
Photometer	PR880	Photo Research
Photometer/spectroradiometer	PR650	Photo Research
	Pritchard 1980B	Photo Research
	GS-1280 RadOMAcam	Gamma Scientific (EG&G)
Photomultiplier tubes		Oriel Corp
		Hamamatsu
Photodiode	PIN 10AP	UDT Sensors, Inc
Flat panel inspection system	FIS 250	Photo Dynamics, Inc

4. 2 Luminance-voltage characterization

One measurement required to evaluate the performance of an ACTFEL device is the *luminance-voltage* (*L-V*) measurement, also known as the *brightness-voltage* (*B-V*) measurement [11]. Brightness, also known as luminance or photometric brightness, is the luminance intensity of any surface in a given direction. It is measured per unit of projected area of the surface as viewed from a single direction.

The *L-V* measurement is performed by measuring the light output of an ACTFEL device at applied voltages of increasing amplitudes until a predetermined

stopping point is reached. The first point is measured by applying a voltage waveform with amplitude below the threshold voltage, allowing the device to reach steady-state, and measuring the luminance with a photometer, photomultiplier tube, or photodiode, in a direction perpendicular to the substrate. The amplitude of the voltage waveform is increased and another measurement is taken, and so on until a sufficiently high voltage above threshold is reached. The *L-V* curve is obtained by plotting luminance on the y-axis and voltage on the x-axis, as shown in Fig.4.1.

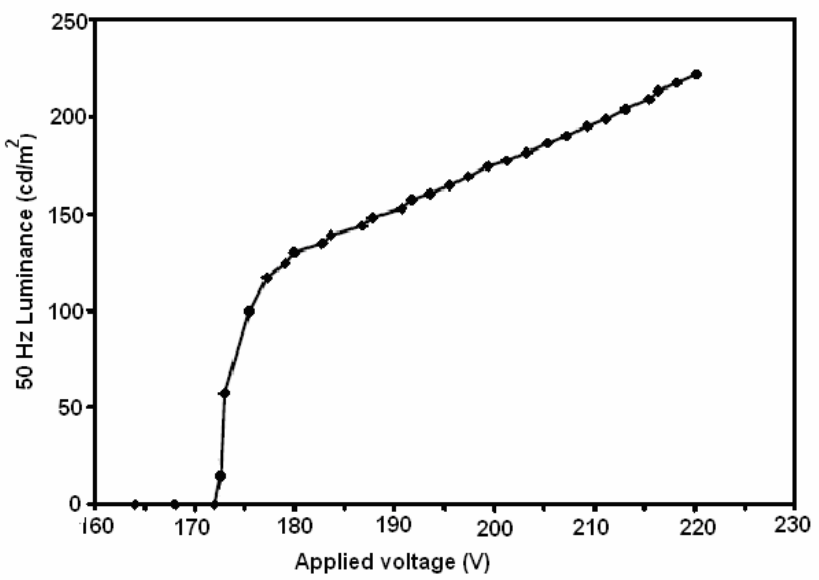

Fig.4.1: A luminance-voltage (*L-V*) curve for ZnS:Mn ACTFEL device driven by a 50 Hz bipolar trapezoidal waveform [11].

The *L-V* curve is dependent on several factors, and it is necessary to specify some of them when reporting results [51]. The measured luminance is dependent on the type of driving waveform, the shape of the waveform, and the frequency of the waveform. The fraction of time that the driving waveform spends above the turn-on voltage determines the luminance of the device. Thus, a driving waveform with a higher frequency or a shape such that the time above turn-on is greater will cause a higher luminance. The *L-V* curve is also dependent on the ambient temperature, the dopant concentration, and the thickness of the phosphor layer. When the temperature is increased, the probability of de-excitation through non-radiative recombination is significantly increased, which leads to reduced light output. Temperature also may affect the threshold voltage in an *L-V* curve since interface emission and space charge generation mechanisms are dependent on temperature [52]. Luminance increases with luminescent impurity dopant level for low concentrations. Increasing the density of luminescent centers raises the probability of an electron undergoing a collision with a luminescent center. This trend holds as long as the impurity concentration is low enough that phosphor crystallinity is maintained and concentration quenching does not occur. Increasing the phosphor layer thickness also increases the probability of electron impact excitation with an impurity. The threshold voltage is also affected by the phosphor thickness, since a higher voltage is required to achieve the threshold electric field in a thicker device.

4.3 Luminous efficiency-voltage characterization

Luminous efficiency is defined as the brightness divided by the consumed power. Fig.4.2 shows an η-V curve for a ZnS:Mn^{2+} device which phosphor layer was prepared by atomic layer epitaxy.

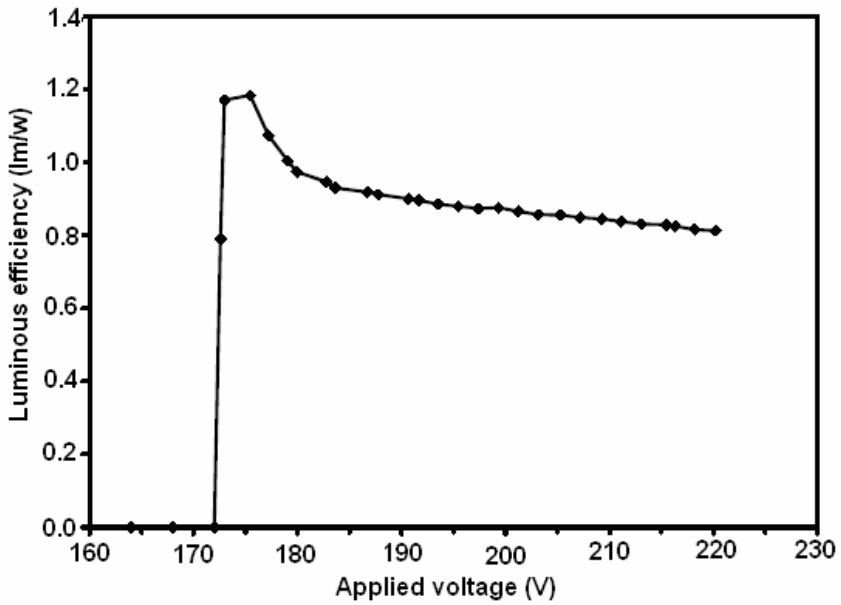

Fig.4.2: Efficiency-voltage (η-V) curve for a ZnS:Mn ACTFEL device driven by a 50 Hz bipolar trapezoidal waveform [6, 53].

Since the luminous efficiency is dependent on the luminance, it is influenced by most of the same factors. When contemplating the influences on the efficiency, it is useful to consider the interactions an electron may undergo in an ACTFEL device and the conditions required for the interactions to take place. Once an electron is in the phosphor, in order for EL to occur, an electron must impact excite a luminescent impurity, so the luminous efficiency is proportional to the excitation efficiency, η_{exc}

$$\eta_{exc} = \sigma N d, \tag{4.1}$$

where σ is the impact excitation cross section, N the dopant concentration, and d the phosphor layer thickness. This assumes that the field is large enough everywhere in the entire thickness d of the phosphor that the electrons have enough energy to impact excite the luminescent center. This is not the case if there is positive space charge present in the phosphor. The thickness of the active region, where there is a sufficient field for impact excitation, is reduced if space charge is present, which reduces η_{exc} and therefore the luminous efficiency η [53].

In addition to the luminance, the luminous efficiency also depends on the power input to the ACTFEL device. Thus if a factor that increases the brightness also increases the power consumption, such as the frequency of the driving waveform, then the efficiency is not increased. The change in luminance caused by a change in the driving frequency coincides with an increase in the power consumed, so the luminous efficiency does not increase with frequency. Luminous efficiency is affected in a similar way by

the device thickness. Thicker phosphor layers enhance the luminance, but also cause the threshold voltage to increase. This would require a higher operating voltage, which causes the power to increase, as evident from Eq. 3.5.

The measured luminance and luminance efficiency depend both on the type of driving waveform, the shape of the waveform, and the frequency of the waveform. They are also dependent on the ambient temperature, the dopant concentration, its grain dimensions and the thickness of the phosphor layer. When the temperature is increased, the probability of de-excitation through non-radiative recombination is significantly increased, which leads to reduced light output. Temperature also may affect the threshold voltage in an *L-V* curve since interface emission and space charge generation mechanisms are dependent on temperature. Luminance increases with luminescent impurity dopant level for low concentrations. Increasing the density of luminescent centers raises the probability of an electron undergoing a collision with a luminescent center. The investigation of the luminescent dopant dimension on the luminance will be a subject of further study.

4.4 Photo-induced transferred charge (PIQ) and photo-induced luminescence (PIL)

Photo-induced transferred charge (PIQ) and photo-induced luminescence (PIL) measurements have been employed for the non-standard electro-optic characterization of evaporated ZnS:Mn ACTFEL devices with probe layers in which only certain regions of the phosphor were Mn-doped [11]. The PIQ/PIL experiments involve a creation of electron-hole pairs in the phosphor near one of the phosphor/insulator interfaces, the transport of this photo-induced charge across the phosphor and measurement of the charge or the EL emitted from the phosphor layer, respectively, as a function of magnitude of the applied DC voltage.

4.4.1 Principle

The basic idea underlying a PIQ/PIL measurement is illustrated in Fig.4.3. First, an applied DC voltage pulse is applied to the ACTFEL device to establish the band-bending shown. Next, electron-hole pairs are generated within ~ 40-60 nm [54] of the incident phosphor surface by an ultraviolet N_2 laser pulse (λ = 337 nm). The polarity of the applied voltage pulse determines whether electron or hole transport is expected to dominate. The PIQ signal is determined as the transferred charge across a sense capacitor connected in series with the ACTFEL device. The magnitude of the PIQ signal is established by the number of photo-generated carriers and the distance that each carrier travels. The PIL signal is the measured luminescence due to the photo-induced carriers transiting the phosphor.

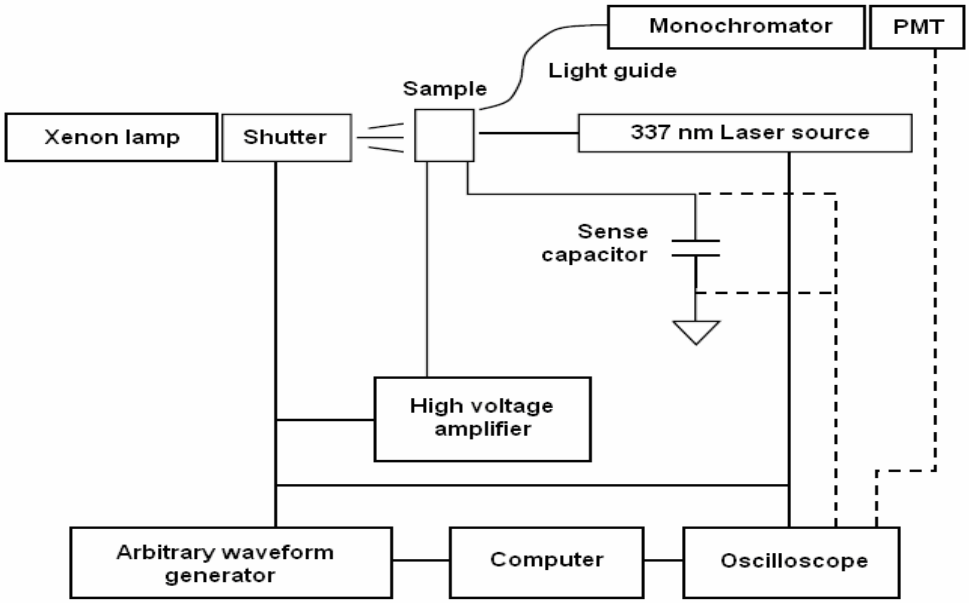

Fig.4.3: PIQ/PIL measurement setup. Dashed lines denote measurement of the voltage across the sense capacitor and the voltage from the photomultiplier [55].

4.4.2 Experimental and results

The sample used in this study consists of a standard ACTFEL structure with SiON top and bottom insulators, evaporated ZnS:Mn as the phosphor layer, an indium-tin oxide bottom contact, and aluminum top contact. The top and bottom insulator thicknesses are approx. 110 nm and 180 nm, respectively. Phosphor thickness is 950 nm. For PIQ/PIL experiments, an ~15-nm-thick semi-transparent layer of aluminum is thermally evaporated onto the sample so that a small portion of this layer overlaps neighboring thick aluminum dots, but the majority of the thin contact covers the uncontacted ACTFEL stack. The purpose of this semi-transparent aluminum layer is to allow ultraviolet laser radiation to pass through the thin contact, creating electron-hole pairs in the phosphor, and yet to allow carriers to be collected via the semi-transparent contact.

4.4.2.1 Photo-induced luminescence

Figure 4.4 represents a PIL curve for an ACTFEL device. A distinct PIL threshold is evident at a phosphor field of approximately 100 MV/m. This threshold corresponds to the average phosphor field at the onset of either:

1) band-to-band impact ionization or
2) Mn impact excitation.

We prefer to attribute the measured PIL threshold to (1), since there is no PIQ or PIL evidence for a second threshold corresponding to the onset of band-to-band impact ionization and we believe that an important condition for efficient ACTFEL operation is that the threshold field for band-to-band impact ionization be less than or equal to the threshold for impact excitation, thus leading to electron multiplication of electrons sourced from interface states. Additionally, the PIL curve shown in Fig.4.4 has a base line offset which is due to the photo-luminescence (PL) response of the device.

The PL response is the light produced by the laser exciting the phosphor in the absence of an electric field-induced response. The PIL threshold is observed for holes as well as electrons. This threshold is attributed to a hole trapping-induced back-injection of electrons from the opposite interface. Thus, the hole PIL signal shown in Fig 4.4 is an artifact which does not actually arise from hole transport.

Finally, one can observe that the PIL signal peaks and then decreases at increasing voltages. This is also believed to be an artifact arising from the difference curve analysis used to estimate PIL. Therefore, the data points for voltages greater than that of the peak voltage are not meaningful and the PIL peak is not significant.

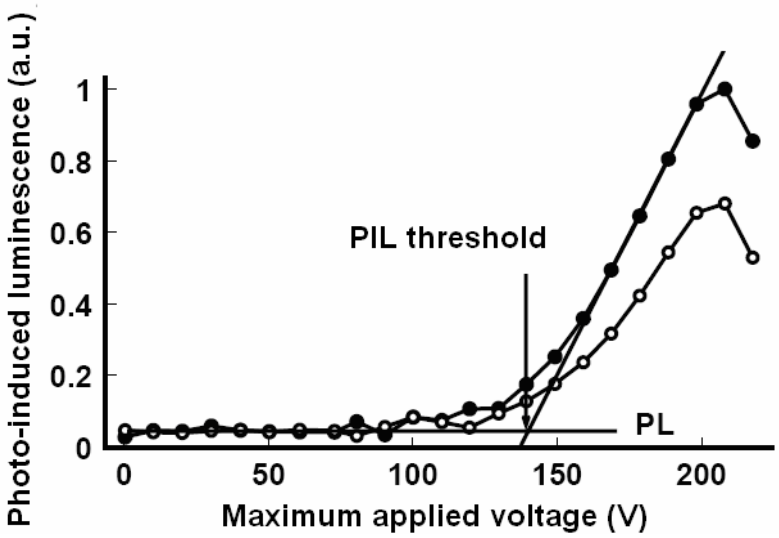

Fig.4.4: PIL curves for ZnS:Mn^{2+} ACTFEL device. • - electrons, o – holes [55].

4.4.2.2 Photo-induced transferred charge

The PIQ curves shown in Fig.4.5 for the ACTFEL device are interesting in several respects. First, it is puzzling why the electron PIQ signal increases monotonically over the entire range of the maximum applied voltage. Since the PIQ signal magnitude is determined by the number of carriers transported times the distance that they travel before being trapped, one would expect the PIQ signal to saturate at small applied voltages below threshold, once a sufficiently large drift field is established to move the photo-induced carriers across the phosphor layer. The monotonically increasing nature of the electron PIQ signal is attributed to a voltage-dependence of carrier extraction from the photo-induced electron-hole plasma [56].

The second interesting feature [55] of the PIQ curve shown in Fig.4.5 is that the slope of the hole PIQ curve is smaller than the slope of the electron PIQ curve below ~125 V (~80 MV/m). This suggests that holes are not as efficient as electrons at traversing the phosphor for fields below ~80 MV/m. In contrast, above ~125 V the electron and hole PIQ curve slopes are identical. The identical PIQ slopes above ~125 V is attributed to hole trapping and back-injection of electrons, as discussed in the previous paragraph. Moreover, if hole trapping is postulated to account for differences

in the PIQ electron and hole PIQ slopes for fields below ~80 MV/m, it is possible to estimate the following quantities: a trapped hole concentration of ~1-5×10^{23} m^{-3}, a hole drift length of ~180-70 nm, a hole lifetime of ~2 ps, and a hole trap capture cross-section of ~7×10^{-17} m^2. The extremely large magnitude of this hole capture cross section is particularly revealing since it corresponds to a negatively charged deep level trap whose charge state leads to very efficient hole capture because of the coulombically attractive interaction between the trap and the hole. It is likely that this hole trap is a defect complex involving a zinc vacancy.

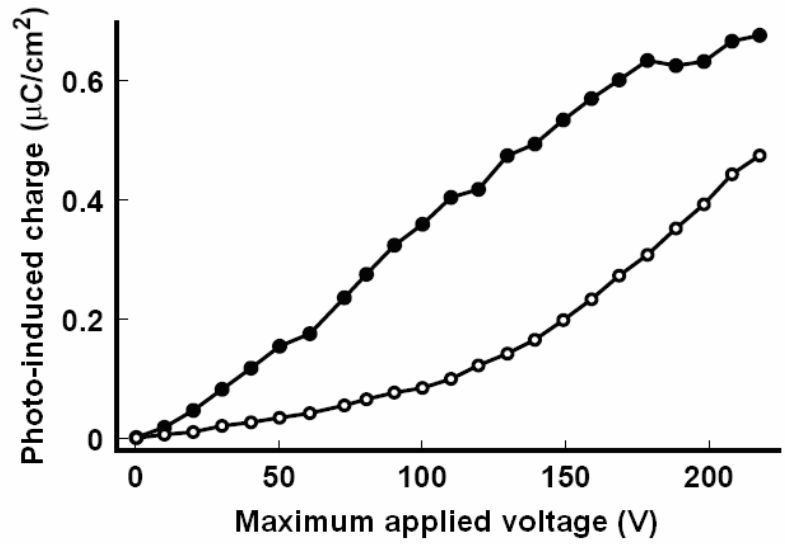

Fig.4.5: PIQ curves for ZnS:Mn^{2+} ACTFEL device. • - electrons, o – holes [55].

4.4.2.3 Conclusion

PIQ/PIL experiments done on this sample show that electron and hole transport may be studied independently by simply changing the polarity of the DC bias. In ZnS:Mn^{2+} ACTFEL devices the hole transport may give rise to impact excitation-induced electroluminescence, holes are approximately half as efficient as electrons in contributing to the transferred charge, and that the efficiency of transport is significantly greater for holes than electrons. The fact that photo-induced hole efficiency is greater than the photo-induced electron efficiency was very surprising. This result can be interpreted as arising from differences in the electric field profile in the phosphor for the cases of hole and electron transport. The further study suggests that hole transport is not effective in ZnS, and that what appears to be hole-induced effects are actually due to whole trapping-induced back injection of electrons.

4.5 Photo-induced charge and hole drift length measurement

4.5.1 Experimental

The PIQ experimental set-up is shown in Figure 4.3 [57]. The ultraviolet radiation is generated by a nitrogen laser at a wavelength of 337 nm pumping a dye laser tuned to 500 nm, which then passes through a doubling crystal to create 250 nm wavelength pulses of 2-3 ns duration. Since the band gap of ZnS is 3.7 eV (330 nm), this photon energy is sufficiently large to create electron-hole pairs by band-to-band generation. The DC voltage applied to the ACTFEL device is generated by an arbitrary-waveform generator (Wavetek model 395) and amplified by a high-voltage amplifier.

The PIQ signal is measured by means of a 100-pF sense capacitor in series with the ACTFEL device via a digitizing oscilloscope (Tektronix model TDS 420A).

The samples used in this study consist of a standard ACT FEL structure with SiON top and bottom insulators, evaporated ZnS:Mn as the phosphor layer, an indium-tin oxide bottom contact, and aluminum top contact. The top and bottom insulator thicknesses are approximately 110 nm and 180 nm, respectively, for all three of the ACTFEL devices used in this study. Phosphor thicknesses are 300, 700, and 950 nm. For PIQ experiments, an ~15-nm-thick semi-transparent layer of aluminum is thermally evaporated onto the sample so that a small portion of this layer overlaps neighboring thick aluminum dots, but the majority of the thin contact covers the uncontacted ACTFEL stack. The purpose of this semi-transparent aluminum layer is to allow ultraviolet laser radiation to pass through the thin contact, creating electron-hole pairs in the phosphor, and yet to allow carriers to be collected via the semi-transparent contact.

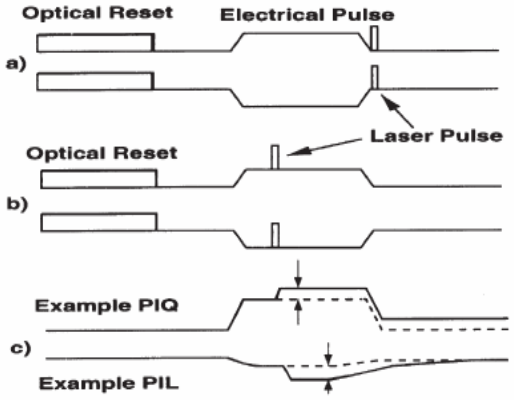

Fig.4.6: Timing diagram of pulse sequence. a) No laser pulse occurs during the voltage pulse. b) A laser pulse occurs during the voltage pulse. c) Example of the PIQ signals with (solid line) and without (dashed line) the laser pulse applied during the voltage pulse [57].

In the experiment, the PIQ signals are measured as a function of the magnitude of the applied voltage across the ACTFEL device. In order to obtain more meaningful data, we found it desirable to optically reset the phosphor field to a flat-band condition between each voltage pulse. To accomplish this, a xenon lamp is used to apply an optical reset pulse between each DC voltage/laser pulse.

A timing diagram for the PIQ measurements is shown in Fig.4.6 [57]. The ACTFEL device is first reset with a 10 s optical reset. Next, a positive voltage pulse with 5 μs rise and fall times and a 100 μs plateau is applied. 30 μs after the beginning of the electrical pulse, a 3ns laser pulse is applied. The maximum charge induced on the sense capacitor and the integrated area of the PMT signal (the total light output) generated by the device for that pulse are stored via computer acquisition. The ACTFEL device is then optically reset again and a negative voltage pulse is applied. Once again, the maximum charge induced on the sense capacitor and the light produced are stored.

For each maximum applied voltage, two sets of PIQ data are acquired. The first set of data is obtained when the voltage pulse is applied in the absence of a laser pulse (Fig.4.6a), while the second set is obtained when both the voltage pulse and the laser pulse are applied (Fig.4.6b).

These two sets of data are then subtracted from one another in order to isolate the photo-induced PIQ signals. After acquisition of four sets of data, the two sets described above for both positive and negative applied voltages, the maximum applied voltage of the pulse is increased and the process is repeated. PIQ data are taken in 5 V steps from 0 V to 20-40 V above threshold for three different ZnS:Mn phosphor thicknesses.

4.5.2 Results and discussion

The primary experimental results of this study are presented in Figure 4.5 in which PIQ is plotted as a function of the maximum voltage applied to the ACTFEL device with phosphor thickness of 950 nm. The PIQ curves for the ACTFEL devices with phosphor thicknesses of 700 and 300 nm exhibit trends similar to those shown in Fig.4.5.

The PIQ curves for the ACTFEL device with a phosphor thickness of 950 nm (Fig.4.5) clearly show a region below ~125 V where the holes are not as efficient at traversing the phosphor. In contrast, above ~125 V the electrons and holes have approximately the same transport efficiency, since the slope of the PIQ curve above 125 V is the same for both electrons and holes (*i.e.,* the slope of a PIQ curve can be viewed as a transport efficiency) ACTFEL devices with phosphor thicknesses of 700 and 300 nm exhibit trends similar to those shown in Fig.4.5 in which the hole PIQ efficiency distinctly increases above a certain applied voltage. The voltage above which the PIQ efficiency increases is ~75 and ~50 V for ACTFEL devices with 700 and 300 nm thick phosphor layers, resp. The voltage at which the transport efficiency changes, corresponds to an internal phosphor field of ~0.8 MV/cm for all three ACTFEL devices. The value of 0.8 MV/cm obtained from the PIQ experiment is an average field across the phosphor; the cathode field is significantly larger if space charge is present, as discussed below. We interpret these PIQ results to suggest hole trapping in the phosphor for lower fields; the transport efficiency of holes is less than that of the electrons since a significant fraction of the photo-injected holes are trapped in the phosphor, while the electrons transit the phosphor layer with very little trapping.

If hole trapping and backside electron injection is invoked to explain the observed apparent increase in the hole PIQ efficiency for phosphor fields greater than ~80 MV/m, it is possible to estimate the trapped hole concentration ρ. This is accomplished by assuming a cathode field of 220 MV/m [57] and using

$$\rho = \left[F_{\mathrm{p}}^{\mathrm{cathode}} - F_{\mathrm{p}}^{\mathrm{measured}}\right]\frac{2\varepsilon_{\mathrm{p}}}{d_{\mathrm{p}}}, \tag{4.2}$$

which implicitly assumes a uniform distribution of trapped holes. Use of (4.2) yields an estimated ρ of 1-5×10^{23} m^{-3} for both ACTFEL devices tested. These estimates do not seem unreasonable since they are somewhat larger than the 7×10^{22} m^{-3} estimates of the static space-charge density for evaporated ZnS:Mn ACTFEL devices. A drift length for holes may be estimated from the PIQ measurement. If the electrons are assumed to transit completely across the phosphor, then at a given voltage, the ratio of the hole PIQ to the electron PIQ multiplied by the phosphor thickness of the device should yield an estimate of the average distance that holes travel prior to being trapped (*i.e.* the drift length) at that applied voltage.

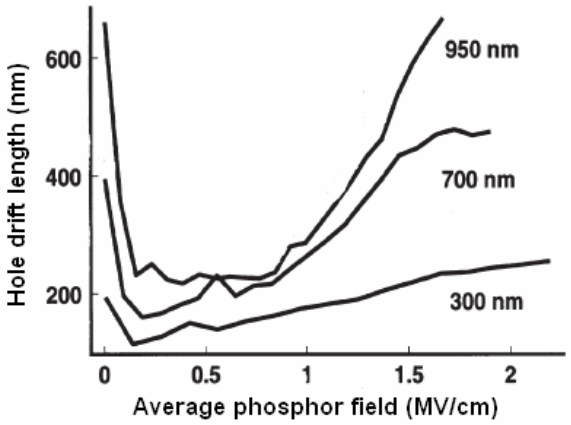

Fig.4.7: Hole drift length versus average phosphor field for evaporated ZnS:Mn ACTFEL devices with phosphor thickness of (a) 950 nm, (b) 700 nm, (c) 300 nm [57].

Figure 4.7 is a plot of the drift length as a function of the internal phosphor field. Note that the lowest field points plotted in Fig.4.7 are not reliable because of the PIQ uncertainties. Also, the upward trend in the hole drift length of Fig.4.7 for phosphor fields greater than ~0.8 MV/cm arises from the onset of backside electron injection, not from an enhancement in the hole drift length. Thus, taking the relatively constant, low-field portion of Fig.4.7 as a measure of the drift length, the hole drift length is estimated to be 180 ± 70 nm. If holes are assumed to travel at a saturated drift velocity of ~10^7 cm/s, then the drift distance can be used to deduce an average hole lifetime of ~2 ps. Furthermore, if the hole trap density is assumed to be 7×10^{22} m^{-3} [57], the hole trap capture cross section can be estimated from

$$\sigma = \frac{1}{\tau v_{\mathrm{sat}} N_{\mathrm{t}}} \sim 7 \times 10^{-17}\ \mathrm{m}^2, \tag{4.3}$$

where τ is the hole lifetime, v_{sat} is the saturated drift velocity, and N_{t} is the trap density. Capture cross-sections of calculated magnitude correspond to a coulombically attractive interaction between a trap and the carrier to be trapped [58]. Thus, the large magnitude of this capture cross-section suggests that the trap is negatively charged prior to hole capture. We speculate that this hole trap is a zinc vacancy or, more likely, a zinc vacancy complex, since a zinc vacancy is a double acceptor. More work is required to conclusively identify the physical nature of this hole trap.

4.5.3 Conclusion

Photo-induced charge (PIQ) and hole drift length measurements of evaporated ZnS:Mn ACTFEL devices with variable phosphor thicknesses provide information related to the transport of electrons and holes in the ZnS phosphor. Hole PIQ curve trends are dominated by hole trapping. Hole trapping is characterized by a drift length of ~(180±70) nm, a hole lifetime of ~2 ps, and a trap capture cross-section of $\sim 7\times10^{-13}$ cm^2. This is a large capture cross section, corresponding to a negatively charged deep level trap whose charge state leads to very efficient hole capture due to the attractive coulombic interaction between the trap and the hole. We speculate that this hole trap is most likely a defect complex involving a zinc vacancy.

4.6 Dependence of brightness and threshold voltage upon phosphor thickness

Memory ACTFEL devices show hysteresis in their brightness-voltage (*B*-*V*) response curve [53]. The hysteresis voltage margin, ΔV, and saturation brightness B_s, can be considered as the figures of merit for memory ACTFEL displays. In operating a memory ACTFEL device, we usually apply a sustaining AC voltage, V_s (root-mean-square value), which is normally adjusted so as to be in the vicinity of the centre portion of the hysteresis region [10]. Initially, the device has low brightness operating at V_s. It can be turned 'on' by increasing the excitation voltage to $V_{ON} \sim V_s + V_0$ and turned 'off' by reducing V_s, at voltage V_0. The optimum value of V_0 is usually chosen so that V_{ON} reaches the 'knee' point voltage in the device's B-V response curve.

From a device and even an equipment point of view, hysteresis in *B*-*V* response curve is the most important advantage of ACTFEL devices for large-area applications. In spite of the fact that the brightness of a memory-type EL, in general, is lower than that of non-memory ones [4], their advantage lies in the possibility of operating on an arbitrary number of pixels in the matrix addressing mode at the same brightness level as the one-pixel device. Thus, memory devices are potentially more suitable for large area display operation.

A pronounced hysteresis effect in the brightness vs. pulse width (*B*-*W*) response curve for memory ACTFEL devices driven near the threshold voltage has also been found and its use to address memory EL displays was suggested. Therefore, on the basis of these investigations we have inspected the dependence of the B-W characteristics on the film thickness of the ZnS:Mn layer. The variations of the response times with respect to these parameters were also studied. The first results are reported in this paper.

4.6.1 Experimental

The studied ACTFEL devices represent the structure composed of layers of SiO_2 (150 nm), Y_2O_3 (300 nm), ZnS:Mn (various thickness from 200 to 900 nm), Y_2O_3 (300 nm), SiO_2 (150 nm) deposited onto an indium-tin-oxide (ITO) coated glass substrate.

The experimental setup used in the measurement is shown in Fig.4.8. The samples were mounted in a thermal chamber, and driven by the voltage provided by the high-voltage pulse shaper. DC or AC pulses with variable durations and voltages could be generated.

All electro-optical measurements are taken by using our standard experimental setup, in which the ACTFEL device is placed in series with a resistor and a large sense capacitor. For brightness-pulse width (*B-W*) measurements, a 150 Hz AC voltage with square-pulse widths ranging from 20 μs to 200 μs was applied (waveform generator Agilent 33220A in conjunction with a high-voltage operational amplifier 7265 DSP). The emitted light brightness was measured as a function of the pulse width, for a given peak-to-peak voltage, using an Ocean Optics PR-650 digital photometer. For the response-time measurements, a Hamamatsu type R928 photomultiplier tube (rise time ~ 25 ns) was used to detect the pulsed-light output. The voltage pulse and optical response were monitored on an Agilent 54621A digitizing oscilloscope and the results were plotted on a recorder [46, 59].

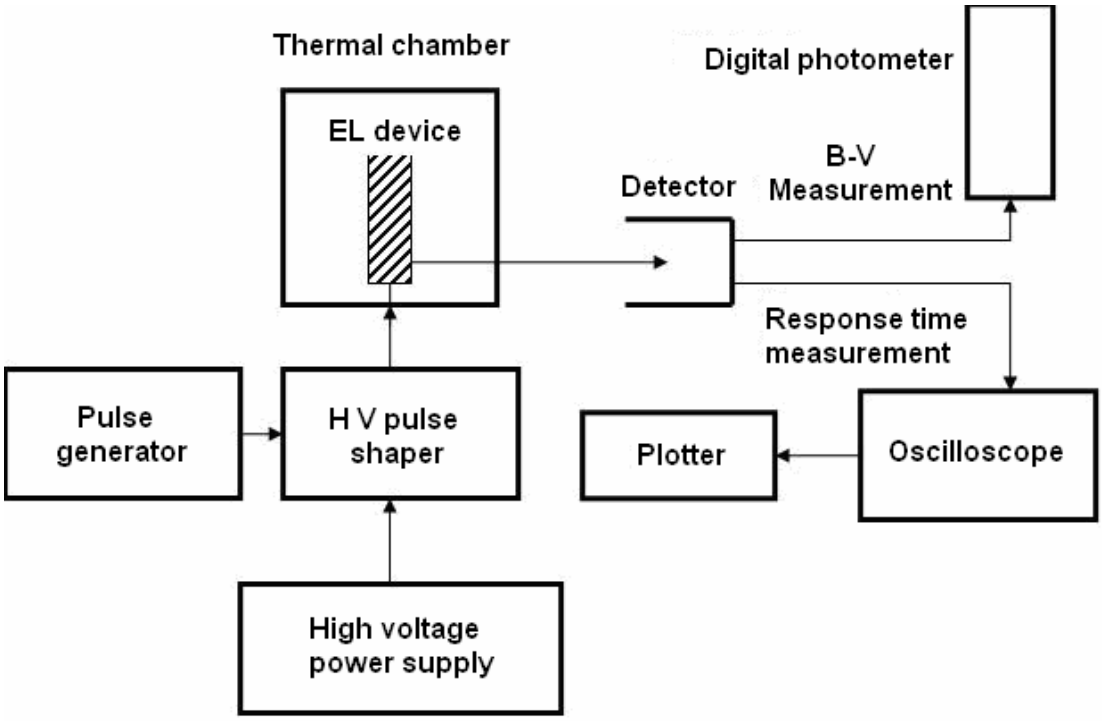

Fig.4.8: Experimental setup for measuring the electro-optical characteristics of ACTFEL devices [59].

4.6.2 Results and discussion

As an example of obtained results, the measured relations of the B-W response curves at various peak-to-peak voltages for the ZnS:Mn film thickness of 600 nm are shown in figure 4.9. As can be seen, a pronounced hysteresis effect is observed for the device driven near the threshold voltage.

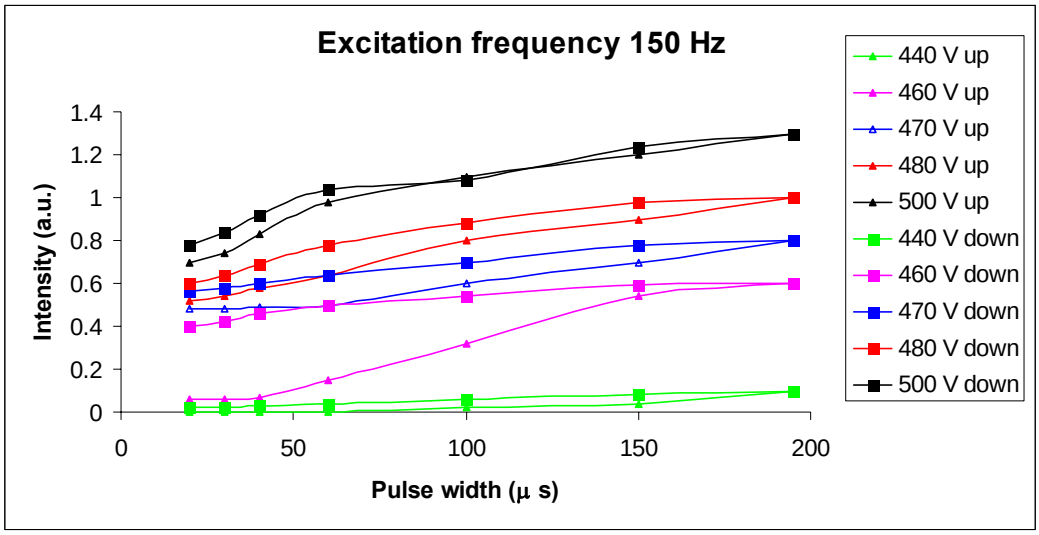

Fig.4.9: Measured relation of the brightness versus pulse width (*B-W*) at various peak-to-peak voltage of the memory EL device at excitation frequency 150 Hz [59].

Let the brightness margin, ΔB, be defined as the hysteresis width at pulse width 20 μs, the observed variations of ΔB and the threshold voltage with respect to the ZnS:Mn film thickness are shown in Fig.4.10. It is noted from Fig.4.10 that the hysteresis appears only if the ZnS film is thicker than 200 nm. Above it, the hysteresis width ΔB increases with the film thickness.

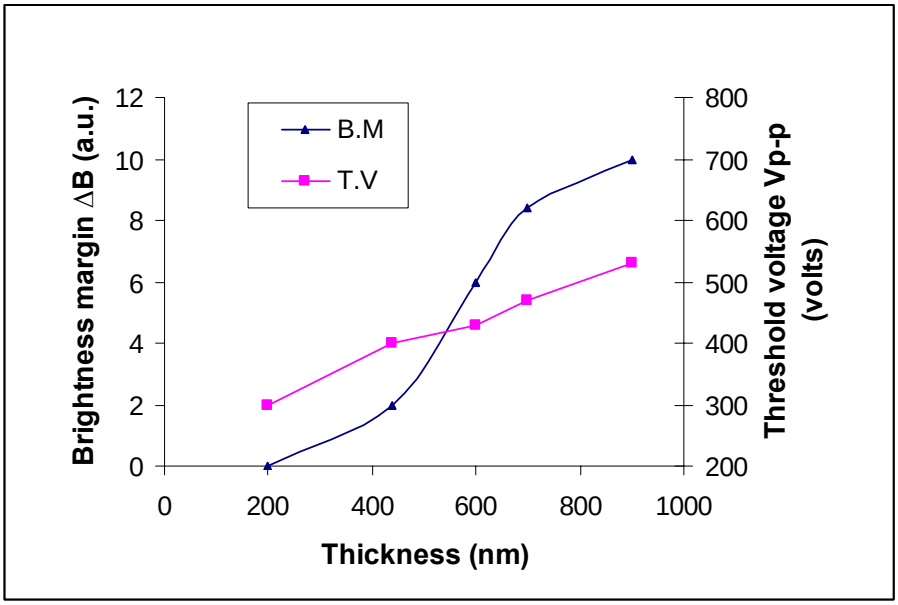

Fig.4.10: Observed variations of brightness margin, ΔB (curve B.M) and threshold voltage $V_{p\text{-}p}$ (curve T.V) with respect to the film thickness of ZnS:Mn layer [59].

It is also noted from Fig.4.10 that the threshold voltage of these devices changes dramatically from one device to another. Within the experimental error, the threshold voltage was found to increase approximately linearly with the ZnS film thickness. This result is understandable. Experimentally, it has been proven that the excitation

mechanism in ZnS:Mn EL devices is due to the direct impact excitation of the activator ions of Mn^{2+} by 'hot' electrons [60]. These electrons were originally trapped at the active (ZnS)-insulator (Y_2O_3) interface states. At high enough applied voltage, they tunnel from the interface states into the conduction band of the active layer. They are subsequently accelerated by the high electric field and the impacts excite the activator ions, Mn^{2+}. Light is emitted as the ions undergo radiative decay from the excited state to the ground state [45]. As a result, the threshold voltage is related primarily to electron tunneling which is induced by the electric field ($E = V/d$) inside the layers. Therefore, the threshold voltage should increase as the thickness of the ZnS film increases.

It should also be noted from Tab.4.2 that the rise-time and the decay-time are not equal. It is known that the rise-time is controlled by the crystalline properties of the ZnS:Mn layer.

Tab. 4.2: The measured results of the rise-time (T_r) and the decay-time (T_d) for ZnS:Mn EL devices having various thickness of the active layer.

ZnS:Mn layer thickness (nm)	Device	T_r (μs)	T_d (μs)
300	D_1	75	105
450	D_2	81	111
600	D_3	80	100
750	D_4	84	105
900	D_5	78	108

Electrons reach the excite-impact energy faster in large grained ZnS:Mn thus decreasing the device's rise-time. The decay-time, on the other hand, is determined by the radiation decay time of luminous centers Mn^{2+} from their excited state. According to this picture, the rise-time should be independent of the ambient temperature, and the decay-time should not. The decay-time T_d can be written as

$$\frac{1}{T_d} = \frac{1}{T_{ir}} + \frac{1}{T_{inr}} , \tag{4.4}$$

where T_{ir} is the internal radiative decay-time, T_{inr} is the internal nonradiative decay time. The major nonradiative decay process for an excited Mn^{2+} ion is most likely due to energy transfer to the so-called 'killer' centers in the ZnS lattice which do not allow the phosphor radiation [60]. These centers may be associated with impurity atoms, or with defects in the ZnS lattice (e.g. vacancies, dislocations, etc).

4.6.3 Conclusion

An experimental study of the brightness-pulse width characteristics of memory ZnS:Mn ACTFEL devices is presented, in which memory of the device is assessed by monitoring the hysteresis characteristics.

From the obtained results we can conclude two important notices:

1) The hysteresis appears only if the ZnS film is thicker than 200 nm. Above it, the hysteresis width ΔB increases with the film thickness.

2) The threshold voltage is related primarily to electron tunneling which is induced by the electric field (E = V/d) inside the layers. Therefore, the threshold voltage should increase as the thickness of the ZnS film increases.

4.7 Electroluminescence brightness and luminous efficiency of ZnS:Mn doped with KCl

The electroluminescence (EL) characteristics of ZnS:Mn doped with KCl for alternating current thin film electroluminescent devices deposited by a RF sputter system from ZnS and Mn targets are investigated.

4.7.1 Experimental

The devices used in this study were normally configured ACTFEL devices consisting of a Corning 7059 glass substrate coated with 300nm of indium tin oxide (ITO) and 220nm of aluminum titanium oxide (ATO) layers. The ZnS:Mn phosphor layer was deposited using two independently operated RF planar magnetron sources with a dense CVD intrinsic ZnS and a metal Mn target, respectively. The ZnS source was operated continuously at 150 W, while the Mn source was operated at 60 W, 5% duty cycle (Fig.4.11). The substrates were on a 180 °C holder that rotated every 11 s. The chamber pressure for argon was held at 2.66×10^{-4} Pa, and the thickness was controlled to be 1000 nm. For co-doped samples, KCl was then thermally evaporated onto the surface of the phosphor layer at room temperature, and diffused in via rapid thermal annealing (RTA) by heating to various temperatures for 5 minutes in a 99.999% nitrogen flow. After any residual KCl was rinsed off by deionized water, 200 nm aluminum reflective electrodes were deposited by thermal evaporation at a chamber pressure $< 2.66\times10^{-4}$ Pa.

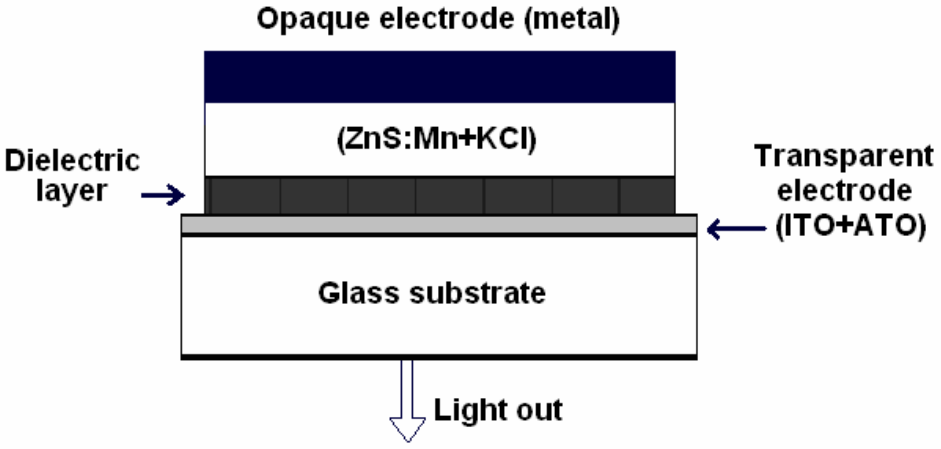

Fig.4.11: Schematic of stack EL device used in this study.

Grain morphologies and defect structures were characterized using transmission electron microscopy (TEM) on a JEOL 200CX, operating at 200 kV. Both cross sectional and plan-view samples were studied. A PhotoResearch PR-650 spectrophotometer was used to measure the EL brightness, CIE coordinates and spectral distribution. The AC waveform used for measurement had rise and fall times of 5μs and

a holding time was 30 μs. A frequency of 50 Hz was used for all testing. EL efficiency was measured using a Sawyer-Tower circuit (Fig.3.3) [46].

4.7.2 Results and discussion

The structure with parallel grains (equiaxed) from as deposited ZnS:Mn is shown in Fig. 4.12 by TEM photo-micrographs taken from an ACTFEL device [60]. In Fig.4.12a, a layer of very fine equiaxed grains (10 nm grain diameter, 100 nm thick) is observed close to the insulator/phosphor interface. The grain boundaries of most of the columnar grains in the balance of the cross section are barely definable. The columnar grain diameter measured by the mean linear intercept from plan-view TEM photomicrographs is 90 nm. Contrast bands in the columnar grains are obvious. After a rapid thermal annealing (RTA) at 700°C for 5 min, KCl co-doped ZnS:Mn phosphor exhibited enhanced columnar grain growth (to a grain diameter of 190 nm) which also consumed the equiaxed grain layer at the ZnS/ATO interface (Fig. 4.13). The density of the contrast bands was still high in this sample, independent of whether or not KCl was co-doped. Finally, KCl co-doped ZnS:Mn thin films annealed to $T \approx 900$°C resulted in very large grains which approached equiaxed geometries with diameters >1 μm.

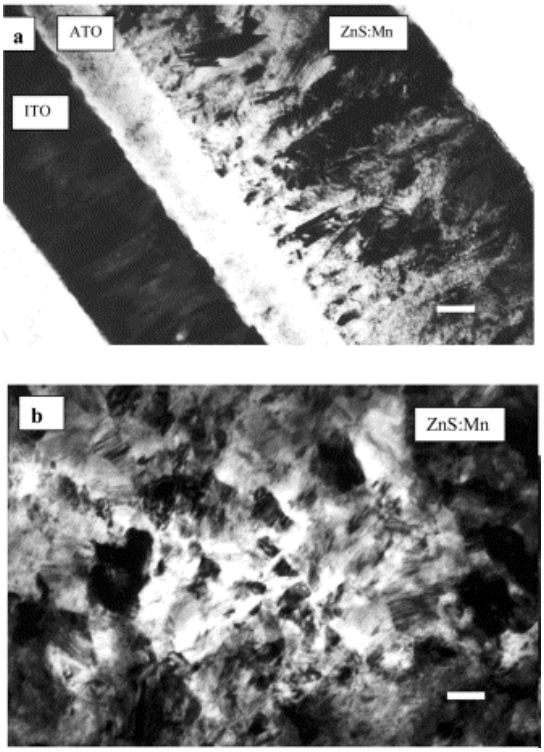

Fig.4.12: TEM micrographs taken from the ACTFEL device with as-deposited ZnS:Mn phosphor [60].
(a) cross-section,
(b) plan-view (bar=100nm).

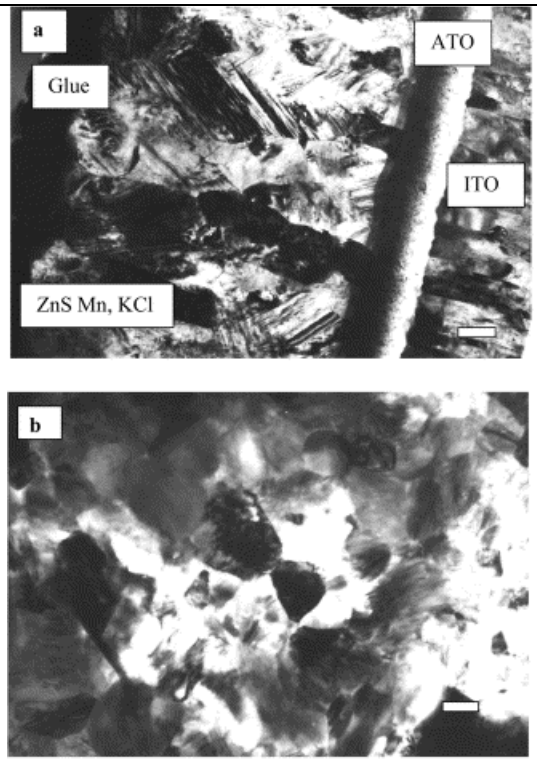

Fig.4.13: TEM micrographs from ZnS:Mn, KCl after 5min of annealing at 700°C [60].
(a) cross-section,
(b) plan-view (bar=100nm).

The luminous efficiency and brightness from samples as-deposited or annealed at 700°C with or without KCl are plotted in Fig.4.14. In all cases, the brightness first increases almost linearly with the applied voltage, then tends to saturate in the high

voltage regime. This behavior is characteristic of ZnS:Mn devices [61]. Data in Fig.4.14 also show that the slope of the *B–V* curve from KCl doped sample is larger than for undoped samples, indicating a sharper turn-on behavior. Neither annealing nor incorporation of KCl changed the color of ZnS:Mn thin films, since all the EL emission spectra exhibit a peak at 580–584 nm, and no changes in CIE coefficients are detected.

Because the Mn^{2+} concentration was optimized and uniformly distributed in as-deposited films, the low brightness and relatively high threshold voltages are ascribed to the heavily defected sputter deposited microstructure. The 100 nm thick layer of 10 nm equiaxed grains (see above) could be a 'dead layer' for hot electrons. For 2–3 eV electrons, the mean free path is ≈ 10 nm based upon numerical Monte Carlo simulation [19]. This is equal to the average grain size in the equiaxed layer. If the grain boundaries were hot electron scattering centers, they would reduce the number of 'hot' electrons and therefore the EL intensity. In addition, the poor resolution of grain boundaries in as-deposited films suggests that a large concentration of point defects may be present. It is logical to assume that these point defects would lead to both scattering and non-radiative recombination, further reducing EL brightness and efficiency. This is especially true since the 3*d* orbitals of Mn^{2+} ions, where the recombination occurs, are not shielded from the ZnS host. The point defects could create relatively shallow band gap states that would allow injection of charge into the ZnS conduction band at low fields. This hypothesis is consistent with the weak 'turn-on' shown in Fig.4.14. The increase in EL brightness upon annealing without KCl is ascribed to improved crystallinity at both the ATO/ZnS interface and in the columnar grains, as evident from grain growth and improved resolution of the grain boundaries. Although no direct experimental observations of the type and density of point defects are available, most defects should be annealed out after 5 min at 700°C, since this corresponds to a homologous temperature of 0.6 (i.e. is at 60% of the melting point of ZnS in K). At this homologous temperature, rapid diffusion is expected to lead to the destruction of point defects and reduction of non-radiative pathways, with consequent improvement in brightness.

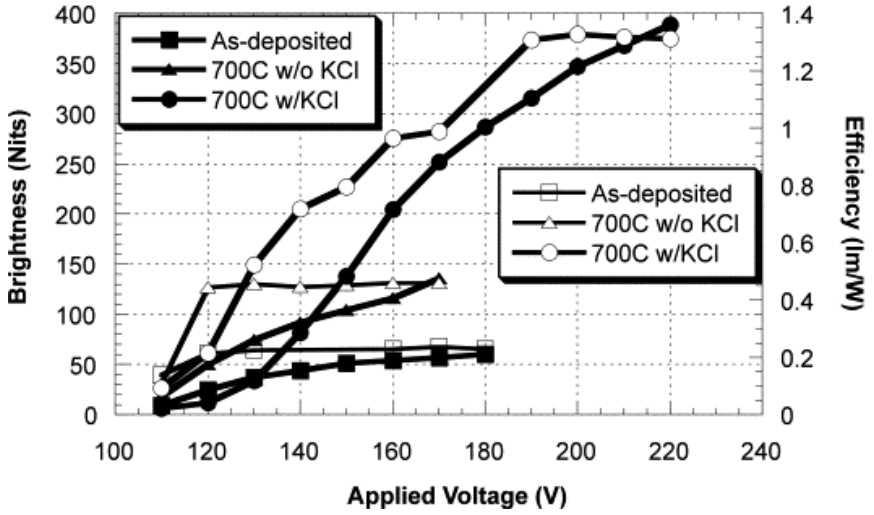

Fig.4.14: Effects of RTA and KCl co-doping on EL brightness (solid symbols) and luminous efficiency (open circles).

Annealed samples doped with KCl exhibited higher threshold voltages, significantly improved EL brightness, and a much sharper turn-on behavior. The small equiaxed grains at the ZnS:ATO interface were eliminated and even more grain growth was observed than for anneals without KCl co-doping. These further improvement in crystallinity with KCl co-doping during annealing would be expected to lead to better EL brightness, because it also results in less space charge, which is believed to be associated with reduced hole trapping at V_{Zn}–Cl complexes. Less space charge should result in hotter electrons with higher energy, which results in improved EL efficiency. Improved crystallinity cannot explain the increased threshold voltage and sharper turn-on, which must be related to the existence of K^+ interstitial and/or Cl^- substitutional ions. Both K^+ interstitials and substitutional Cl^- in ZnS:Mn can be donors. If their energy states are sufficiently far from the conduction band, a relatively high electric field is required to ionize them. In addition, since they should have a well defined energy state, a much sharper turn-on behavior is expected. The extra donors increase the hot electron population, which contributes to higher EL brightness.

4.7.3 Conclusion

The effects of KCl co-doping on the microstructure and the EL properties of ZnS:Mn phosphors have been investigated. At temperatures of 700°C, incorporation of KCl improves the crystallinity of the ZnS:Mn phosphors by enhancing grain growth in the columnar grains and causing them to consume a 100 nm layer of equiaxed fine grains at the ATO/ZnS interface. In addition, KCl co-doping allows growth of grains to diameters > 1 μm at $T \approx 900$°C. The potassium diffused through the ZnS film at $T \geq 600$°C in 5 min, and exhibits a small activation energy. Based on these observations and its ionic size, it is postulated that the potassium occupies interstitial sites in cubic ZnS, and therefore acts as a donor in the lattice. Co-doping with KCl improves the brightness and efficiency by ≈100%, and increases the threshold voltage and makes the slope of the *B*–*V* plot much larger. The EL data show that while improved crystallinity may reduce non-radiative recombination, the most important effects of KCl co-doping are a reduction of space charge and band bending with a resulting larger, hotter electron population in the EL phosphor.

5 Electrical characterization – results and discussion

In this chapter, we do not use the most common *V-A* characteristics, because other ones are more important in the study of ACTFEL devices.

For measurement of drive voltage and current digital oscilloscopes are used for all of the electrical measurements described in this chapter. Suitable instruments are available from several manufacturers, including Tektronix and Hewlett-Packard. A bandwidth of 100 MHz is more than sufficient. Waveform analysis capabilities are very helpful but not absolutely necessary. Interfaces RS 232 or IEEE 488 are required for computer control and data transfer.

5.1 Charge-voltage characterization

A *Q-V* curve assesses several physical parameters about ACTFEL devices. The amount of charge on the sense capacitor at various portions of a *Q-V* curve has a particular physical meaning. These charges are labeled in Fig.5.1. Q_{cond} is the conduction charge transported across the phosphor during the voltage pulse, which impact excites luminescent centers and gives rise to light emission.

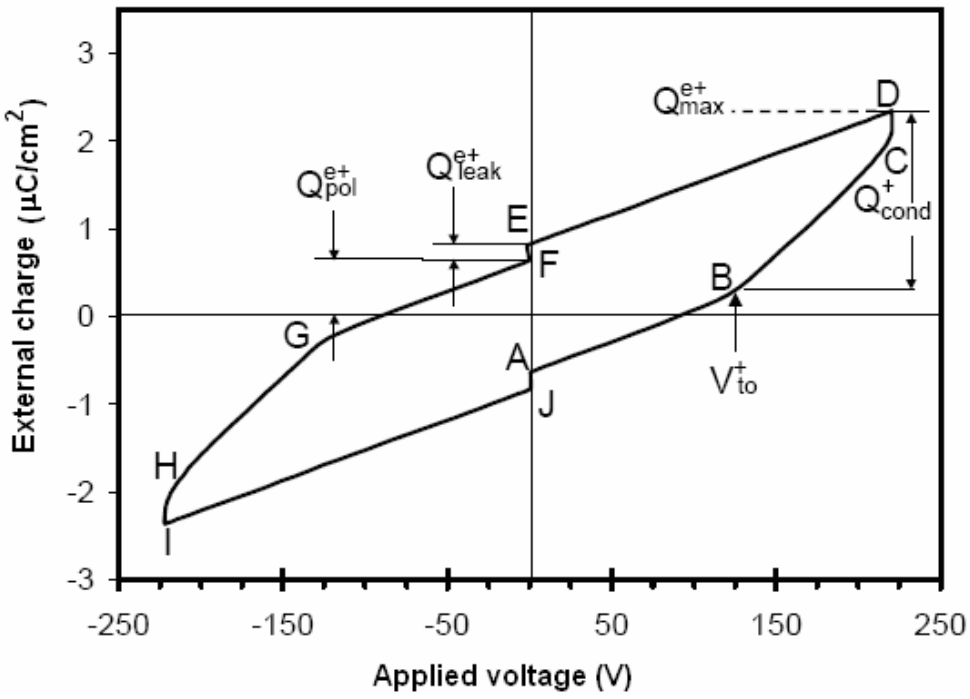

Fig.5.1: *Q-V* curve for an evaporated ZnS:Mn ACTFEL device [60].

Figure 5.1 shows a hysteresis loop brought about by application of a sinusoidal waveform driving voltage. The charge that flows through the phosphor during the portion of the waveform at which the applied voltage is constant at its maximum value, V_{max}, and the phosphor field decreases, or relaxes, is the relaxation charge, Q^{e}_{relax}. Q^{e}_{leak} is the leakage charge resulting from the emission of electrons from shallow interface states during the portion of the waveform where the voltage is zero. The polarization charge, Q^{e}_{pol}, is the charge stored at the phosphor/insulator interface just prior to the onset of the ensuing pulse of opposite polarity. The charge labeled Q^{e}_{max} in Fig.5.1 is the maximum external charge and corresponds to the maximum voltage measured across the sense capacitor for a given applied voltage. Also apparent in a *Q-V* curve are the two turn-on voltages, V_{to}, the positive turn-on voltage being marked in Fig.5.1. The turn-on voltage often differs for positive and negative portions of the *Q-V* curve because of polarization charge [62].

The magnitude of polarization charge, and therefore the turn-on voltage, depends on V_{max}. The turn-on voltage should not be confused with the threshold voltage, V_{th}, which is the lowest value of V_{max} at which the phosphor begins to conduct electric charge for the first time and when significant light emission is initiated.

A *Q-V* curve loops in a counter-clockwise direction, as observed in Fig.5.1 [60]. The A through J labels correspond to the labels of the driving waveform (Fig.3.4). The point labeled A in Fig. 5.1 corresponds to the onset of a positive voltage pulse applied to the top electrode. The charge value at point A is nonzero because of polarization charge residing on the phosphor/insulator interfaces, which is left behind from the previous pulse of opposite polarity. The portion of the *Q-V* curve below the turn-on voltage (the portions labeled AB and FG in Fig.5.1) has a slope equal to that of the total capacitance of the series combination of the insulator and phosphor layers of the ACTFEL device. From point B to point C, the phosphor is conducting and is effectively shorted, and the slope is ideally equal to the physical capacitance of the series combination of the two insulators, C_i. The slope of the BC (and GH) portion of the *Q-V* curve can become much larger than C_i if there is a generation of positive space charge in the phosphor layer during this time [60]. From point C to point D, the applied waveform is constant at its maximum value and the increase in charge is relaxation charge. During the DE portion of the *Q-V* curve, the applied voltage decreases to zero; this is the trailing edge portion of the voltage waveform.

The EF segment is the time between the end of the positive portion of the waveform and the beginning of the rise of the negative polarity pulse. The process repeats with the external applied voltage having negative polarity in the F to A portion of the curve.

5.2 Capacitance-voltage characterization

Capacitance-voltage (*C-V*) curves are created by plotting the dynamic capacitance of an ACTFEL device as a function of the voltage applied to the ACTFEL device during the rising edge of the applied voltage waveform [48]. The dynamic capacitance is the slope of the *Q-V* curve and is plotted for the rising edge of both the positive and negative portions of the applied voltage waveform. The dynamic capacitance is calculated from

$$C = \frac{i(t)}{\frac{dv_a(t)}{dt}}, \tag{3.6}$$

The quantity C in Eq. 3.6 is plotted against $v_a(t)$ to generate a *C-V* curve.

C-V curves for an evaporated ZnS:Mn ACTFEL device are shown in Fig.5.2 taken with driving waveforms of maximum amplitude 20, 40, and 60 V above V_{th}.

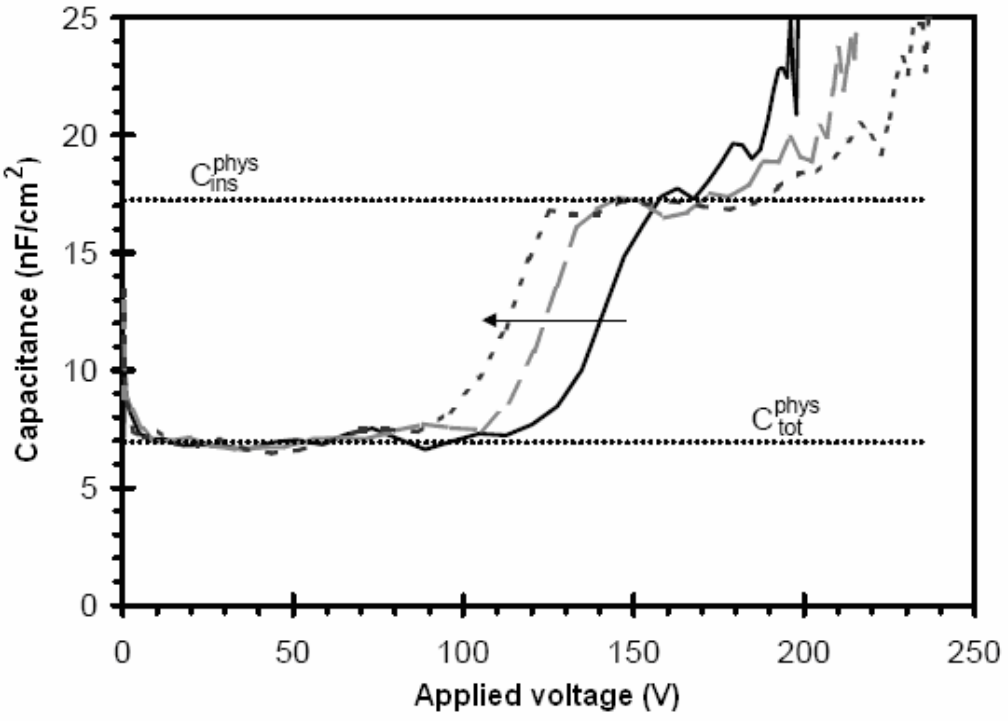

Fig.5.2: *C-V* curves for an evaporated ZnS:Mn ACTFEL device taken at 20, 40, and 60 V above threshold. The arrow indicates the direction of increasing voltage [57].

The capacitance in a *C-V* curve for the smaller voltages corresponds to the total capacitance of the ACTFEL device. Ideally, the above turn-on capacitance is equal to the insulator capacitance, C_i, of an ACTFEL device because the phosphor layer is shorted. The turn- on voltage V_{to} is apparent in a *C-V* curve as the voltage where the capacitance increases from C_t to C_i. In reality, not many ACTFEL devices have the above turn-on capacitance in a *C-V* curve, C_i^{cv}, equal to the physical insulator capacitance C_i^{phys}, assessed from film thickness and dielectric constant measurements. [57] The shape of a *C-V* curve and its dependence upon V_{max} are indicators of whether the transferred charge is interface or bulk derived. The shift of the *C-V* curves to smaller voltages with increasing V_{max} shown in Fig. 5.2 is characteristic of an ACTFEL device in which the electrons originate exclusively from interface states. If the initial portion of the *C-V* transition is soft and the *C-V* curves shift in a non-rigid manner, it is likely that a substantial portion of the transferred charge is bulk derived [53].

Two deviations from the ideal above turn-on situation exist $C_i^{cv} > C_i^{phys}$ and $C_i^{cv} < C_i^{phys}$. When $C_i^{cv} < C_i^{phys}$, there is an insufficient amount of conduction current

during the rising edge of the applied waveform to completely shunt the phosphor layer [61].

This can be attributed to an inadequate density of interface states or carrier multiplication in the phosphor bulk.

5.2.1 Internal charge-phosphor field characterization

Another method of ACTFEL characterization – internal charge-phosphor field – consists in plotting the charge against phosphor field, as it was described in paragraph 3.3.6. Internal field may substantially differ from the average external field calculated as V_{th}/t, where t is thickness of the sample. This difference is due to dynamic space charge generation in the phosphor bulk. If the steady-state fields at different maximum applied voltages above V_{th} are independent of V_{max}, then the ACTFEL device exhibits strong field limitation. The field may overshoot the steady-state value around points B and/or G due to dynamic space charge generation in the phosphor bulk [46].

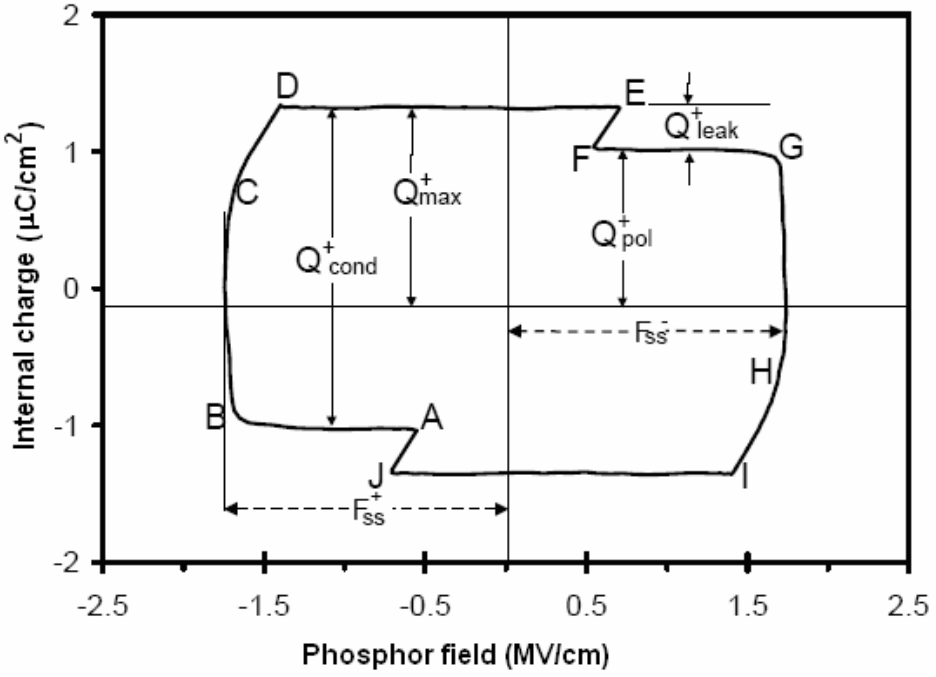

Fig.5.3: Q-F_p curve for an evaporated ZnS:Mn ACTFEL device [57].

The shape and accuracy of a Q-F_p curve depend directly upon the phosphor and insulator capacitances and the phosphor thickness, as seen in Eqs.3.9 and 3.10. An uncertainty in the phosphor thickness is reflected in an uncertainty in the phosphor field. Uncertainties in the estimates of C_i and Cp cause distortion in the shape of a Q-F_p curve [63]. Plotting a Q-F_p curve is an effective way to monitor the accuracy of the estimated values of C_i and C_p. Deviations from the estimated values and the values of C_i and C_p

that give the most ideal shaped Q-F_p curve are a result of dynamic space charge in the ACTFEL device under study. [57]

5.3 Influence of charged centers on transport characteristics

Luminescent charged centers exist in the phosphor layer of common alternating current thin film electroluminescent devices. When the electrons pass through the phosphor layer, the scattering process occurs. Scattering generally means a physical process in which particles are deflected hazardously as a result of collisions. In this paragraph, the electron scattering process by these centers is studied through phase shift analysis. Charged centers influence the transport process by changing the direction of electron motion through the scattering process. Moreover, it is necessary to use quantum mechanic description with the wave function. In the following section, this influence is investigated by means of the Monte Carlo method. The scattering rates in different cases are gained and compared with other important scattering processes.

5.3.1 Scattering rates of charged centers

5.3.1.1 Phase shift analysis of scattering process

In practice, the concentration of charged centers is not too high in ACTFEL devices. So, we ignore the interaction between charged centers, that is, adopt an isolated center model. A charged center will introduce extra Coulomb field into the lattice. This field will be screened by electrons. The final result of the potential field could be described as follows:

$$V(r)=\frac{Ze}{4\pi\varepsilon r}\exp(-r/L)\,, \tag{5.1}$$

L stands for the effective radius of the field, which describes the strength of the screening effect. Z is the effective valence of the center (the difference between the valence of this center and that of the normal ion).

The scattering process of such a potential field could be treated through phase-shift analysis [19]. The incident wave could be expanded using the eigenstate of l^2. The amplitude process since this process could be regarded as an elastic of each partial wave is unchanged during the scattering process. The only effect of the charged center is the phase shift of these partial waves. We use δ_l to represent the phase shift of the l-th partial wave, then the scattering rate is given by

$$S=\frac{4\pi\hbar}{m^*k}N\sum_{l=0}^{\infty}(l+1)\sin^2(\delta_l-\delta_{l+1})\,, \tag{5.2}$$

in which N stands for the concentration of charged centers.

In EL phosphors,

$$\frac{m^*}{\hbar^2}|V_0|r_0^2\sim10^{-4}<<1\,, \tag{5.3}$$

(V_0 and r_0 stand for the strength and range of the potential field respectively). So, the Born approximation could be different concentrations used, in which the effective radius of the field is

$$L=\left[e^2(4\pi^{3/2}\varepsilon)^{-1}\left(\frac{2m^*}{\hbar^2}\right)^{3/2}(k_BT)^{1/2}\frac{1}{\Gamma(1/2)}\int_0^{\infty}\frac{x^{-1/2}dx}{1+\exp(x-E_F/k_BT)}\right]^{-1/2}, \quad (5.4)$$

and the lth phase-shift

$$\delta_l=\frac{2m^*ke}{\hbar^2}\int_0^{\infty} j_l^2(kr)V(r)r^2dr, \quad (5.5)$$

where j_l is the lth spherical Bessel function. Substituting (5.5) into (5.4), the scattering rate of charged centers could be calculated.

5.3.1.2 Scattering rates

Based on the above discussion, scattering rates of charged centers in several cases are calculated.

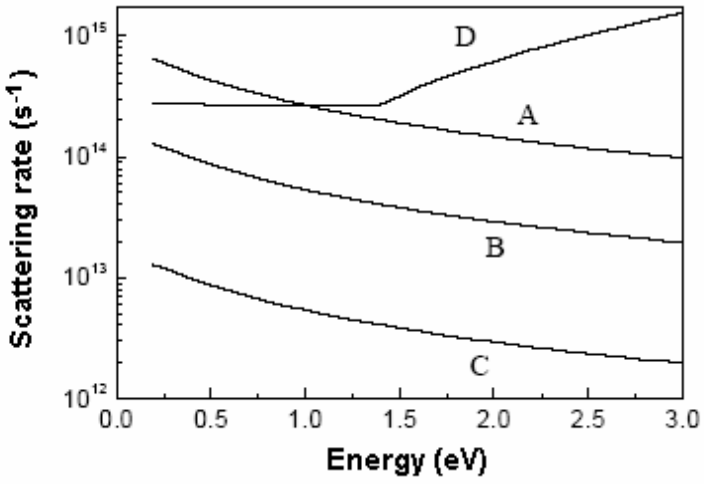

Fig 5.4: Scattering rates of charged centers (Z = 2) with field respectively). (A: 5 at. %; B: 1 at.%; C: 0.1 at.%; D: the sum of other scattering rates, T = 300 K).

Figure 5.4 shows the scattering rates under different concentrations of charged centers of Z = 2. The sum of phonon scattering rates, including acoustic phonons, polar optical phonons and intervalley scattering, is also shown in this figure for comparison [19]. According to Fig.5.4, scattering rate decreases with electron energy. Thus, it is more important in the low energy region. Comparing with other scattering mechanisms, charged centre scattering is weaker at the concentration of 0.1 atomic%. When the concentration is 1%, it is comparable with the sum of all others and will play an important role in the EL process. Furthermore, as shown in Fig.5.4, it becomes the most important scattering mechanism when the concentration reaches 5%. In this case, the total scattering rate will be doubled.

According to the calculation, in the case of T = 300 K, the effective radius of the charged center's potential is 6.25×10^{-10} m. At the concentration of 5 atomic% (which is the maximal charged center's concentration here), the interaction between charged centers is only 0.6% of V_0. This proves the validity of the adoption of the isolated center model.

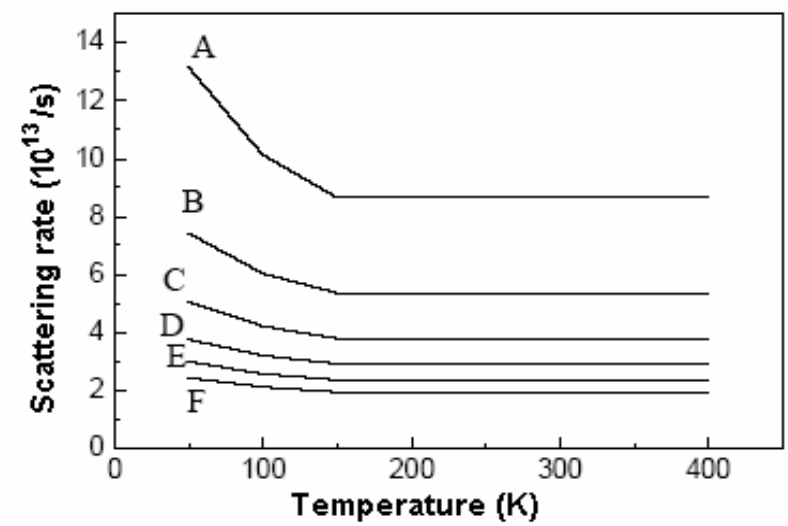

Fig. 5.5: Temperature dependency of charged centers (Z = 2) scattering rates with different electron energies (A: 0.5 eV; B: 1.0 eV; C: 1.5 eV; D: 2.0 eV; E: 2.5 eV; F: 3.0 eV).

The charged center scattering process also depends on temperature. This is introduced into our theoretical analysis by the variation of effective potential radius, L, with temperature. The calculated results are shown in Fig.5.5. In contrast with phonon scattering, the charged center scattering rate decreases with the temperature. This decrease is more obvious at low temperature. According to Fig.5.5, the temperature effect is more obvious at low electron energy. As a summary, the temperature effect of the charged center scattering is smaller than that of phonon scattering mechanisms.

In the above calculations, we set Z = 2. This is mainly the case of a vacancy. In the case of rare earth ions (luminous centers), Z = 1. Figure 5.6 shows the influence of effective valence on scattering rate. The rate of Z = 2 is about two to three times that of Z = 1 and the difference decreases with electron energy.

We have discussed charged center scattering process and calculated the scattering rates in different conditions. In fact, we treated this scattering process as an elastic process. That is, the electron does not lose energy during the scattering process. Charged centers influence the transport process by changing the direction of electron motion through the scattering process. In the following section, this influence is investigated by means of the Monte Carlo method.

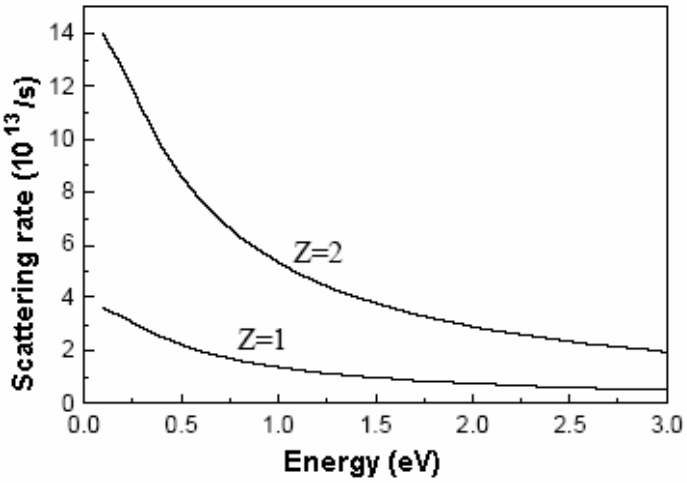

Fig.5.6: The comparison of scattering rates of charged centers with different effective valence.

5.3.2 Influence of charged centers on the transport process

5.3.2.1 Monte Carlo simulation

The Monte Carlo method is a simulation of the motion of individual carriers as they move under the influence of external fields and are scattered by various mechanisms [19]. This motion is composed by a series of 'free flight' processes terminated by the scattering events. During the 'free flight' process, the influence of scattering mechanisms is not considered and the motion could be described as

$$\frac{d}{dx}(\hbar\vec{k}) = -e\vec{E}\,, \tag{5.6}$$

where $\hbar$ is the Planck constant, e is the electronic charge, $\vec{E}$ is the electric field strength and $\vec{k}$ is the wave vector. The free flight time between two collisions t_r is chosen stochastically according to the total scattering rate [49],

$$t_r = -\frac{1}{\Gamma}\ln(r_1), \tag{5.7}$$

where Γ is the total scattering rate (the sum of rates of all scattering mechanisms considered) and r_1 is a random number generated by the computer program and is uniformly distributed between 0 and 1. At the end of this free flight ($t = t_r$), another random number uniformly distributed between 0 and 1, r_2, is generated by the Monte Carlo program to choose a certain kind of scattering from all of the scattering mechanisms. If there are n kinds of scattering mechanism and the rate of the i-th mechanism is W_i, then the probability of the occurrence of the m-th scattering is [49]

$$W_m\left(\sum_{i=1}^{n} W_i\right)^{-1}. \tag{5.8}$$

If

$$\sum_{i=1}^{m-1} W_i \left(\sum_{i=1}^{n} W_i \right)^{-1} < r_2 \leq \sum_{i=1}^{m} W_i \left(\sum_{i=1}^{n} W_i \right)^{-1} \tag{5.9}$$

the *m*-th scattering mechanism is chosen.

Once a scattering mechanism has been chosen, the momentum and the energy of the electron are updated as determined by the specific mechanism that has been selected. Then the next 'free flight' process begins until it is again terminated by the next scattering event. This cycle is repeated many times. The motion of an electron in the phosphor layer is thus simulated.

5.3.2.2 Influence of charged centers on electron kinetic energy

Based on the calculations about charged center scattering rates, the electron transport process in an ACTFEL device is simulated. The considered scattering mechanisms include acoustic phonon scattering, polar optical phonon scattering, intervalley scattering and charged center scattering. The simulation results under different charged center conditions are shown in Fig.5.7.

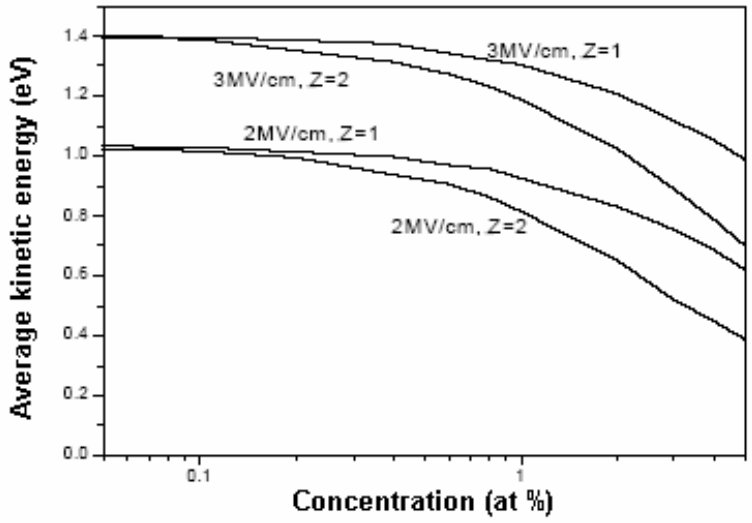

Fig.5.7: Relations between average kinetic energies and charged center concentrations.

When no charged centers exist, the average kinetic energy of electrons could reach 1.03 eV or 1.4 eV with 2.0 MV cm^{-1} or 3.0 MV cm^{-1} electric fields respectively, under room temperature. As the concentration of charged centers increases, the average kinetic energy of electron decreases. In the case of Z = 2, average kinetic energy drops to 80% or 85% under 2.0 or 3.0 $MVcm^{-1}$ electric fields respectively when the concentration is 1 atomic %.

When the concentration reaches 5 atomic %, these two figures will be 37% or 50%. On the other hand, when the concentration is lower than 0.1 atomic %, the average kinetic energy of the electrons keeps unchanged. According to Fig.5.7, the influence of charged centers with Z = 1 on electron energy is not so serious as the case of Z = 2, but it also lowers the energy significantly when the concentration reaches 1 atomic %.

5.3.3 Conclusion

Charged centers as luminescent centers exist generally in ACTFEL devices and influence their properties. At the same time, they will influence the transport process. These effects must be considered in the design of ACTFELs for novel properties. Quantitative results about the influence of charged centers on electron kinetic energy are gained.

To the authors' knowledge, this is the first investigation of the influence of charged centers on ACTFEL. These results provide basic data for further improvement of ACTFELs.

6 Aging analysis – results and discussion

6.1 Introduction

The process of burning-in and aging can be nicely monitored by regular checking of the luminance versus voltage characterization. The burn-in means to test an operation of electronic components before they are applied in order to stabilize their characteristics and reveal defects. Normally ACTFEL devices tend to stabilize after a few tens of hours of burn-in, but can exhibit complex aging behavior during the burn-in process. The luminance vs. voltage curves for ZnS:Mn devices in which the phosphor layer is deposited by evaporation, for example, tend to shift to slightly higher voltage during burn-in [50]. Aging data is collected by measuring luminance vs. voltage at selected time intervals during aging. The measurement is carried out as described earlier for luminance vs. voltage measurements (Chapter 5). The aging is done by continuously operating the device at a fixed voltage or at a fixed voltage above threshold. The aging process can be accelerated by operating the device at higher frequency or higher temperature regime. Therefore it is useful to determine the behavior of optoelectronic devices.

The aging characteristics and device stability of ACTFEL flat-panel display devices have been the subject of numerous studies [4, 62, 63]. The majority of this chapter is focused on monitoring the luminescence of the ACTFEL device as a function of aging time. Now I would like to present the results of two experiments: the purpose of this experimental work discussed herein is to report first an investigation of the aging properties of thermally evaporated as well as atomic layer epitaxy (ALE) ZnS:Mn ACTFEL device and, second to study RF sputtered green emitting Zn_2GeO_4:Mn half-stack device.

In the first case, instead of measuring the luminescent properties, we monitored the electrical properties of the ACTFEL devices as a function of aging time. Specifically, we assess the ACTFEL electrical properties using the capacitance-voltage (*C- V*) [46] and internal charge-phosphor field (Q-F_p) [53] techniques.

In the second case, the measurements of surface roughness by apertureless Scanning near-field optical microscope and of device structure by Transmission electron microscope, as well as of measurement of luminescent properties were provided.

6.2 Experimental

The ACTFEL devices consist of a ZnS:Mn active phosphor layer which is sandwiched between two sputtered silicon oxynitride insulator layers. Aluminum and indium-tin oxide (ITO) electrodes are employed as contacts. Briefly, *C-V* analysis is accomplished using the circuit shown in Fig.6.1 [50, 64]. An arbitrary waveform generator (Agilent

33220A) in conjunction with a high-voltage operational amplifier (7265 DSP) generates the small duty cycle bipolar pulse waveform which drives a series resistor, R_s the ACTFEL device, and a current sense resistor, R_c as shown in Fig.6.1. Resistance R_s is chosen to be 1.25 kΩ and R_c is chosen to be 10 Ω. Voltages $v_2(t)$ and $v_3(t)$ are obtained using a digitizing oscilloscope (Agilent 54621 A). The standard waveform consists of symmetric, bipolar pulses of trapezoidal shape with 5 μs rise and fall times and a pulse width of 30 μs where rise and fall times are defined as the time between 0% and 100% of the maximum amplitude and the pulse width is defined as the duration during which the pulse is at its maximum amplitude. The frequency of the waveform is 1 kHz.

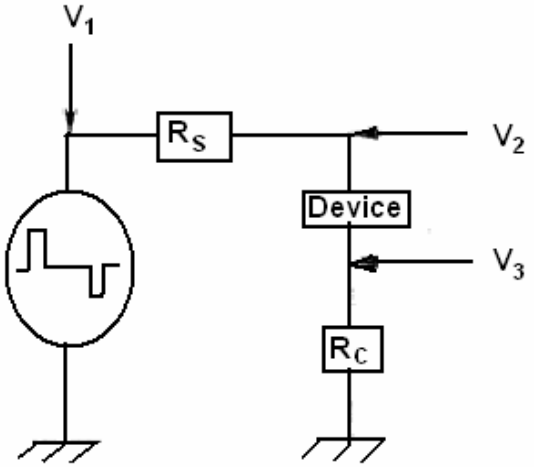

Fig.6.1: Circuit scheme used for ACTFEL electrical characterization [50, 64].

Referring to Fig.6.1, the current through the ACTFEL device is obtained from the voltage across the sense resistor, R_c, e.g. $i(t) = v_3(t)/R_c$. The capacitance is equal to the current divided by the derivative of the voltage across the ACTFEL device, so that

$$C(v_2 - v_3) = \frac{i(t)}{d[v_2(t) - v_3(t)]/\,\mathrm{d}t} \quad . \tag{6.1}$$

The *C-V* curve is obtained by plotting $C(v_2\text{-}v_3)$ vs. $[v_2(t) - v_3(t)]$ and is shown in Fig.6.2. Capacitance C_t refers to the total capacitance prior to breakdown while C_i is the insulator capacitance. Since the *C-V* transition is non-abrupt, we denote three turn-on voltages, V_{to1}, V_{to2}, V_{to3}, which refer to the onset of conduction, the midpoint of the *C-V* transition, and the field-clamping voltage, respectively. Voltage V_{to2} is found to correspond very well to the normal *Q-V* threshold.

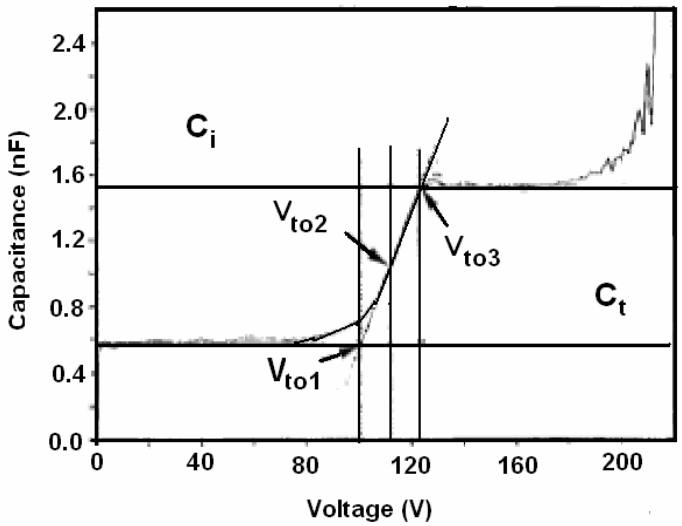

Fig.6.2: *C-V* curve for ZnS:Mn ACTFEL device.

6.3 Results and discussion

6.3.1 Thermally evaporated ZnS:Mn

The results of the first experiment with thermally evaporated ZnS:Mn ACTFEL aging experiments are summarized in Figs.6.3 to 6.5 for the following temperatures: -50°C, -10°C, 0°C, 20°C, 60°C, and 80°C [64]. The family of selected *C-V* curves shown in Fig.6.3 is for the 60°C experiment. These curves show characteristics typical of all aging experiments at various temperatures.

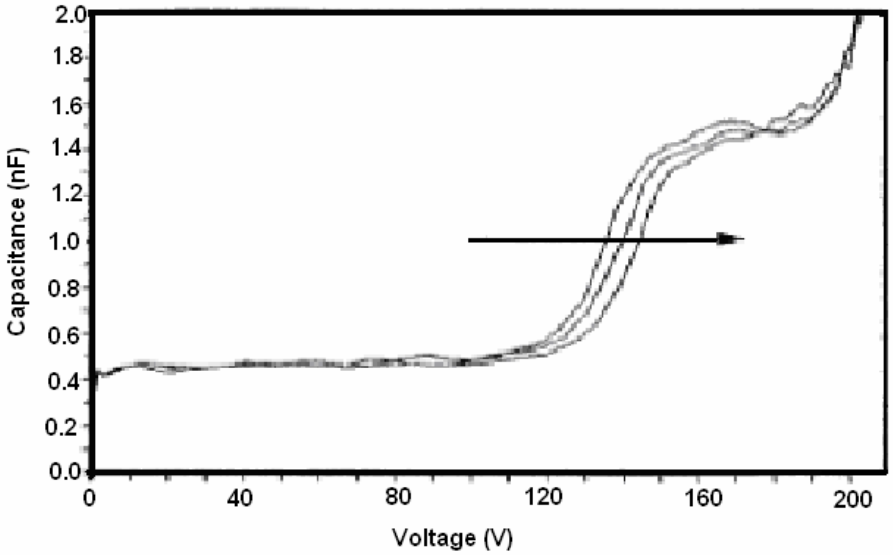

Fig.6.3: *C-V* curves for 60°C experiment. Arrow indicates direction of increasing aging time. Aging times of curves shown are 1 second, 20 minutes, and 9.5 hours (from left to right) [64].

In general, it is observed that the turn-on voltage shifts rigidly with operating time and that C_t and C_i remain constant, to within experimental error, with aging time.

As can be observed from Figs.6.4 and 6.5, the aging characteristics can be classified into four regimes:

(1) incubation period,
(2) logarithmic aging,
(3) saturation, and
(4) long-term aging.

At lower temperatures there is an incubation period, in which the turn-on voltage is essentially constant; this incubation period is most clearly evident in Fig.6.5. This incubation period lasts 1 hour at the lowest temperature (-50°C) and eventually disappears at and above room temperature (20°C).

The incubation period is followed by a period in which the turn-on voltage increases logarithmically with aging time.

Next, the turn-on voltage approaches a saturated value which is temperature-dependent. Finally, the last aging regime is denoted long-term aging in which the turn-on voltage decreases slowly with increasing aging time. The logarithmic and saturation aging regimes are taken to collectively comprise what we denote the short-term aging characteristics. The incubation period is tentatively attributed to the fact that the warm-up and pre-aging occur at a higher temperature than that of the aging.

Long-term aging kinetics will be the subject of future study. Thus, our present study of the aging kinetics will focus on short-term aging in which the kinetics are found, or extrapolated, to be logarithmic or saturated.

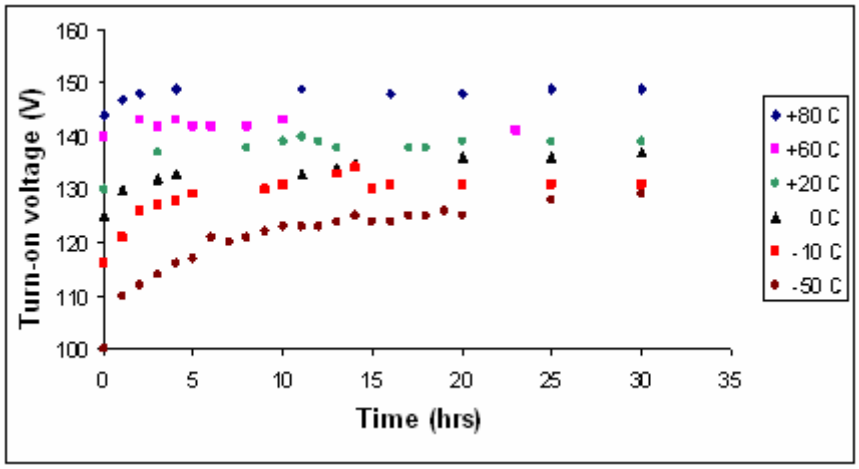

Fig.6.4: Turn-on voltage, V_{to2}, as a function of aging time at temperatures of -50, -10, 0, 20, 60, and 80°C [64].

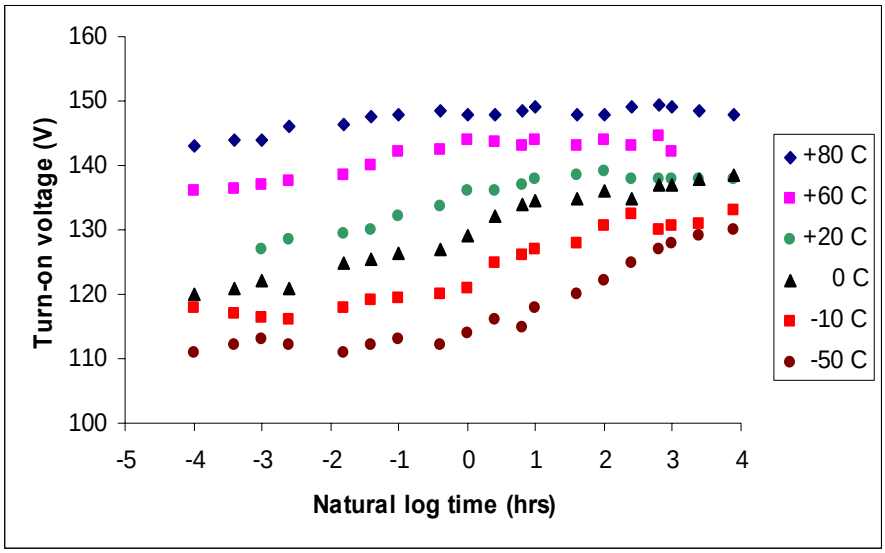

Fig.6.5: Turn-on voltage, V_{to2}, as a function of the natural logarithm of aging time at temperatures of -50, -10, 0, 20, 60, 80°C [64].

6.3.1.1 Conclusion

An ACTFEL aging study is presented in which the *C-V* technique is used to characterize the electrical properties of thermally evaporated ZnS:Mn ACTFEL devices at various temperatures as a function of aging time. The primary experimental findings of this study are the following:

1) The insulator and phosphor capacitances are constant with respect to aging time; this suggests that the perturbation in the electrostatic charge distribution which is responsible for aging occurs near the SiON/ZnS interfaces.
2) The *C-V* curve shifts rigidly with aging time; this indicates that changes in the fixed charge density, not the interface charge density, give rise to aging.
3) The activation energy for short-term aging is found to be approximately 0.2 eV. These experimental observations lead to the following model for aging of evaporated ZnS:Mn ACTFEL devices. Atomic rearrangement at SiON/ZnS interfaces leads to the formation of deep level, fixed charge states which trap transported conduction electrons. Such electron trapping leads to a reduction of the conduction and polarization charges and an increase in the turn-on voltage. It is likely that atomic migration is stimulated by the thermalization energy dissipated by hot electrons after they impinge upon the SiON conduction band discontinuity. Also, it is likely that atomic migration at the interface is exacerbated by the presence of sulfur vacancies in the ZnS near the interface.

6.3.2 Atomic layer epitaxy ZnS:Mn

In this case, ZnS:Mn layer was deposited by atomic layer epitaxy (ALE). We measured the *C-V* characteristics in two regimes with positive and negative voltage applied to the top Al electrode.

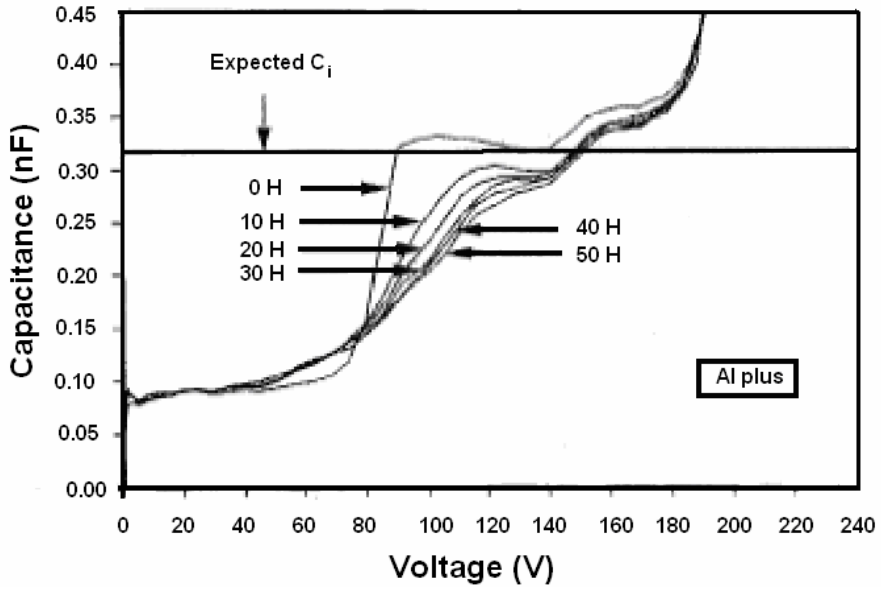

Fig.6.6: *C-V* curves as a function of aging time for ALE ZnS:Mn ACTFEL device when the Al electrode is positively biased (i.e., emission from the IT0 interface) [50].

Figure 6.6 illustrates *C-V* characteristics as a function of aging time for a positive voltage pulse applied to the top Al electrode [50]. The *C-V* curve shifts with respect to aging time, and this shift indicates that the interface state density in the restricted regime, Q_{ss} (averaged steady state charge) increases as a function of aging time. Moreover, notice how soft the *C-V* curve becomes in the v_{to1} regime as aging continues; this softening indicates that electrons are injected from shallower interface states as aging progresses. Finally, we found that the effective insulator capacitance C_i decreases with aging time, most of the decrease in C_i occurs during the initial 10 hours of aging.

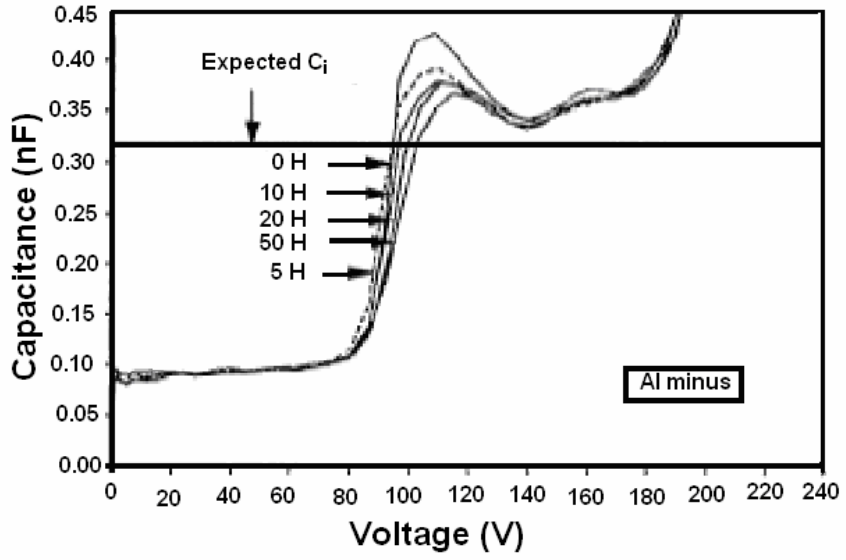

Fig.6.7: *C-V* curve as a function of aging time for an ALE ZnS:Mn ACTFEL device when the Al electrode is negatively biased (i.e., emission from the Al interface) [50].

On the other side, figure 6.7 shows *C-V* curves corresponding to various aging times for a negative voltage pulse applied to the top Al electrode.

It is evident, from a comparison of Fig.6.6 and Fig.6.7, that the *C-V* curves corresponding to the two interfaces are quite different initially and that they display distinctly different aging trends. Hence, the electrical properties and aging characteristics of these interfaces are also quite different. The asymmetry trends we observe by *C-V* analysis are similar to the conduction current-voltage curves reported by Soenen et al [62]. Perhaps the most unusual aspect of the curves shown in Fig.6.7 is the *C-V* overshoot which we interpret as evidence for the buildup of space charge in the bulk ZnS phosphor. An overshoot in the Q-F_p characteristics is also observed concomitant with *C-V* overshoot; this is further evidence for space charge. Notice that the extent of the overshoot decreases with increasing aging time. Therefore, the amount of space charge which builds up in the ZnS decreases with aging. The second trend, evident from Fig.6.7, is that the *C-V* curve first shifts to lower voltages and then shifts to higher voltages with increasing aging time. These shifts are interpreted as indicating that Q_{ss} is rather constant with aging. Furthermore, since these *C-V* curves are rather steep, averaged steady state charge Q_{ss} is relatively small.

Several of the *C-V* trends discussed previously are summarized in Fig.6.8. and Fig.6.9. Figure 6.8 is a plot of the turn-on voltage V_{to2}, as a function of aging time. Voltage V_{to2} for the bottom interface monotonously increases with aging time as the *C-V* transition becomes broader. Voltage V_{to2} for the top interface first decreases slightly, then increases slowly, and finally saturates at a voltage similar to its original value. Figure 6.9 indicates the dramatic difference in the Q_{ss} aging trends for the two interfaces. Both interfaces exhibit an increase in Q_{ss} with aging time, but the change in the bottom interface is much larger.

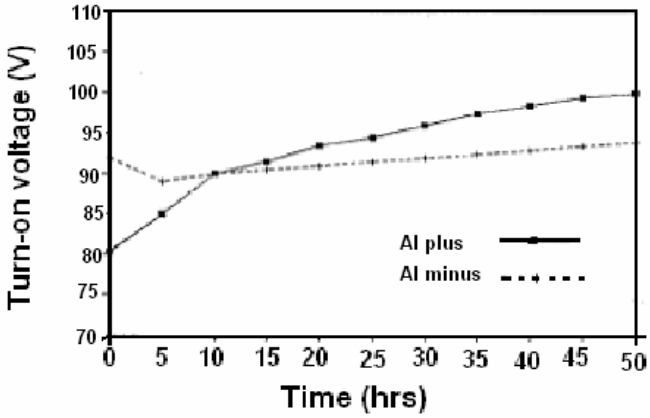

Fig.6.8: Turn-on voltage V_{to2} vs aging time for an ALE ZnS:Mn ACTFEL device [50].

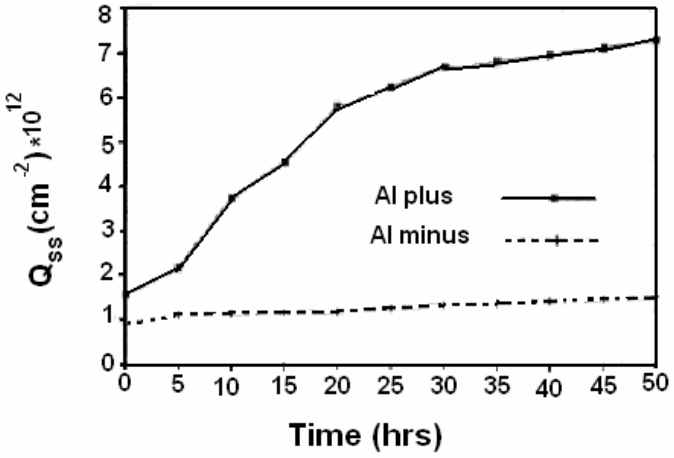

Fig.6.9: Averaged steady state charge Q_{ss} vs. aging time for an ALE ZnS:Mn ACTFEL device [50].

6.3.2.1 Conclusion

In this paragraph an experimental study of the aging characteristics of ALE ZnS:Mn ACTFEL devices is presented in which aging is assessed by monitoring the electrical properties of these devices via *C-V* and *Q-F* analysis. The electrical properties of these ALE devices are asymmetrical with respect to the polarity of the applied voltage pulse. This is in contrast to thermally evaporated ZnS:Mn ACTFEL devices whose electrical and optical properties are quite symmetric. This asymmetry is in good agreement, however, with the results of previous workers. We attribute the experimentally observed asymmetry of the electrical properties to differences in the interface state densities of the top and bottom interfaces.

The most striking implication of the aging trends is that the interface state distributions at the top and bottom interfaces are asymmetric and, furthermore, exhibit highly asymmetric aging characteristics. This is clearly illustrated by the Q_{ss} aging trends shown in Fig.6.9. In summary, our assessment of the experimental data shown in Figs. 6.6 - 6.9 leads to the following conclusions regarding the aging characteristics of-ALE ZnS:Mn ACTFEL devices:

1) The interface state densities of the top and bottom interface are distinctly different and exhibit different aging characteristics.
2) Both shallow and deep traps are created during aging at the bottom interface.
3) A smaller number of predominately deep traps are created at the top interface during aging.
4) The decrease in C_i with aging indicates that some of the "interface steady state charge" actually moves deeper into the ZnS bulk with aging.
5) The decrease in the *C-V* overshoot of the bottom interface indicates that the amount of space charge build up in the ZnS decreases with aging time.

6.3.3 Subthreshold voltage-induced transferred charge

Another useful and interesting technique for investigation of subtle device physics electrical operation and the aging behavior of ACTFEL devices (ZnS:Mn phosphor layer) is subthreshold voltage-induced transferred charge (VIQ) method [46]. The VIQ set-up is shown in Fig.3.2.

The VIQ experiment consists of applying a large number of bipolar trapeziodal voltage pulses of a variable subthreshold voltage amplitude and monitoring the polarity and magnitude of the voltage induced across a sense capacitor during illumination of the ACTFEL device with a xenon lamp to optically reset the voltage-induced space charge within the ACTFEL device; this induced voltage across the sense capacitor during the optical reset is the VIQ signal.

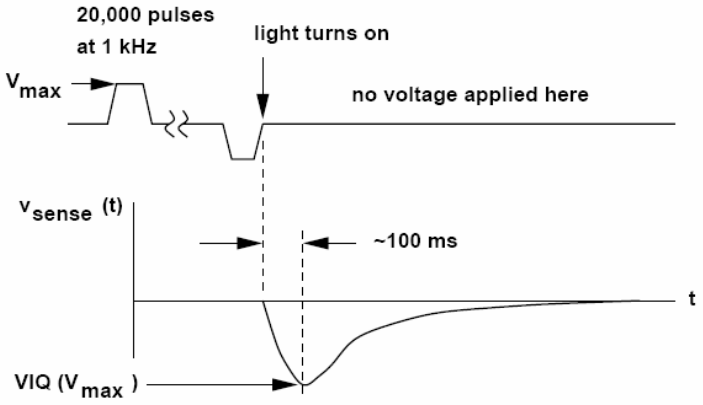

Fig.6.10: Timing diagram for subtreshold voltage-induced transferred charge (VIQ) experiment [46].

The time sequence of events in the VIQ experiment is called “timing diagram” and is shown in Fig.6.10 and illustrates the origin of the VIQ signal. A VIQ curve is obtained by plotting the VIQ signal versus the applied voltage amplitude from 0 V up to threshold. Such VIQ plots typically consist of one or more gaussian-shaped peaks. The voltage location, height, polarity, and temperature dependence of a VIQ peak provides information about the physical location, energy depth, capture cross-section, and density of phosphor traps giving rise to the VIQ signal. Moreover, changes in the VIQ signal as a function of aging time provide information related to the physical nature of ACTFEL aging.

The essence of VIQ experiment may be discerned with the aid of Fig.6.11 and Fig.6.12, which show two possible VIQ energy band diagrams during the optical reset portion of the experimental sequence when the VIQ signal is monitored as the maximum transient voltage developed across the sense capacitor. The VIQ space charge distribution in Fig.6.12 shows negative charge near the bottom (ITO) [top (Al)] interface and positive (negative) charge near the top (Al) [bottom (ITO)] interface. The VIQ polarity is established by the direction of flow of the photo-generated carriers.

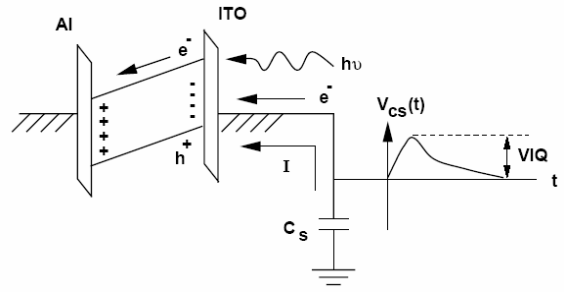

Fig.6.11: VIQ energy band diagram - negative charge trapped near the bottom phosphor/insulator interface [46].

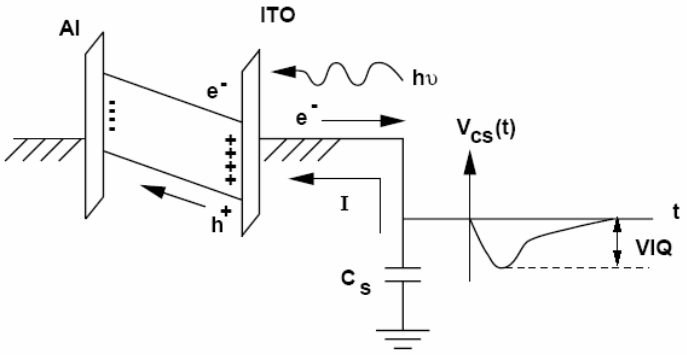

Fig.6.12: VIQ energy band diagram - positive charge trapped near the bottom phosphor/insulator interface [46].

6.3.3.1 Results and discussion

The ZnS:Mn VIQ aging experiments were performed using samples with phosphors deposited by three different methods: thermal evaporation, atomic layer epitaxy using chlorine ALE (Cl), and atomic layer epitaxy using diethylzinc ALE (DEZ). The method of deposition turned out to have strong effect on the aging characteristics of the ACTFEL device.

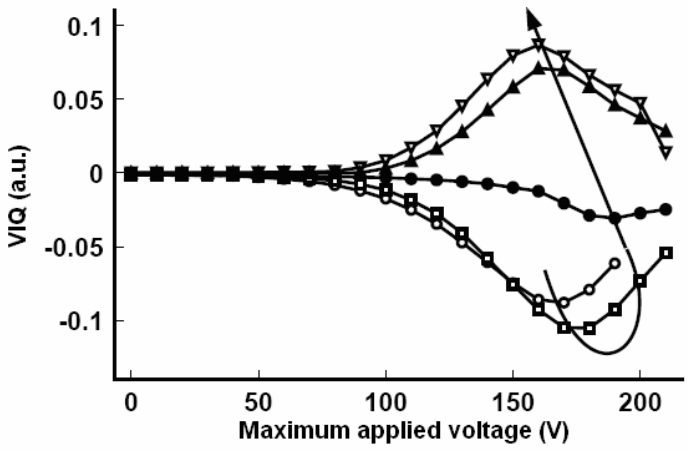

Fig.6.13: VIQ aging trend for an thermally evaporated ZnS:Mn ACTFEL device [46].

The VIQ aging curves for a thermally evaporated ZnS:Mn ACTFEL device are shown in Fig.6.13. A negative polarity VIQ peak occurs for the first few hours of operation; this corresponds to a situation in which the most shallow VIQ traps are located near the bottom (ITO) interface; this gives rise to positive charge near the bottom interface, as shown in Fig.6.12. The negative VIQ peak initially increases in magnitude and then decreases in magnitude as a function of aging, with the location of the voltage peak increasing slightly. After ~40 hours of aging at 1 kHz, the VIQ polarity switches from negative to positive.

A positive VIQ peak is attributed to localization of the most shallow VIQ traps near the top (Al) interface, giving rise to positive charge near the top (Al) interface, as shown in Fig.6.11.

The voltage at which the VIQ peaks gradually decreases for aging periods longer than 40 hours. The VIQ response exhibits a VIQ threshold voltage of ~90V, corresponding to a VIQ threshold field of ~0.7 MV/cm, which remains constant with aging. The fact that the VIQ threshold field does not change with aging suggests that the VIQ traps at the top and bottom interface arise from the same type of trap. The decrease and subsequent switch of polarity with aging is attributed to changes in the trap density at or near the interfaces. The increase in the VIQ peak magnitude for initial aging is attributed to the generation of more traps near the bottom (ITO) interface. Later aging causes generation of traps near the top (Al) interface, resulting in a reduction of the VIQ maximum, and finally leading to a switch in the VIQ polarity. Luminance-voltage (*L-V*) and capacitance-voltage (*C-V*) measurements of evaporated ZnS:Mn ACTFEL devices exhibit p-shift followed by n-shift aging characteristics. These *L-V* and *C-V* p-shift to n-shift aging trends correlate well with VIQ measurements in which the negative polarity VIQ signal switches to a positive polarity VIQ signal for longer aging periods. Thus, these *L-V, C-V*, and VIQ aging trends arise from a common source [11].

Voltage induced charge (VIQ) aging curves for an ALE (Cl) ZnS:Mn ACTFEL device are shown in Fig.6.14.

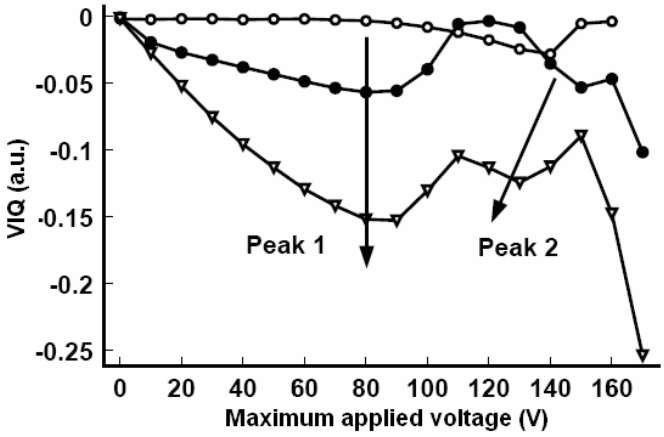

Fig.6.14: VIQ aging trend for an ALE (Cl) ZnS:Mn ACTFEL device [46].

The new samples prepared by ALE (Cl) have a single small negative VIQ peak and develop two large negative peaks with aging. A negative polarity VIQ signal is consistent with the energy band diagram shown in Fig.6.12, in which the most shallow

VIQ trap states are present near the bottom (ITO) interface. The lower voltage peak, Peak 1, grows with aging and remains at the same voltage. The trap responsible for Peak 1 must be very shallow since the VIQ threshold voltage occurs at approximately 0 V. The higher voltage peak, Peak 2, grows and shifts to a lower voltage with aging. Peak 2 is attributed to a deeper trap. The VIQ aging does not tend to stabilize, although the rate of growth of both VIQ peaks slows down after the ACTFEL device has been aged for a long time.

VIQ aging curves for an ALE (DEZ) ZnS:Mn ACTFEL device are shown in Fig. 6.15. A single VIQ peak is observed which initially increases and then decreases in magnitude. The VIQ peak voltage decreases with aging. The initial increase in the VIQ magnitude is likely due to an increase in the number of traps responsible for VIQ near the top (Al) interface. The subsequent decrease in VIQ magnitude and concomitant shift in the peak to a lower voltage after 4 hours of aging is possibly due to generation of traps at the bottom (ITO) interface.

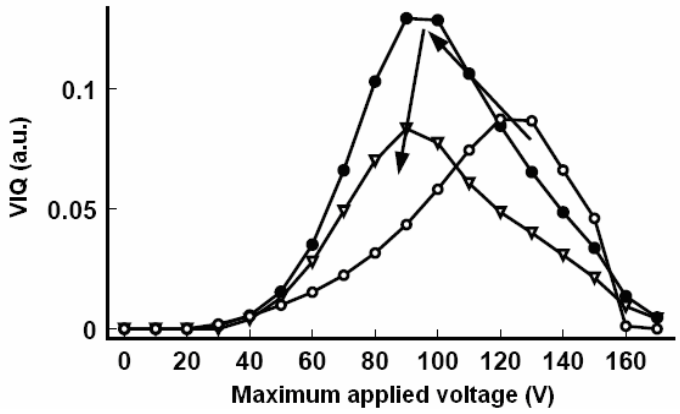

Fig.6.15: VIQ aging trend for an ALE (DEZ) ZnS:Mn ACTFEL device [46].

6.3.3.2 Conclusion

The trap depth and capture cross-section of a VIQ trap may be estimated from temperature-dependent VIQ analysis, and may also provide clues regarding the atomic identification of VIQ traps. Traps with a capture cross-section greater than ~10^{-14} cm^2 are coulombically attractive, traps with a capture cross-section of ~10^{-14}-10^{-18} cm^2 are neutral, and traps with a capture cross-section less than ~10^{-18} cm^2 are coulombically repulsive. Thus, the capture cross-section of the evaporated ZnS:Mn VIQ trap indicates this trap to be attractive or neutral, and the ALE (DEZ) VIQ trap to be neutral. A likely candidate for the evaporated ZnS:Mn VIQ trap would be a sulfur vacancy, which is a double donor that would be coulombically attractive to electron capture. Also, the first and second ionization energies of a sulfur vacancy in ZnS have been estimated as ~1.2 and ~1.4 eV, in reasonable agreement with the VIQ trap energy depth estimation. A possible ALE (DEZ) VIQ trap would be oxygen on a sulfur site, which is an isoelectronic trap, and would hence be neutral for electron capture. Finally, the energy depth of Cl in ZnS is ~0.2-0.3 eV, suggesting that VIQ Peak 1 in the ALE (Cl) ZnS: Mn ACTFEL device is due to Cl.

6.3.4 Green-emitting Zn_2GeO_4:Mn

Oxides were among the first and more extensively researched luminescent materials, and they comprise a substantial portion of important phosphors for electroluminescent lamp, cathode ray tube (CRT), and other applications [22]. Oxide phosphors are attractive because of their enormous number, large game of emission colors, and thermodynamic stability. Additionally, many historically important luminescent oxides, such as willemite (zinc silicate) and ruby (Al_2O_3:Cr), are naturally-occurring, and the manufacture of oxides is often relatively simple and safe. Previous research on alternating-current thin-film electroluminescence (ACTFEL) [6], however, has generally been focused on sulfide-based phosphor systems, particularly ZnS and SrS. Oxide phosphor materials have been thought to be poorly suited for ACTFEL applications because of their typically large bandgaps and their refractory nature. The last decade, however, has seen an increase in oxide thin-film phosphor research with several groups reporting success in manufacturing oxide-based ACTFEL devices [10].

ACTFEL devices are made by using the standard non-inverted structure on glass [65]. In this chapter, we extend this previous work by assessing temperature and aging characteristics of Zn_2GeO_4:Mn ACTFEL devices. Surface roughness of the layer can significantly affect the brightness of the device by affecting its output efficiency.

6.3.4.1 Experimental

The ACTFEL device half-stack structure used in this experiment is one insulator device similar to that shown in Fig.2.2 (Chapter 2) consisting of a 200 nm thick layer of indium tin oxide (ITO) as the (transparent) bottom electrode, a 200 nm thick aluminum titanium oxide (ATO) bottom insulator layer, the Zn_2GeO_4:Mn phosphor, and a 150 nm thick top contact of Al. The phosphor layer is composed of a thin film deposited by RF magnetron sputtering of a $Zn_{2x}GeO_4$:Mn_x target, where x = 0, 0.005, 0.01, 0.02, 0.04, or 0.06, i.e., undoped and 0.25-3 atomic %Mn relative to Zn sites [66].

Unfortunately, sputtered films have a lot of point defects. Point defects alter the phosphor field and are responsible for increased inelastic scattering which negatively affects the number of electrons which become sufficiently hot and cause luminescence. This in turn negatively affects the excitation efficiency. Point defects also create non-radiative recombination pathways which are in direct competition with radiative pathways and therefore reduce the radiative efficiency [finally trap charge and bend electric field]. Hence it is important to minimize the number of point defects to achieve good luminescence. Annealing helps remove defects and also improves dopant activation.

In this chapter the Mn concentration always refers to the atomic concentration in the target; the Mn concentration incorporated into the thin film phosphor may differ from that of the target concentration. These targets were prepared at the Faculty of Nuclear science and Physical engineering at Prague from stoichiometric quantities of ZnO, GeO_2, and MnO powders that were reacted in air to form the germanate, cold-pressed into two-inch targets, and sintered in air at 1100°C for several hours to achieve densification. The thin-film stack was annealed in air, typically for ~2 hours at ~680°C; films with bright photoluminescent emission were found to result from annealing at temperatures as low as 620°C.

6.3.4.2 Results and discussion

6.3.4.2.1 Surface roughness and structure

Surface roughness can significantly affect the brightness of the device by affecting the output or outcoupling efficiency. As-deposited films and films annealed at 425ºC for 1 hour films were quantitatively analyzed to study changes in surface roughness. Figure 6.16 shows surface morphology from apertureless Scanning near-field optical microscopy for (a) as-deposited and (b) annealed Zn_2GeO_4:Mn samples. The root mean square (RMS) surface roughness measured was 16 - 16.5 nm for the as-deposited films and 15 - 15.5nm for the annealed films. Negligible change (±10%) in the surface roughness was observed between the two, suggesting that the outcoupling efficiency of EL emission was not changed by annealing.

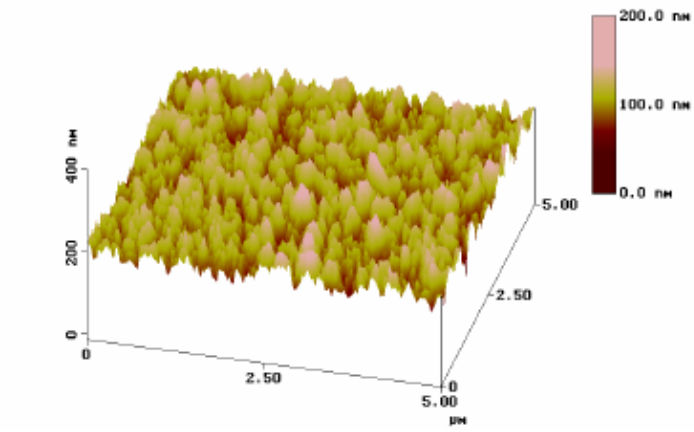

(a)

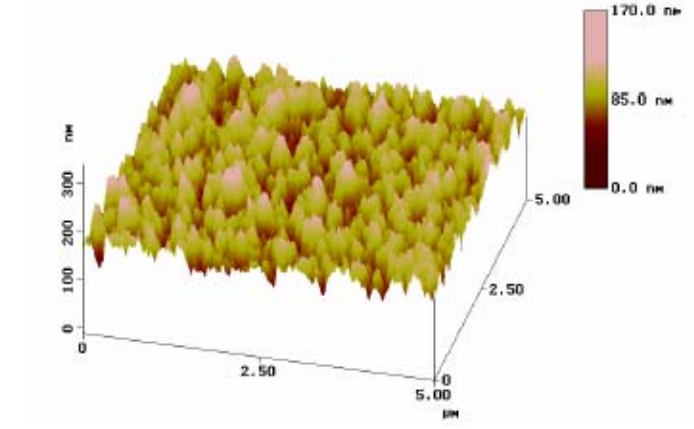

(b)

Fig.6.16: Apertureless SNOM surface morphologies of
(a) as-deposited and (b) annealed at 425 ºC for 1 hr Zn_2GeO_4:Mn thin films [66].

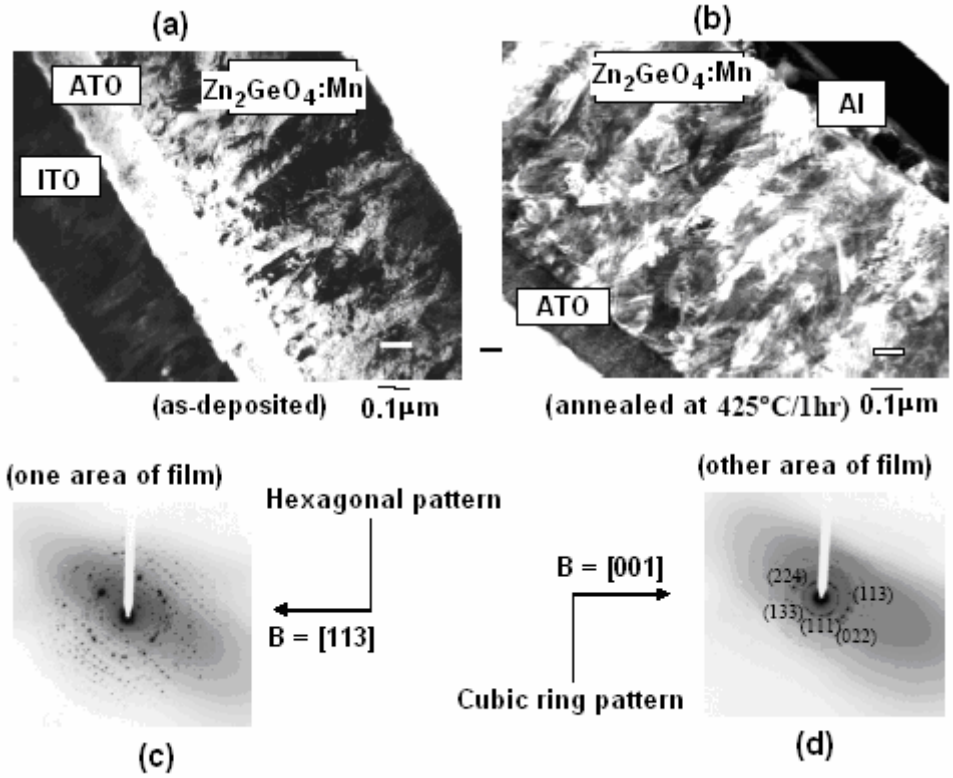

Fig.6.17: TEM micrographs for Zn_2GeO_4:Mn thin films [66].

To resolve the cubic and hexagonal phases, TEM was used to investigate the structure of the Zn_2GeO_4:Mn thin films on a microscopic scale. A JOEL 200 CX TEM operating at 300 keV was used for the characterization and determination of cross section of samples. Figure 6.17 shows cross section TEM micrographs for Zn_2GeO_4:Mn thin films in the as deposited (Fig.6.17a) and the annealed conditions (Fig.6.17b). This figure clearly shows the multi-stacked ACTFEL structure. To study the structure of the thin film device, electron diffraction patterns were collected from various parts of the Zn_2GeO_4:Mn film. TEM revealed a mixture of two structures (cubic and hexagonal) though it was difficult to resolve one from the other. In one area of the film a predominantly cubic structure (Fig.6.17d) was observed whereas in other areas it was predominantly hexagonal (Fig.6.17c). On the whole a rather non- homogenous film was observed.

6.3.4.2.2 Optical characterization

One of the more important attributes of an ACTFEL phosphor material is its luminance stability. The luminance-voltage (*L-V*) and luminous efficiency-voltage (η-*V*) characteristics of a Zn_2GeO_4:Mn (2% Mn) ACTFEL device operated at 50 Hz are shown in Fig.6.18. $L_{40} = 10^5$ cd/m^2 and $\eta_{40} = 0.33$ lm/W are observed for the brightest device; other devices exhibit lower luminance levels (L_{40} = 80cd/m^2) but better efficiency ($\eta_{40} = 0.45$ lm/W). These numbers can be compared to the brightest reported saturated green ACTFEL phosphors, ZnS:Tb and ZnS:TbOF, which have 50 Hz L_{40} = (90 – 100) cd/m^2 and η_{40} = (0.6 - 1.0) lm/W, respectively, and CIE coordinates of

0.30; 0.60. These ZnS:Tb EL phosphors, however, have been hindered by stability problems; four prominent emission peaks also limit color purity. Also, the use of $BaTa_2O_6$ as a top insulator material would double the insulator capacitance and therefore is expected to double the L_{40} value for the Zn_2GeO_4:Mn devices to $\eta = 200$ cd/m^2 [57].

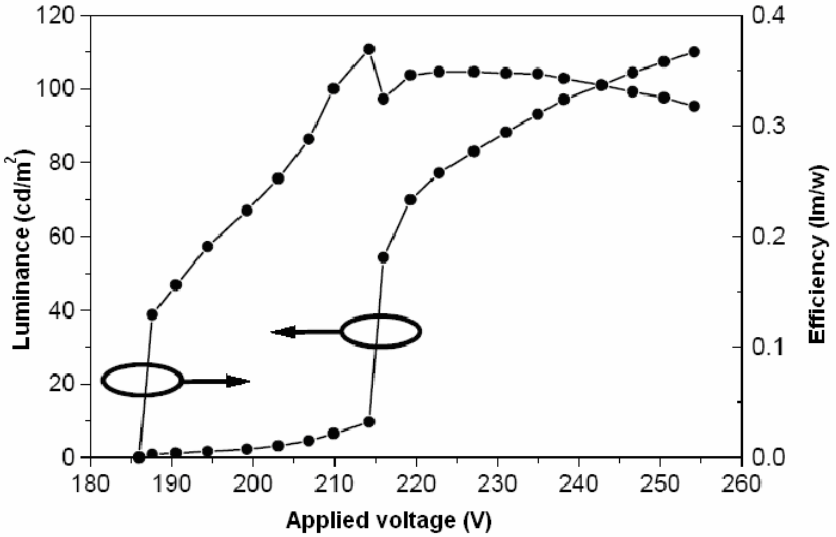

Fig.6.18: Luminance-voltage (*L-V*) and efficiency-voltage (η-*V*) plots of a Zn_2GeO_4:Mn (2% Mn) ACTFEL device driven at 50 Hz. ($L_{40} = 10^5$ cd/m^2 and $\eta_{40} = 0.33$ lm/W) [57].

The sharp step in the L-V curve shown in Fig.6.18 is the result of space charge in the device. Devices with low Mn concentrations tend to show exponential luminance increases with voltage until 40 V over threshold, at which point the luminance essentially saturates. This exponential luminance increase is also seen in devices with higher Mn concentrations, as well as in most sulfide devices, for a much shorter span of several volts, before the step in luminance noted above.

Additionally, some devices exhibit L-V curves that are basically step functions, with the luminance increasing from zero to on the order of a hundred cd/m^2 over the space of a few volts, then saturating at that level. This behavior is accompanied by an extremely large amount of space charge generation, resulting in very high phosphor current densities that can reach instantaneous values well over 1 A/cm^2. This behavior seems to be related to the "domain EL". These devices tend to be very unstable, usually burning out quickly, presumably as a result of the large current densities observed.

6.3.4.3.3 Aging trends

Previous research indicated that Zn_2GeO_4 ACTFEL devices age very rapidly, essentially to zero luminance in a very short time [67]. The aging mechanism hypothesized involved rapid atomic diffusion through large, open 1-D tunnels present in the zinc germanate crystal structure.

Constant voltage aging behavior typical of the devices manufactured during this study with the standard structure is indicated by curve (a) in Fig.6.19, which shows the

normalized luminance of a 3% doped Mn Zn_2GeO_4:Mn device operated at 40 V above the initial threshold voltage at 1 kHz as a function of time [64].

The luminance declines from 168 cd/m^2 to 62 cd/m^2 after 24 hours, while the threshold voltage is found to have shifted from 190 V initially to 212 V.

The luminance at 40 V over the post-aging threshold of 212 V is 136 cd/m^2, indicating that most but not all of the luminance decrease is the result of the positive threshold voltage shift (i.e. p-shift aging). This type of p-shift aging is not perceived to be problematic since it may be accommodated via an initial 'burn-in' procedure.

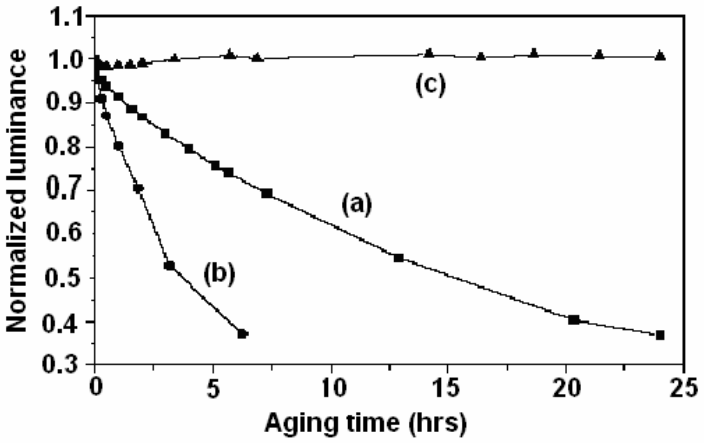

Fig.6.19: Normalized luminance vs. aging time for three devices on two substrates, as described in the text. Devices (a) and (c) are aged at 300 K, while (b) is aged at 125 K [66].

To investigate the cause of the aging, a device adjacent to the device in curve (a) on the same substrate (which should be as nearly identical as possible) is aged at a reduced temperature of 125 K. At such low temperatures, processes that are strongly dependent upon thermal energy, including atomic diffusion, should be severely retarded, while the electron distribution should be significantly hotter since less lattice scattering of the carriers occurs. A hotter electron distribution could lead to accelerated aging as hot electrons break chemical bonds within the phosphor layer, or as they thermalize and recombine at the conduction band discontinuity between the phosphor and the insulator. (Thermalization is the process of particles reaching thermal equilibrium through mutual interaction. For example, when a molecule absorbs energy, the lifetime of exited state is ~ 10^{-12} s. Then it rapidly loses energy to the lowest level of the lowest excited state.)

The low-temperature aging trend of a Zn_2GeO_4:Mn device is shown as curve (b) in Fig.6.19 [66]. The initial 125 K luminance of 626 cd/m^2 is reduced to 232 cd/m^2 after only a little more than six hours, a degradation rate much faster than at high temperature; the luminance at 300 K was measured before and after aging and decreased similarly. Thus, it appears that hot electrons are responsible for some of the Zn_2GeO_4:Mn ACTFEL device performance degradation. This is in contrast to temperature-dependent aging experiments using evaporated ZnS:Mn ACTFEL devices, which showed more degradation after 15 min of aging at 300 K than occurred after 24 hours of aging at 125 K. Finally, curve (c) of Fig.6.19 corresponds to a device with a structure somewhat different from the other devices. The 300 nm thick bottom insulator of Y_2O_3 and the 1000 nm thick phosphor layer were deposited on ITO-coated glass and

subjected to a 680°C furnace anneal in Ar/O_2. A 200 nm thick top insulator layer of SiON and Al contacts were deposited after a 650°C RTA in O_2. The device in curve (c) is aged at 50 V over threshold at 1 kHz and 300 K, and the initial luminance of 145 cd/m^2 is maintained over 24 hours of aging. This performance stability was verified for other devices on the same substrate.

In investigating the electro-optical characteristics of the device in curve (c), several atypical features stand out. First, when ramping up the applied voltage, only a small amount of negative transient offset of the electrical characteristics [57] is witnessed near threshold, whereas other devices usually display a large amount. This transient offset is thought to be due to a mismatch in the energy depths of traps responsible for sourcing transferred charge, with a negative offset corresponding to shallower top interface traps. The significant reduction seen in device (c) of this offset implies that the trap energies are more closely matched than in other devices. Second, luminescence is first observed roughly simultaneously for both applied voltage polarities, rather than the usual case in which the negative emission precedes the positive emission by several volts.

Third, the nature of the emission itself is odd in that transient luminance annihilation is observed for both polarities at 1 kHz, rather than only for the positive pulse. Both polarities also exhibit strong trailing edge emission, so that the instantaneous luminance level at the end of either pulse is not diminished from the instantaneous luminance level at the beginning. Fourth, the phosphor field is more symmetric with respect to the voltage pulse polarity compared to other devices. Overall, the electro-optic behaviour of these very stable devices is much more symmetric, especially near threshold, than the behaviour normally observed in other devices.

However, the dependence Q_{max}-V_{max} trends of the very stable devices are found to be much more asymmetric than other devices. Specifically, the threshold step in the Q_{max}-V_{max} curves is found to be much larger and steeper for the negative applied voltage pulse; the derivative of these curves (transferred charge capacitance) show over four times as much overshoot for the negative pulse as compared to the positive, and a large amount compared to other devices in general. This is indicative that a much greater amount of space charge is being created during the negative pulse. At the same time, about 40% more charge is transferred per half-cycle during the negative pulse. These two facts, taken together, may explain the enhanced aging stability, assuming that hot electron damage to one of the insulator-phosphor interfaces is the dominant aging mechanism. The space charge asymmetry shown in the more stable device may act to reduce the field at the sensitive interface while it acts as the anode, or it may reduce the electron flux to the sensitive interface, thereby reducing aging. Additionally, the large phosphor thickness and space charge densities of this device reduce the average phosphor electric field, which may mitigate hot electron damage.

6.4 Conclusion

A study of the aging characteristics of evaporated ZnS:Mn alternating-current thin-film electroluminescent (ACTFEL) devices is undertaken by monitoring the capacitance-voltage (*C*-*V*) characteristics at various temperatures as a function of aging time. Short-term ACTFEL aging is characterized by a rigid shift in the *C*-*V* curve to higher turn-on

voltage with aging time. Additionally, the insulator and phosphor capacitances are found to be independent of aging time, the internal phosphor threshold voltage increases slightly with aging time, and the conduction and polarization charges are observed to decrease with aging time.

A study of aging characteristics of sputtered Zn_2GeO_4:Mn ACTFEL devices is presented. Although the electro-optic performance and aging behaviour of these devices is rather good, the luminous efficiency is currently not sufficient to justify commercialization of this phosphor. Future efforts to improve the luminous efficiency of this phosphor should focus on alternatives to field-ionization of impact-excited Mn^{+2} luminescent impurities as a means of introducing space charge into the phosphor. Perhaps this could be accomplished via co-doping or the use of alternative annealing procedures. Also, the use of luminescent impurities with shorter lifetimes could be advantageous since this would minimize transient luminance annihilation.

Most of this work has involved characterization of the electric and/or luminescent properties of the ACTFEL devices as a function of aging time. This study is unique in that the aging characteristics are monitored, as a function of temperature and aging time, using the capacitance-voltage (*C-V*) technique, which offers several advantages for ACTFEL aging studies.

First, the technique can be readily automated.

Second, a wealth of device physics data can be acquired which leads to a better understanding of the internal electrostatic modifications associated with aging and, hence, of the physical mechanisms of aging. The obvious disadvantage of the *C-V* technique is that it exclusively monitors the electrical properties of the ACTFEL whereas the device performance must ultimately be assessed optically. Temperature-dependent *C-V* aging studies yield an aging activation energy of approximately 0.2 eV. ACTFEL aging is also characterized by a turn-on voltage which increases with aging time, a *C-V* transition which shifts rigidly with aging time, phosphor and insulator capacitances which are independent of aging time, a phosphor field which increases slightly with aging time, and conduction and polarization charges which decrease with increasing aging time.

7 General conclusions

Although the use and importance of green phosphors looked to be overcome, the target for the near future is the investigation of a green phosphor with enough brightness to maintain the correct ratio of brightness between the red, green and blue phosphors. For this reason, the **development of green ACTFEL phosphors** and **their characterization** is the main emphasis of this thesis although phosphors of other colors have not been entirely ignored.

Having this in mind, the principal **objectives** of this thesis were to **study the electrical and optical characterization** of ACTFEL devices, and specifically the **aging process** of materials that comprise the ACTFEL display. To achieve these objectives, we carried out optical, electrical, and opto-electric measurements of the ACTFEL structures and phosphor layers (as shown in Chapters 4, and 5). The study of the aging characteristics (Chapter 6) of evaporated and atomic layer epitaxy ZnS:Mn phosphors has been undertaken by monitoring the luminance-voltage (L-V) internal charge-phosphor field (Q-F_p) [45] and capacitance-voltage (C-V) electrical characteristics at in selected time intervals during aging. Short-term and long-term ACTFEL aging studies has been provided and an attempt to visualize locally the structure of phosphor with a subwavelenght resolution using Scanning near-field optical microscope (SNOM) has also been presented.

The important results of this study are:

1) **Luminance-voltage** (L-V) and **luminous efficiency-voltage** (η-V) characteristics are dependent on several factors [11, 45]:
   - the type of driving waveform,
   - the shape of the waveform, and
   - the frequency of the waveform.

The *fraction of time that the driving waveform spends above the turn-on voltage determines the luminance of the device.* Thus, a driving waveform with a higher frequency or a shape such that the time above turn-on is greater will cause a higher luminance.

The L-V characteristics are also dependent on
- the ambient temperature,
- the dopant concentration [53], and
- the thickness of the phosphor layer.

When the *temperature is increased*, the probability of de-excitation through non-radiative recombination is significantly increased, which *leads to reduced light output*. *Temperature* also may *affect the threshold voltage* in an L-V curve since interface emission and space charge generation mechanisms are dependent on temperature [45].

Luminance increases with luminescent impurity dopant level for *low concentrations* [53]. Increasing the density of luminescent centers raises the probability of an electron undergoing a collision with a luminescent center. This trend holds as long as the impurity concentration is low enough that phosphor crystallinity is maintained and concentration quenching does not occur.

Increasing the phosphor layer thickness also *increases the probability of electron impact excitation with an impurity*. The *threshold voltage is* also *affected by the phosphor thickness, since a higher voltage is required to achieve the threshold electric field in a thicker device.*

An experimental study of the *luminance (brightness)-pulse width* characteristics ZnS:Mn devices shows that [59]:

- a *hysteresis appears* only if the *ZnS film is thicker than 200 nm*. Above it, the hysteresis width ΔB increases with the film thickness.
- a *threshold voltage* is related primarily to *electron tunneling* which is induced by the electric field ($E = V/d$) inside the layers. Therefore, the threshold voltage should increase as the *thickness of the ZnS film increases*.

2) **Photo-induced charge** (PIQ) and **Photo-induced luminance** (PIL) experiments show that e*lectron and hole transport may be studied independently* by simply changing the polarity of the DC bias. In ZnS:Mn^{2+} ACTFEL devices the hole transport may give rise to impact excitation-induced electroluminescence, holes are approximately half as efficient as electrons in contributing to the transferred charge, and that the efficiency of transport is significantly greater for holes than electrons [55, 57].

The fact *that photo-induced hole efficiency is greater than the photo-induced electron efficiency was very surprising.* This result can be interpreted as arising from differences in the electric field profile in the phosphor for the cases of hole and electron transport. The further study suggests that hole transport is not effective in ZnS, and that what appears to be hole-induced effects are actually due to whole trapping-induced back injection of electrons.

Photo-induced charge (PIQ) and hole drift length measurements of evaporated ZnS:Mn ACTFEL devices with variable phosphor thicknesses provide information related to the transport of electrons and holes in the ZnS phosphor. Hole PIQ curve trends are dominated by hole trapping. Hole trapping is characterized by a drift length of ~ (180±70) nm, a hole lifetime of ~ 2 ps, and a trap capture cross-section of ~ 7×10^{-13} cm^2. This is a large capture cross section, corresponding to a negatively charged deep level trap whose charge state leads to very efficient hole capture due to the attractive Coulombic interaction between the trap and the hole. We speculate that this hole-trap is most likely a defect complex involving a zinc vacancy [45, 46].

3) **Influence of KCl co-doping on the microstructure and the electroluminescent properties of ZnS:Mn phosphors**:

At temperatures of 700°C, incorporation of KCl *improves the crystallinity of the ZnS:Mn* phosphors by enhancing grain growth in the columnar grains and causing them to consume a 100nm layer of equiaxed fine grains at the ATO/ZnS interface. In

addition, KCl co-doping allows growth of grains to diameters > 1μm at $T \approx 900°C$. Kalium (K) diffused through the ZnS film at $T \geq 600°C$ in 5min, and exhibits small activation energy. Based on these observations and its ionic size, it is postulated that *K occupies interstitial sites in cubic ZnS*, and therefore acts as a donor in the lattice.

Co-doping with KCl *improves the brightness and efficiency by ≈100%*, and *increases the threshold voltage* and makes the slope of the *B–V* plot much larger.

The EL data show that while improved crystallinity may reduce non-radiative recombination, the *most important effects* of KCl co-doping are a *reduction of space charge* and *band bending* with a resulting l*arger, hotter electron population in the EL phosphor* [60].

4) ACTFEL devices aging trends

Most of this work has involved characterization of the electric and/or luminescent properties of the ACTFEL devices as a function of aging time.

ACTFEL devices tend to stabilize after a few tens of hours of burn-in, but can exhibit **complex aging behavior** afterwards during the aging process. This study is unique in that the aging characteristics are monitored, as a *function of temperature* and *aging time*, using the *capacitance-voltage (C-V) technique*, which offers several advantages for ACTFEL aging studies.

First, the *technique can be readily automated*. Second, a *wealth of device physics data can be acquired* which leads to a *better understanding of the internal electrostatic modifications associated with aging* and, hence, of the physical mechanisms of aging.

The obvious disadvantage of the *C-V* technique is that it exclusively monitors the electrical properties of the ACTFEL whereas the device performance must ultimately be assessed optically. Temperature-dependent *C-V* aging studies yield aging activation energy of approximately 0.2 eV. ACTFEL aging is also characterized by a turn-on voltage which increases with aging time, a *C-V* transition which shifts with aging time, phosphor and insulator capacitances which are independent of aging time, a phosphor field which increases slightly with aging time, and conduction and polarization charges which decrease with increasing aging time.

These experimental observations lead to a **model for ACTFEL aging** in which *hot-electron-mediated atomic migration near the insulator/phosphor interfaces gives rise to the creation of defect complexes which act as deep level traps and increase the interface fixed charge density.* The atomic rearrangement is envisaged to occur very close to the interface (within perhaps 100 Å), to most likely involve the presence of sulfur vacancies, and to probably occur by nearest-neighbor hopping.

The luminance-voltage curves for ZnS:Mn devices in which the phosphor layer was deposited, tend to shift to slightly higher voltage during burn-in [64].

The primary experimental results are the following:

- The insulator and phosphor capacitances are constant with respect to aging time; this suggests that the *perturbation in the electrostatic charge distribution* which is *responsible for aging occurs near the SiON/ZnS interfaces*.

- The *C-V* curve shifts rigidly with aging time; a rigid shift indicates that *changes in the fixed charge density*, not the interface charge density, *give rise to aging*.
- The activation energy for short-term aging is found to be approximately 0.2 eV. *Atomic rearrangement at SiON/ZnS interfaces leads to the formation of deep level*, *fixed charge states* which *trap transported conduction electrons*. Such electron trapping l*eads to a reduction of the conduction and polarization charges* and an *increase in the turn-on voltage*. It is likely that atomic migration is stimulated by the thermalization energy dissipated by hot electrons after they impinge upon the SiON conduction band discontinuity. Also, it is likely that atomic migration at the interface is exacerbated by the presence of sulfur vacancies in the ZnS near the interface.

The most striking implication of the **aging trends** is that the *interface state distributions* at the *top and bottom interfaces* are *asymmetric* and *exhibit highly asymmetric aging characteristics*.

- The interface state densities of the top and bottom interface are distinctly different and exhibit different aging characteristics.
- Both shallow and deep traps are created during aging at the bottom interface.
- A lesser number of predominately deep traps are created at the top interface during aging.
- The decrease in C_i with aging indicates that some of the "interface state charge" actually moves deeper into the ZnS bulk with aging, and
- The decrease in the *C-V* overshoot of the bottom interface indicates that the amount of space charge build up in the ZnS decreases with aging time.

A short study of aging characteristics of borrowed sputtered Zn_2GeO_4:Mn ACTFEL device was also presented [66]. Although the electro-optic performance and aging behaviour of this phosphor was rather good, the luminous efficiency was currently not sufficient to justify commercialization of this phosphor.

Future efforts to improve the luminous efficiency of this phosphor should focus on alternatives to field-ionization of impact-excited Mn^{+2} luminescent impurities as a means of introducing space charge into the phosphor.

Perhaps this could be accomplished via co-doping or the use of alternative annealing procedures. Also, the use of luminescent impurities with shorter lifetimes could be advantageous since this would minimize transient luminance annihilation.

A non-negligible objective of this thesis is also its pedagogical aspect. Therefore, the presented text can be considered as a textbook suitable for our students in Libya.

For further development of these structures, it is strongly expected to create new functional materials beyond a scope of conventional inorganic compounds. The targets of our ongoing research project are to create new organic-inorganic hybrid systems with new types of electronic and optical functions and to open the new frontiers of advanced applications, such as memory devices with a huge recording density and a light-emitting flat panel with high energy-conversion efficiency.

8 References

[1] KOBAYASHI, H., TANAKA, S. The present and future prospects of electroluminescent phosphors, *Journal of SID*, 1996, Vol. 4, No.3, p. 157-163.

[2] DESTRIAU, G., Recherches sur les scintillations des sulfures de zinc aux rayons, *Journal de la Chimie et de la Physique*, 1936, Vol. 33, No. 9, p. 587-625.

[3] VLASENKO, N.A., POPKOV, Y.A., The electroluminescence of sublimate phosphor ZnS:Mn, *Optika i Spektroskopiya*, 1960, Vol. 8, No. 1, p. 81-88.

[4] INOGUCHI, T., TAKEDA, M., KAKIHORA, Y., YOSHIDA, M., Stable high luminance thin-film electroluminescenct panels, *SID Digest*, 1974, Vol. 5, No. 1, p. 84 - 92.

[5] MAUCH, R.H., The current status of thin-film electroluminescence, *Journal of SID*, 1997, Vol. 5, No. 3, p. 173-178.

[6] ONO, Y. A., *Electroluminescent display*, World Scientific, Singapore, 1995.

[7] HITT, J.C., BENDER, J.P., WAGER, J.F. Thin-film electroluminescent device physics modeling, *Critical Review of Solid State Materials Science*, 2000, Vol. 25, No. 1, p. 29-85.

[8] STUYVEN, G., De VISSCHERE, P., NEYTS, K., HIKAVYY, A., Hybrid electroluminescent devices with atomic layer deposited thin films on a screen printed dielectric, *Japanese Journal of Applied Physics*, *part 1-regular papers short notes & review papers*, 2002, Vol. 41, No. 8, p. 5702 -5705.

[9] BRINGUIER, E., Statistical mechanics of high-field transport in semiconductors, *Physical Review*, 1995, Vol. B 52, No. 11, p. 8092 – 8105.

[10] WAGER, J. F., KEIR, P. D. Electrical characterization of thin-film electroluminescent devices In *Annual Review of Materials Science*, Palo Alto, 1997, Vol. 27, p. 223-248.

[11] AHMED, M.M.A., TOMANEK, P., Luminance-voltage and efficiency-voltage characterization of ZnS:Mn^{2+} alternating-current thin-film electroluminescent device, In *11th Electronic Devices and Systems (EDS 04) Conference*, Brno, Vysoké učeni technické v Brně, 2004, s. 76 - 79, ISBN 80-214-2701-9

[12] SZE, S.M., *Physics of semiconductor devices*, 2nd ed., 1981, New York: Wiley-Interscience.

[13] KOBAYASHI, H., TUETA, R., MENN, R. Thin-film electroluminescent device with a Ge layer, *IEEE Transaction on Electron Devices*, 1982, Vol. ED-29, No.10, p. 1626-1630.

[14] OHWAKI, J., KOZAWAGUCHI, H., TSUJIYAMA, B. Stacked insulator structure thin-film display device, *Journal of the Electrochemical Society*, 1990. Vol. 137, No. 2, p. 340 - 344.

[15] RACK, P.D., HOLLOWAY, P.H., The structure, device physics, and material properties of thin film electroluminescent displays, *Materials Science and Engineering*, 1998, Vol. R21, No. 2, p. 171-219.

[16] KITTEL, C., *Introduction to Solid State Physics*, 6th ed., 1986, New York: John Wiley and Sons, Inc.

[17] BRENNAN, K., Theory of high-field electronic transport in bulk ZnS and ZnSe, *Journal of Applied Physics*, 1988. Vol. 64, No. 8. p. 4024-4030.

[18] MACH, R., MUELLER, G.O., Ballistic transport and electroluminescence in IIB-VI and IIA-VI compounds, *Journal of Crystal Growth*, 1990, Vol. 101, No. 10, p. 967-975.

[19] BHATTACHARYYA, K., GOODNICK, S.M., WAGER, J.F., Monte Carlo simulation of electron transport in alternating-current thin-film electroluminescent device, *Journal of Applied Physics*, 1993, Vol. 73, No. 7, p. 3390-3395.

[20] BRINGUIER, E., J. Impact excitation in ZnS-type electroluminescence, *Journal of Applied Physics*, 1991, Vol. 70, No. 8, p. 4505-4512.

[21] BARAFF, G.A., Distribution functions and ionization rates for hot electrons in semiconductors, *Physical Review,* 1962. Vol. 128, No. 6, p. 2507-2517.

[22] BLASSE, G., GRABMAIER, B.C., *Luminescent materials*, 1994, Berlin: Springer-Verlag.

[23] HARKONEN, G., LEPPANEN, M., SOININEN, E., TORNQVIST, R., VILJANEN, J., Multicolour thin film electroluminescent displays: a new application of rare earth metals, *Journal of Alloys and Compounds*, 1995. Vol. 225, No. 1-2, p. 552-554.

[24] HONG XIAN, BENALLOUL, P., BARTHOU, Ch., BENDIT, J. Excitation and radiative efficiencies in ZnS:Mn thin film electroluminescent devices prepared by reactive radio-frequency magnetron sputtering *Japanese Journal of Applied Physics*, 1994, Vol.33, Part 1, No. 10, p. 5801-5806

[25] STEVENS, H., 2000, *Fabrication sheet*, Dow Corning, Inc.

[26] KEIR, P.D., *Fabrication and characterization of ACTFEL devices*, Masters thesis, 1999, Oregon State University, Corvallis. 280 p.

[27] Präzision Glass & Optics, http://www.pgo-online.com, retrieved October 2005.

[28] KIM, H.,GILMORE C M, PIQUÉ A., HORWITZ, J. S., MATTOUSSI, H., MURATA, H., KAFAFI, Z.H., CHRISEY, D.B., Electrical, optical, and structural properties of indium-tin-oxide thin films for organic light-emitting device, *Journal of Applied Physics*, 1999. Vol. 86, No.11, p. 6451-6461.

[29] PAINE, D.C., WHITSON, T., JANIAC, D., BERESFORD, R., YANG, C.O., A study of low temperature crystallization of amorphous thin film indium-tin-oxide, *Journal of Applied Physics*, 1999, Vol. 85, No. 12, p. 8445-8450.

[30] CHOPRA, K.L., MAJOR, S., PANDYA, D.K., Transparent conductors-a status review, *Thin Solid Films,* 1983, Vol. 102, No. 1, p. 1-4.

[31] TIKU, S.K., SMITH, G.C., Dielectrics for bright EL displays, *IEEE Transactions on Electron Devices*, 1984. Vol. ED-31, No. 1, p. 105-108.

[32] ONO, Y. *Progress in information display technology*, S. KOBAYASHI (Ed.). Vol. 1, 1995, Singapore, World Scientific Publishing Co.

[33] HOWARD, W.E., The importance of insulator properties in a thin film electroluminescent device, *IEEE Transaction on Electron Devices*, Vol. ED-24, No. 7, p. 903 -908.

[34] TANAKA, S., SHANKER, V., SHIIKI, M., DEGUCHI, H., KOBAYASHI, H., Multi-color electroluminescence in alkaline-earth-sulfide thin-film devices, *SID Digest*, 1985, p. 218-222.

[35] TANNAS, L.E., *Flat-panel displays and CRT's,* 1985, New York: Van Nostrand Reinhold. 468 pp.

[36] PICKERING, H.S., *The covalent bond*, 1978, London, Wykeham Publications

[37] KALE, A., SHEPHERD, N., DEVITO, D., GLASS, W., DAVIDSON, M., HOLLOWAY, P.H., Infrared emission from zinc sulfide: Rare-earth doped thin films, *Journal of Applied Physics*, 2003, Vol. 94, No. 6, p. 3147-3152.

[38] BALLATO, J., LEWIS J.S. III, HOLLOWAY, P.H., Display applications of rare-earth-doped materials, *MRS Bulletin*, 1999, Vol. 24, No. 9, p. 51-56.

[39] WACHTLER, M., SPEGHINI, A., GATTERER, K., FRITZER, H.P., AJO, D., BETTILENNI, M., Optical properties of rare earth ions in lead germanate glasses, *Journal of the American Ceramic Society*, 1998, Vol. 81, No.8, p. 2045-2052.

[40] GEORGOBIANI, A.N., GRUZINTSEV, A. N., BARTHOU, C., BENALLOUL, P., BENOIT, J., TAGIEV, B.G., TAGIEV, O.B., ZHABBOROV, R.D., Infrared luminescence of Er[3+] in calcium thiogallate, *Journal of the Electrochemical Society*, 2001. Vol. 148, No. 11, p. H167-H170.

[41] ZEINERT, A., BENALLOUL, P., BENOIT, J., BARTHOU, C., DREYHSIG, J., GUMLICH, H.E., On the excitatory efficiency in ZnS:Mn thin-film electroluminescent device, *Journal of Applied Physics*, 1992, Vol. 71, No. 6, p. 2855-2862.

[42] IN SOOK LEE, PENNATHUR, S., GOODNICK, SM, WAGER, J.F., Band structure and high-field electron transport of a ZnS phosphor in AC thin-film electroluminescent device, *Journal of Korean Physical Society,* **1**997, Vol. 31, No. 3, p. 517~520

[43] LIDE, D.R., FREDERIKSE, H.P.R. (Eds.) *CRC Handbook of chemistry and physics*. 78th ed., 1997, Boca Raton: CRC Press.

[44] TROPPENZ, U., HUTTL, B., STORZ, U., KRATZERT, P., WELTHAUS, K.O., SUN, S. S., TUENGE, R.T., Photoluminescence and electroluminescence studies on Cu and Ag doped SrS ACTFEL devices. *Extended abstracts of the 4th International Conference on the Science and technology of display puhosphors,* 1998, p. 187-190.

[45] AHMED, M., TOMÁNEK, P. Influence of charged centers on transport characteristics of alternating current thin film electroluminescent devices. *Proceedings of SPIE*, 2006, Vol. 6018, No. 6018, p. 61 – 65, ISSN 0277-786X.

[46] AHMED, M.M.A., Subtreshold voltage-induced transferred charge aging analysis of alternating-current thin-film electroluminescent device, In *New Trends in Physics 2004,* Brno, Ing. Zdeněk Novotný, CSc., 2004, p. 196 - 199, ISBN 80-7355-024-5

[47] KRASNOV, A.N., Alternating-current thin-film electroluminescent devices: effect of fabrication conditions on aging and failure defect formation, *Progress in Crystal Growth and Characterization of Materials*, 1998, Vol. 37, No. 1, p. 123-167.

[48] DAVIDSON, J. D., WAGER, J. F., KHORMAEI, R. I., KING, C. N., WILLIAMS, R., Electrical characterization and modeling of alternating-current thin-film electroluminescent devices, *IEEE Transaction on Electron Devices*, 1992, Vol. 39, No. 9, p. 1122-1128.

[49] BAUKOL, B. A., KEIR, P. D., CLEARY, B. A., NEVERS, C. A., PLANT, T. K., WAGER, J. F. , Electro-optic characterization of thin-film electroluminescent devices, In B. R. VADDI, H. S. NALWA (Eds.) *Handbook of luminescence and display materials and devices*, , American Scientific Publishers, 2003, Vol. 2, p. 489- 535.

[50] AHMED, M. M. A., Aging study of atomic layer epitaxy ZnS:Mn alternating-current thin-film electroluminescent devices, In *Proceedings of the 11th Conference, STUDENT EEICT 2005*, FEKT VUT Brno, Vol. 2., p. 193-197, ISBN 80-214-2889-9.

[51] DOBIS, P., BRÜSTLOVÁ, J., GRMELA, L., TOMÁNEK, P. Electrooptical characterization of ZnS:Mn thin-film electroluminescent devices, In *10th EDS 2003 Electronic Devices and Systems Conference*, Brno, Ing. Zdeněk Novotný, CSc., 2003, p. 287 - 290, ISBN 80-2142452-4.

[52] Technical report – Denso Technology 2001 – Instrument clusters, http://www.globaldenso.com/TECHNOLOGY/tec-report/2001/pdf/T2001_S19.pdf

[53] AHMED, M.M.A., Phosphor materials and luminescent impurities for ACTFEL device, In *Workshop NDT 2004 Non destructive testing.* Brno University of Technology, 2004, p. 8 - 13, ISBN 80-7204-371-4

[54] NEYTS, K. A., CORLATAN, D., VISSCHERE, P.D., DEN BOSSCHE, J. V., Observation and simulation of space-charge effects and hysteresis in ZnS:Mn ac thin-film electroluminescent devices, *Journal of Applied Physics*, 1994, Vol. 75, No. 8, p. 5339-5346.

[55] AHMED, M.M.A, Photo-induced charge and luminescence measurements in ZnS:Mn alternating-current thin-film electroluminescent devices, In *New trends in Physics NTF 2004*, Brno, Ing. Zdenek Novotny, CSc., 2004, s. 200 - 203, ISBN 80-7355-024-5

[56] VLASENKO, N.A., BELETSKII, A.I., DENISOVA, Z.L., KONONETS, YA.F., VELIGURA, L.I., Use of photodepolarization spectra for diagnostics and characterization of alternating current thin-film electroluminescent (ACTFEL) devices, *Proceedings of SPIE*, 1998, Vol. 3359, No. 3359, p. 512-518.

[57] AHMED, M.M.A, Photo-induced charge and hole drift length measurements of evaporated ZnS:Mn alternating-current thin-film electroluminescent devices, In *Elektrotechnika a informatika 2004,* Plzeň, Fakulta elektrotechnická, Západočeská univerzita v Plzni, 2004, p. 63 - 66, ISBN 80-7043-300-0.

[58] SHIH, S.P., KEIR, P. D., WAGER, J. F., Space charge generation in ZnS:Mn alternating-current thin-film electroluminescent devices, *Journal of Applied Physics*, 1995, Vol. 78, No. 8, p. 5775-5781.

[59] AHMED, M. The dependence of brightness and threshold voltage of memory ZnS:Mn thin film electroluminescent device upon its thickness, In *Proceedings of the 12th Conference STUDENT EEICT 2006*, 2006. Brno: Vysoké učení technické v Brně, FEKT a FIT, 2006, Vol. 4, p. 128 - 132, ISBN 80-217-4-3162-8

[60] AHMED, M. Electroluminescence brightness and luminous efficiency of ZnS:Mn doped with KCl, In *Proceedings of the 13th Conference STUDENT EEICT 2007.* Brno: Ing. Zdeněk Novotný, CSc., Ondráčkova 105, Brno, 2007, Vol. 3. p. 210 - 214, ISBN 978-80-214-3409-7

[61] SOENEN, B., VAN DEN BOSSCHE, J., DE VISSCHERE, P., Kinetics and aging in atomic layer epitaxy ZnS:Mn AC thin-film electroluminescent device, *Journal of Applied Physics*, 1997, Vol. 82, No. 8, p. 5241-5246.

[62] KEIR, P.D., PLANT, T.K., WAGER, J.F., SUN, S.S., Photo-induced charge and luminescence measurements of evaporated ZnS:Mn alternating-current Thin-film electroluminescent devices*, Journal of SID*, 2000, Vol. 51, Suppl-1, p. 51-56.

[63] SHIH, S.P. *Electrical characterization and aging studies of ALE ZnS:Mn ACTFEL devices with varying phosphor thickness,* M.S. thesis, Oregon State University, 1996.

[64] AHMED, M. M. A., Aging study of evaporated ZnS:Mn alternating-current thin-film electroluminescent devices, In *Proceedings of the 11th Conference, STUDENT EEICT 2005*, FEKT VUT Brno, 2005, Vol. 2., p. 193-197, ISBN 80-214-2889-9.

[65] LEWIS, J.S., DAVIDSON, M., HOLLOWAY, P., Control of point defects and space charge in electroluminescent ZnS:Mn thin films, *Journal of Applied Physics*, 2002, Vol. 27, No. 12, p. 6646-6657.

[66] AHMED, M. Aging characteristics of green-emitting Zn_2GeO_4:Mn alternating-current thin-film electroluminescent devices, *Transactions of the VŠB – Technical University of Ostrava*, *Mechanical Series,* 2005, Vol. LI, No. 2, p. 1-6, ISSN 1210-0471

[67] WILLIAMS, L.C., NORTON, D., BUDAI, J., HOLLOWAY, P.H., Cathodoluminescence from thin film Zn_2GeO_4:Mn phosphor grown by pulsed laser deposition, *Journal of Electrochemical Society*, 2004, Vol. 151, No. 8, p. H188-H191.

9 Abbreviations

ACTFEL	alternating-current thin-film electroluminescent
ALE	atomic layer epitaxy
ATO	aluminum titanium oxide
B-V	brightness-voltage
B-W	brightness-pulse width
CIE	Comité International d´Eclairage
C-V	capacitance-voltage
CRT	cathode-ray tube
CVD	chemical vapor deposition
DEZ	diethylzinc
EBE	electron beam evaporation
EL	electroluminescence
FED	field-emission display
FPD	flat-panel display
ITO	indium tin oxide
LCD	liquid-crystal display
L-V	luminance-voltage
MISIM	metal-insulator-semiconductor-insulator-metal
PB	propagating breakdown
PDP	plasma display panel
PECVD	plasma enhanced chemical vapor deposition
PIL	photo-induced luminescence
PIQ	photo-induced transferred charge
PL	photoluminescence
Q-F_p	internal charge-phosphor field
Q-V	charge-voltage
Q_p-F_p	charge flow vs. electric field across the phosphor layer
RE	rare earth
RF	radio frequency
RMS	root mean square
RTA	rapid thermal annealing
SHB	self healing breakdown
SNOM	scanning near-field optical microscope
TCO	transparent conducting oxide

TEM	transmission electron microscopy
TFEL	thin-film electroluminescent
VIQ	voltage-induced transferred charge
η-V	luminous efficiency-voltage

Symbols

B_s	saturation brightness
C	capacitance
C_i	insulator capacitance
C_p	phosphor capacitance
C_{sense}	sensor capacitance
C_t	total capacitance prior to breakdown
E	electric field
E_{DB}	electrical breakdown field
E_g	band gap
F_p	electric field across a phosphor layer
F_{ss}	average steady-state phosphor field
J	tunneling emission current
J_e	thermionic current- electronic charge flux
L	luminance
L	effective radius of the field
N	concentration of dopant centers
N_e	number of luminescent ions in the excited state
N_t	trap density
P	power
P_{eg}	probability for spontaneous emission from the excited to the ground state
Q	electric charge
Q_{cond}	conduction charge
Q^e_{max}	maximum external charge
Q^e_{leak}	leakage charge
Q_p	internal charge across a phosphor layer
Q^e_{pol}	polarization charge
Q^e_{relax}	relaxation charge
Q_{ss}	averaged steady state charge
R_c	current sense resistor
R_s	series resistor
S	area of the test spot
S	scattering rate
T	temperature
T_d	decay-time
T_{ir}	internal radiative decay-time

T_{inr}	internal nonradiative decay time
V	voltage
V_{app}^{tot}	total applied voltage
V_p	total voltage applied across the phosphor layer
V_{to}	turn-on voltages
V_{th}	threshold voltage
ΔV	hysteresis voltage margin
d_i	thicknesses of insulator layer
d_p	thicknesses of phosphor layer
h	Planck's constant
$\hbar$	restricted Planck's constant h divided by 2π
$i(t')$	current waveform
j	spherical Bessel function
k	Boltzmann's constant
$\vec{k}$	wave vector
l_i	impact length
m	mass of electron
m^*	effective electron mass
n	refractive index
$n(E)$	electron energy distribution
q	charge of electron
$q_{ext}(t)$	external charge
$v(t')$	voltage waveform
$v_a(t)$	voltage measured across the device
v_{sat}	saturated drift velocity
t	time
t_r	free flight time
Φ	work function
Φ_B	barrier height
Γ	total scattering rate
δ_l	phase shift
ε	dielectric constant (permittivity)
ε_i	dielectric constant of insulating layer
λ	wavelength
η	luminous efficiency
η_{opt}	optical outcoupling efficiency
ρ	hole concentration
σ	excitation cross-section of the luminescent center
θ_c	critical angle for internal reflection
τ	period of the driving waveform
τ	hole lifetime
τ_R	radiative decay time

Definition of terms

Burn-in: To run a system or device for a period of time to ensure that all components are working properly.

Electroluminescence: The nonthermal generation of light resulting from the application of an electric field to a substance, usually a luminescent crystal.

Latent image: The ghost image of a previously displayed pattern which can sometimes be seen in a full field on an electronic display screen.

Light emission decay time: The time it takes for the light emission from one excitation pulse to fall to $1/e$ times its initial value.

Polarization charge: The charge trapped at the phosphor/insulator interface following the application of a drive pulse.

Polarization field: The field across the phosphor layer resulting from the polarization charge.

Q_p-F_p loop: The closed curve which results from plotting the internal charge flow across the phosphor layer (Q_p) vs. the electric field across the phosphor layer (F_p).

***Q-V* loop:** The closed curve which results from plotting the external charge (Q) flowing into a TFEL device vs. the externally applied voltage (V).

Threshold voltage: The voltage amplitude of the drive waveform above which current flows across the phosphor layer and light is emitted from a TFEL device.

Turn-on voltage: The voltage corresponding to the first knee in the Q-V loop of a TFEL device. This is the voltage at which charge begins to flow across the phosphor layer. This voltage is generally less than the threshold voltage because the internal field across the phosphor layer is enhanced by the polarization field once the polarization charge has built up in the steady state.